Universidad Carlos III de Madrid

Departamento de Teoría de la Señal y Comunicaciones

INGENIERÍA DE TELECOMUNICACIONES

PROYECTO DE FIN DE CARRERA

MULTI-BEAM ANTENNA SYSTEM FOR HAPS APPLICATIONS

En colaboración con LEMA/EPFL

Octubre 2011

Autor: Carlos Zorraquino Gastón
Tutor: Daniel Segovia Vargas
Tutor en EPFL: Juan Ramón Mosig
Asistente en EPFL: Marco Letizia

Contents

Visión global del proyecto

Los satélites de órbita terrestre baja (LEO-satélites) están encontrando un uso cada vez mayor en servicios de comunicaciones en los últimos años. Teniendo en cuenta sus beneficios, una nueva familia de estaciones está siendo estudiada y desarrollada, las estaciones en plataformas de gran altitud (HAPS). Con menor tiempo de desarrollo y presupuestos más pequeños, pueden cumplir con muchas de las funciones de los satélites.

En general, los satélites se encuentran en una órbita que está por encima de la tierra a una distancia de entre 200 y 4000 km. Los HAP son los dirigibles o aviones, que operan en la estratosfera, por lo general a una altura de 17 a 22 km. A esta altitud, se puede mantener una posición cuasi-estacionaria, y puede ofrecer una amplia gama de servicios, principalmente de comunicación y servicios de teledetección.

En comparación con los satélites de órbita geoestacionaria (GEO), los satélites LEO-HAPS tienen algunas ventajas importantes tales como una menor distancia al suelo (menos potencia necesaria, antenas más pequeñas ...), menor retardo en el tiempo, disponibilidad de efecto Doppler para la determinación de la posición, menor costo, una mayor flexibilidad, aunque son menos potentes.

Durante los últimos años una impresionante cantidad de trabajo ha sido llevado a cabo en el ámbito de los HAPS y los sistemas de telecomunicaciones relacionados con ellos, como se puede comprobar en [1]. Desde el punto de vista de las antenas, modelos de antenas para HAPS se han utilizado en [2] para analizar las prestaciones de un sistema basado en HAPS para comunicaciones inalámbricas.

La comunicaciones a través de un HAPS puede proveer servicios de banda ancha ofreciendo soluciones rentables para proporcionar una alternativa viable al cable o los satélites, con el potencial de llegar a los usuarios rurales, urbanos y en movimiento.

Los HAPS ofrecen una forma efectiva de explotación del espectro milimétrico mediante el uso de arquitecturas multicelulares, ver Figure 1. En el UIT-R [3] este tipo de aplicación se estudia y la banda de frecuencias que se asigna se define como 27,5-31,3 GHz. Este documento expone que la viabilidad de estos sistemas depende en gran medida de la capacidad de datos del sistema general, que a su vez esta gobernado por las propiedades de carga de las antenas que sirven a las células en el suelo.

Muchos servicios inalámbricos, como GPS y televisión, tienen la necesidad de utilizar polarización circular para alcanzar altos rendimientos. Ya que estos servicios se pueden mejorar mediante el uso de HAPS (dados sus beneficios intrínsecos antes

mencionados), un sistema de antenas multi-haz can polarización es un elemento básico a desarrollar para la aplicación de HAPS.

Por lo tanto, este documento presenta en la sección 1 posibles sistemas de antenas con las diferentes tecnologías que podrían ser utilizadas en estas aplicaciones. Después, sus inconvenientes y problemas potenciales son identificados y estudiados, las secciones 2 y 3 presentan los dos principales problemas y proponen soluciones para superarlos, incluyendo simulaciones y resultados de mediciones. Además, aunque no se ha considerado dentro de los objetivos iniciales del proyecto, un problema adicional se ha identificado y caracterizado en la sección 4 donde también se proponen soluciones y estas son comprobadas mediante mediciones. Por último, las nuevas posibilidades que se presentan como futuro trabajo y un resumen se recoge en la sección 6.

Mención especial debe hacerse a la sección 3.3, donde un esfuerzo adicional se llevo acabo para proponer un método innovador para la optimización de las estructuras polarizador mediante líneas de meandro.

Sección 1: Escenario y aspectos generales

La sección 1 describe las especificaciones definidas por el escenario considerado en el ámbito de este proyecto . Las características del escenario se recogen en la Tabla 1.1.1.

Una vez se han definido las especificaciones del sistema para las características del sistema, la sección 1 explora diferentes alternativas que han sido estudiadas para obtener el correcto diagrama de radiación multi-haz:

- **Array impreso**: Esta estrategia presenta algunas ventajas como son sus pequeñas dimensiones, su bajo costo, su fácil fabricación y configuración. Sin embargo, su red de alimentación es compleja y no puede manejar potencias muy altas.
- **Array de hélices**: Esta estrategia presenta algunas ventajas como son la polarización circular, el bajo costo y que su forma de haz depende fuertemente en el diseño de la antena. Sin embargo, presenta un gran volumen, las hélices son difíciles de fabricar para aplicaciones de 30GHz y su mecánica es delicada. Además, la red de alimentación se llevó a cabo en un circuito microstrip que limita la capacidad de potencia.
- **Guías de onda cilíndricas en combinación con una lente esférica:** El uso de guías de ondas permite manejar alta potencia, además la interacción con la lente se puede controlar mediante el diseño de una bocina adecuada. El uso

de tecnologías de la guía de onda implica también que cada alimentador sea mecánicamente independiente de los otros.

La construcción de las guías de onda puede ser realizada de forma precisa y económica en aluminio o latón mediante el uso de máquinas de taladro digitales. Además, la polarización circular es fácil de lograr mediante la combinación de guías de onda circular y polarizadores.

Debido a todas sus ventajas frente a las otras alternativas estudiadas, este modelo es el que se ha decido utilizar en el diseño del sistema de antenas multi-haz para HAPS.

Una vez que se ha decidido utilizar la alternativa de una guía de onda con lente, la sección 1 hace un análisis para diferentes lentes y polarizadores:

- **Lente esférica de dieléctrico uniforme**: Con un diseño muy simple y adecuadas prestaciones es la lente que se ha decidido utilizar en el sistema de antenas para HAPS.
- **Lente Luneberg**: Con un cambie suave de su permitividad esta lente reduce las reflexiones y sitúa el punto focal en la superficie de la lente. Sin embargo, su difícil construcción hace que esta opción sea descartada.
- **Polarizador interno basado en secciones elípticas:** Donde se ha concluido que las pérdidas de retorno disminuyen a medida que el número de secciones elípticas aumenta pero no es posible asegurar que la relación axial es mejor cuando el número de secciones elípticas aumenta. Aunque el ancho de banda que presenta no es suficiente, este polarizador podría ser utilizado en una sub-banda en la banda Ka, ya que se ha demostrado que la directividad deseada se puede lograr mediante la colocación de su apertura cerca de la superficie de la lente.

  El mayor problema de este polarizador es que la relación axial se degrada cuando la onda pasa a través de la lente y esta degradación es mayor en el caso de que se desplace el punto de observación con respecto al centro de la célula.
- **Polarizador interno basado en una pieza de dieléctrico:** Teniendo en cuenta los resultados obtenidos para este polarizador, se podría decir que es adecuado en este escenario, ya que presenta un coeficiente de reflexión pequeño, presenta una diferencia de fase entre las componentes de polarización en torno a 90 º y por lo tanto presenta una buena relación axial. Sin embargo, la relación axial se degrada cuando la onda pasa a través de la

lente y esta degradación es mayor en el caso de que se desplace el punto de observación con respecto al centro de la célula.

- **Polarizador externo de líneas de meandro:** Básicamente, la idea de usar este polarizador surge de la posibilidad de evitar la degradación de la polarización circular cuando la onda pasa a través del lente realizando el cambio de la polarización después de la lente.
  El principio de funcionamiento de este polarizador consiste en crear un desfase de 90º entre las dos componentes del campo eléctrico que incide con polarización lineal.
  Dado que este es el polarizador que se va ha utilizar en el diseño complete del sistema de antenas para HAPS, la sección 1 presenta una detallada definición del polarizador y expone en el estado del arte en el análisis de este tipo de estructuras incluyendo: la solución de Young para las perdidas de inserción ,la solución de Terrent para cada sección del meandro usando el método de los momentos, la solución analítica de Chu & Lee, puertos Floquet, método de los momentos y método de los momentos periódico.

Una vez que han sido escogidos los elementos que componen el sistema complete, la sección 1 analiza el comportamiento del mismo para los casos de uno y varios alimentadores. De este análisis se puede concluir que el sistema es adecuado pero presenta una serie de problemas potenciales que se deben corregir:

- Deformación elíptica de las células exteriores.
- Degradación de la polarización circular para las células exteriores.
- Acoplamiento entre alimentadores.

Las siguientes secciones tratarán de analizar y proponer diferentes soluciones a los problemas potenciales que se han identificado.

Sección 2: Corrección de la elipticidad en las células exteriores

Para tratar de corregir la deformación de la frontera de las células exteriores que adoptan forma elíptica, en la sección 2 se analizan diferentes alternativas que han sido propuestas.

El primer paso consiste en la caracterización del problema mediante un software diseñado en Matlab. Este programa es capaz de predecir la distribución de potencia en el suelo para determinadas condiciones y, hacienda la operación inversa, es capaz de calcular el diagrama de radiación necesario para producir una determinada distribución de potencia en el suelo para ciertas condiciones. Por lo tanto, hacienda uso de este software, se calcula como se debería modificar el diagrama de radiación para las células exteriores para producir así una frontera de célula circular. Este análisis nos lleva a la conclusión de que la directividad debe ser incrementada en la dirección del eje mayor de la elipse que dibuja la frontera de la célula.

Una vez conocidas las condiciones que debe cumplir el Nuevo diagrama de radiación, la sección 2 analiza las posibles soluciones que se plantean:

- **Posiciones de las guías de onda**: Esta alternativa trata de corregir la elipticidad de las células exterior mediante dos cambios distintos en las posiciones de los alimentadores con respecto a la lente:

    - **Inclinación del eje del alimentador**: La directividad es la misma en todas las direcciones por lo tanto esta solución no es valida para compensar el efecto de elipticidad en las células externas. Además, se deduce que como el eje longitudinal de la guía de onda no apunta al centro de la lente, la directividad se reduce en general. Por otra parte se observa una ligera asimetría en el haz que podría ser utilizada para otros usos en el futuro.
      Además, se demuestra la concordancia entre los resultados de las simulaciones de CST y los resultados de las mediciones por lo que es posible tomar como referencia los resultados de las simulaciones.
      Para la realización de las medidas en esta situación, una pieza ha sido especialmente diseñada haciendo uso de Solid Works y dando la libertad de movimiento requerida a la guías de onda.

- **Desplazamiento de la posición del alimentador en la dirección tangente a la lente:** la directividad es similar en los dos planos de corte relevantes por lo que la solución no es válida para corregir el efecto de excentricidad en las células externas. Además, se demuestra la alimentación excéntrica implica una orientación del haz cambiando el ángulo de proyección en el suelo. Este efecto puede ser útil para cambiar la distribución de las guías de onda con respecto a la lente para conseguir una distribución plana. Pero es necesario tener en cuenta que, dado que el eje longitudinal de la guía de onda no apunta al centro de la lente y que la apertura se aleja del punto focal, la directividad se reduce en general y la forma del haz resultante presenta una cierta asimetría que podría ser utilizado para otros usos en el futuro.

  Por otra parte, se demuestra la concordancia entre resultados de las simulaciones de CST y los resultados de las mediciones. Por lo tanto, es posible el uso de las simulaciones para conocer de antemano el comportamiento del sistema.

  Para la realización de las medidas en esta situación una pieza ha sido especialmente diseñada haciendo uso de Solid Works y dando la libertad de movimiento requerida a la guías de onda.

- **Cambios en la geometría de la lente**. Esta alternativa trata de corregir la elipticidad de las células exterior mediante el cambio de la geometría de la lente convirtiéndola en una lente elíptica. Los resultados demuestran que, si el diámetro de la lente se extiende en la dirección del eje mayor de la elipse que dibuja el limite de la célula exterior y con la orientación perpendicular a la dirección de propagación de la onda:
  - La directividad se incrementa solo en la dirección deseada. Por lo tanto, es una solución válida para corregir el efecto de la elipticidad en las células externas.
  - Dado que actuar en la posición de las guías de onda no es una solución válida para compensar el efecto de la elipticidad en las células externas, se puede concluir que para obtener una solución valida es necesario actuar en los elementos que emiten radiación.
  - Optimización de la forma de la lente para una alimentación concreto no funciona para las posiciones de otros alimentos. => Es necesario ya sea para diseñar una forma de la lente con la simetría revolución o estudiar la alternativa de actuar en el cuerno de la alimentación o la guía de onda.

Sección 3: Corrección de la degradación de la polarización circular

Para tratar de corregir la degradación de la polarización circular que se introduce en el paso a través de la lente, en la sección 3 se analizan la posibilidad de utilizar un polarizador externo de líneas de meandro.

En esta sección se demuestra que el uso de este polarizador evita la degradación de la polarización pero también implica ciertas dificultades añadidas que acarrea su uso. En esta sección se comienzan explicando los dos problemas principales en el uso de estos polarizadores:

- **Problemas en el modelado y la simulación**: Se comprueba que la simulación de la estructura modelada en CST Microwave Studio acarrea computaciones muy costosas y por lo tanto su tiempo de simulación es muy largo. En consecuencia, se exploran diferentes metodologías para su simulación siguiendo las recomendaciones del equipo de apoyo de CST y se concluye que, aunque sea lenta, la técnica mas eficiente para simular el comportamiento de la estructura es el modelado del sistema complete y su análisis mediante el 'Transient Solver'.

- **Limitación en el ángulo de incidencia**: Se demuestra que el uso de polarizadores de líneas de meandro implica una limitación en el ángulo de incidencia de los haces con respecto a su superficie. Por lo tanto este hecho limita el numero de alimentadores que se pueden utilizar y por ello se limita el numero de células por 'cluster'.

Debido a la limitación en el ángulo de incidencia que supone el uso de este tipo de polarizadores, es necesario optimizar la estructura para determinados ángulos de incidencia . Por lo tanto, la sección 3 propone dos métodos de optimización:

- **Optimización mediante el uso de CST**: Dados los problemas para simular este tipo de estructuras haciendo uso de CST, este método de optimización no utiliza la herramienta de optimización de CST. En lugar de ello, se modifican los parámetros más sensibles y se simula el sistema completo para analizar su comportamiento. Teniendo en cuenta la tendencia en la modificación de su comportamiento, se han seleccionado unas dimensiones para construir un prototipo del polarizador.
  Esta sección describe el proceso de fabricación del prototipo de polarizador incluyendo la descripción de los procesos de:

- Preparación de mascaras
- Foto-revelado
- Ensamblaje

Una vez construido el prototipo se realizaron distintas medidas del sistema de antenas en una cámara anicónica. Esta sección recoge el proceso de toma de medidas y muestra los resultados obtenidos y los analiza llegando a la conclusión de que el prototipo de polarizador es adecuado para el caso de incidencia ortogonal paro no es valido para el caso de incidencia oblicua.

Dadas las pequeñas mejoras que supone el proceso de optimización con CST, se puede concluir que este método no constituye una herramienta útil para la optimización del modelo de polarizador.

Además, se puede concluir que un polarizador optimizado para incidencia ortogonal no es válido para ser utilizado en las células externas y por lo tanto un modelo optimizado para el ángulo de incidencia del haz externo debe ser diseñado. Con el fin de crear un polarizador que funcione para todos los haces, debe ser diseñado un modelo de línea de meandro diferente para las diferentes áreas de incidencia creando una transición suave en los límites de las áreas.

- **Optimización mediante teoría de líneas de transmisión**: Dada la ineficiencia en la optimización con CST, se ha decidido implementar un nuevo sistema de optimización basado en la teoría de líneas de transmisión.
  El nuevo método consiste en la implementación de un circuito equivalente a la estructura haciendo uso de Microwave Office. Dada la eficiencia de este circuito equivalente para modelar el polarizador, el circuito se utiliza para optimizar los valores de ciertas impedancias para un determinado ángulo de incidencia y frecuencia de trabajo.
  Una vez se conocen los valores de estas impedancias se produce a una optimización de las dimensiones del meandro para conseguir estos valores de impedancias. Esta segunda optimización se lleva a cabo mediante el uso de HFSS.
  Utilizando este método de optimización, esta sección analiza los resultados para los casos de optimización para incidencia ortogonal y optimización para incidencia oblicua. Concluyendo que este método de optimización es efectivo y da lugar a modelos de polarizador que funcionan bajo las condiciones utilizadas en la optimización. Estos modelos podrían se utilizados para construir un polarizador con diferentes secciones que realice el cambio de polarización de forma correcta para todos los haces del sistema.

Sección 4: Reducción del acoplo entre alimentadores

En esta sección se ha caracterizado el problema del acoplo entre alimentadores adyacentes mediante la toma de medidas para diferentes situaciones de los alimentadores haciendo uso de un analizador de red.

Una vez caracterizado el problema se plantea un método para reducir el acoplo basado en el cambio de la distribución de los alimentadores haciendo uso de los resultados obtenidos en el experimento del desplazamiento de la posición del alimentador en la dirección tangente a la lente. Llegando a la conclusión de que el origen del acoplo no esta en el enfrentamiento entre las aperturas de los alimentadores sino en las reflexiones en la superficie de la lente.

Finalmente, teniendo en cuenta que el origen del acoplo reside en las reflexiones sobre la superficie de la lente, se proponen dos posibles alternativas para reducir el acoplo:

- **Lente Luneberg**. Reduce las reflexiones mediante un cambio suave en la permitividad.
- **Esquema de reutilización de frecuencias con filtrado**. Mediante el uso de diferentes frecuencias en alimentadores adyacentes, es posible el uso de filtrado en el circuito de recepción para eliminar el efecto del acoplo.

Sección 5: Sumario y trabajo para el futuro

Esta sección recoge las conclusiones más importantes que se han ido obteniendo durante la realización del proyecto y, basándose en estas conclusiones, propone trabajo para el futuro en el caso de continuar con esta línea de investigación.

Sección 6: Anexos

Esta sección recoge documentos interesantes obtenidos como resultado de la realización de éste proyecto:

- Abstract de la conferencia sobre diseño de sistemas de antenas multi-haz para HAPS presentada para la EuCAP del 2012.
- Dibujo mecánico de las piezas que sujetan los alentadores confiriéndoles la libertad de movimiento requerida
- Dibujo mecánico de las mascaras para construir las capas de líneas de meandro de los prototipos de polarizador.

Introduction

Satellites using low earth orbit (LEO-satellites) are finding increasing use for new communications services in recent years; based on their benefits a new family of stations is currently being studied and developed, the High Altitude Platform Stations (HAPS). With shorter development time and smaller budgets, they can fulfill many of the functions of their larger counterparts.

Generally, satellites are lofted into an orbit which is above the earth from 200 Km to 4000 Km. HAPS are airships or planes, operating in the stratosphere, at altitudes of 17-22 Km typically. At this altitude, they can maintain a quasi-stationary position, and support payloads to deliver a wide range of services, principally communication and remote sensing services.

Compared with geostationary orbit (GEO) satellites, LEO-satellites and HAPS have some important advantages such as closer distance to ground (less power needed, smaller antennas…), smaller time delay, the availability of Doppler effect for position determination, lower cost, more flexibility, although less powerful.

During last years an impressive quantity of work has been carried out on HAPS and their related telecommunication systems as can be checked in [1]. From the antenna point of view, HAPS antenna models have been used in [2] to analyze the performances of HAPS based wireless telecommunication system.

Communications via HAPS will develop broadband capability to deliver cost effective solutions providing a viable alternative to cable and satellite, with the potential to reach rural, urban and travelling users.

HAPS offer an effective way of exploiting mm-wave spectrum by supporting multi-cell architectures. In ITU-R [3] this kind of application is studied and the frequency band to be allocated is defined as 27.5-31.3 GHz. It exposes that the viability of such systems is largely determined by the overall system data capacity, which is in turn governed by the properties of the antenna payload that serves the cells on the ground.

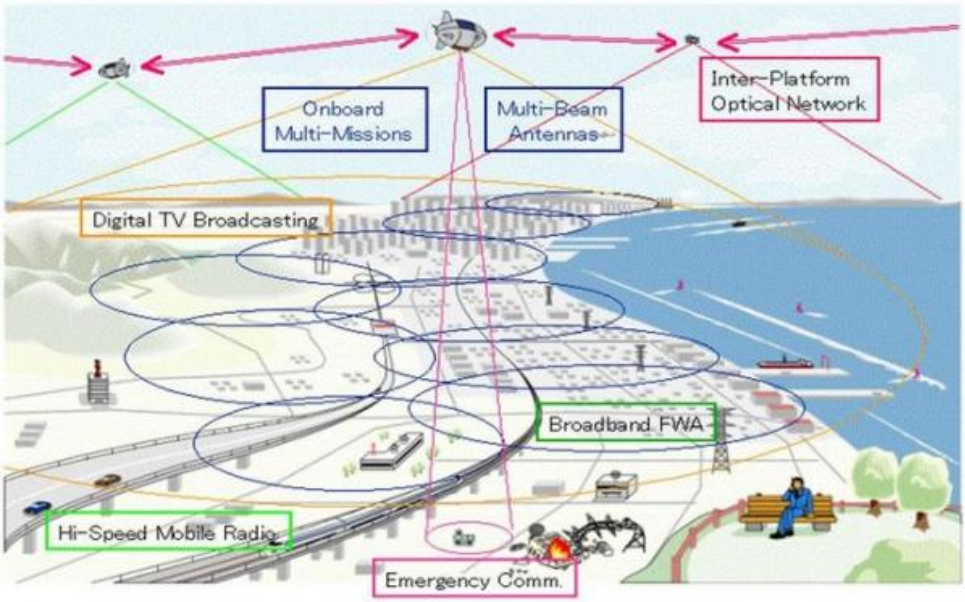

Figure 1. *HAPS services*

Many wireless services, such as GPS and TV broadcasting, need circular polarization to reach high performances. Since these services can be improved by using HAPS because of their intrinsic benefits aforementioned, a circularly polarized multi-beam antenna system is a basic element to be developed for HAPS application.

Therefore, this document presents in section 1 possible antenna systems technologies that could be used in these applications. Then, their drawbacks and potential issues are identified and studied; sections 2 and 3 present the two main problems and propose solutions to overcome them, which are supported by simulations and measurements results. Additionally, although it was not considered within the objectives of the project, an additional problem has been identified and characterized in section 4 where solutions are also proposed and tested by measurements. Finally, new possibilities are presented and summarized in section 7 as possible future work.

Special mention should be done to section 3.3 where extra effort was posed to propose an innovative method for the optimization of meander-line polarizer structures.

1. Scenario & general aspects

This project is part of a much bigger project currently under development in LEMA laboratory at EPFL. From this bigger project several publications have recently emerged in the topic HAPS communications, [4] and [5]. These documents constitute the starting point of this project and thus part of this first section, where the scenario and different general aspects are defined, is based on these previous publications.

1.1. Scenario

This section describes the scenario characteristics based on the requirements for wireless communications via HAPS according to a concept currently under investigation in Switzerland. These characteristics have been used to set the antenna specifications. They consist of a Ka-band (27.5-31.3 GHz) multi-beam antenna mounted on a platform at the standard height of 21 Km and providing 7 spot beams on the ground as explained in [6], it should allow multi-cell architecture and spectrum reuse as described in [7-10]. Additionally, as many wireless communications services need using circular polarization another requirement for this scenario is to achieve circular polarization.

Taking into account global system considerations, it has been decided that the spot beams should be arranged in an overlapping hexagonal grid and every beam should guarantee an effective ground coverage in the form of a 5 Km diameter circular cell as shown in Figure 1.1.1. *Typical beam overlaps used for multi-beam antenna designs are -3 dB for two adjacent beams, and -4 dB for three adjacent beams*, [11]. Therefore, it has been decided to use a beams overlap level equal to -4 dB and thus the circular cell boundaries on ground shown in Figure 1.1.1 correspond to a -4 dB beam aperture. This strategy ensures uniform coverage in the ground.

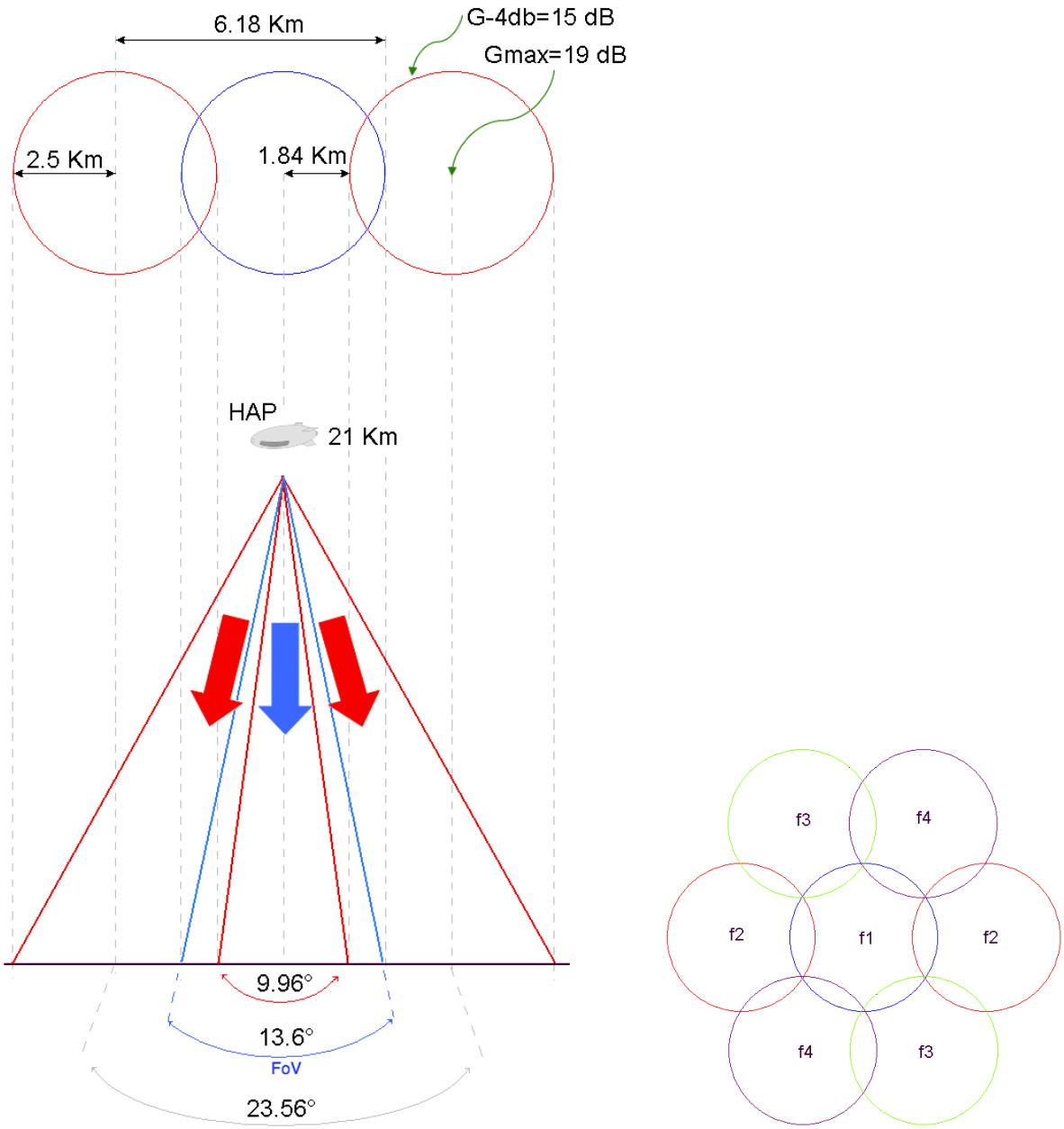

Figure 1.1.1 *Multi-cell scheme geometry and spectrum reuse scheme*

The Field of View angle (FoV) associated to this cell diameter can be simply obtained from the geometrical properties of the scenario exposed in Figure 1.1.1 as follows:

$$\mathrm{FoV} = 2\arctan\left(\frac{\mathrm{R_{cell}}}{\mathrm{H_{HAPS}}}\right) = 13.6° \qquad (1.1.1)$$

Link budget can be defined to provide different levels of service, some link budgets related with HAPS scenario can be observed in [12]. In this particular project scenario, global link budget considerations imply a minimum antenna gain of G = 19 dB.

Table 1.1.1 below summarizes the resulting scenario characteristics, which set the antenna specifications considered for this project:

Frequency	27.5-31.3 GHz
Bandwidth	3.8 GHz ≅ 13%
Gain	19 dB
H_{HAPS}	21 Km
FoV	13.6°
R_{cell}	2.5 Km

Table 1.1.1. *Scenario*

One of the most important parameters in the design of cellular systems is the Signal to Interference Ratio (SIR), which needs to be high enough to provide service. Thus, in order to minimize the interference signal (i.e. undesired signal in the same frequency than the desired signal), the spectrum reuse scheme has been designed using 4 different frequencies distributed among cells as shown in Figure 1.1.1.

Therefore, this scenario will define the SIR in the worst case as follows, [13]:

$$SIR = \frac{P_{Tx}G(\theta_s)(\frac{\lambda}{4\pi d})^2 G_{Rx}}{P_{Tx}G(\theta_i)(\frac{\lambda}{4\pi d})^2 G_{Rx}} = \frac{G(\theta_s)}{G(\theta_i)} \quad (1.1.2)$$

where

P_{Tx} is the transmitted power

$G(\theta_s)$ is the antenna gain in the direction θ_s, i.e. in the travelling direction of the desired signal

$G(\theta_i)$ is the antenna gain in the direction θ_i, i.e. in the travelling direction of the interference signal

d is the distance between receiver and HAPS

G_{Rx} is the receiver gain

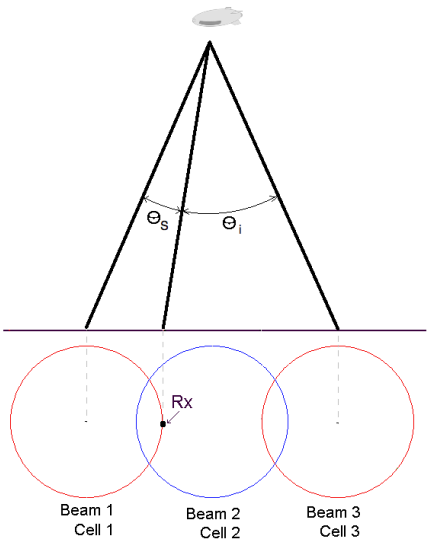

Figure 1.1.2. *SIR computation scenario*

It implies that in this scenario, where sources of the signals are considered to transmit with the same power and receiving antennas are considered omnidirectional, the SIR only depends on the radiation pattern of the HAPS antenna. Consequently, imposing a lower bound in the SIR, the radiation pattern of the HAPS antenna will be more completely defined (it has been already set a restriction of -4 dB in the cell boundary). The resulting radiation pattern characteristics of the HAPS antenna are depicted in Figure 1.1.2.

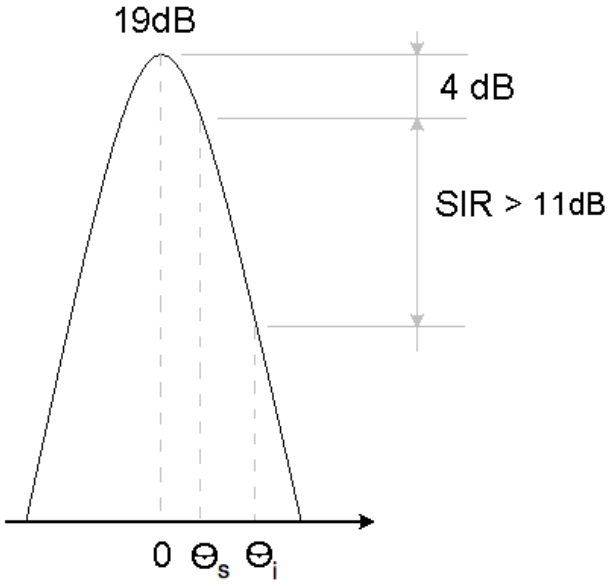

Figure 1.1.2. *Radiation pattern of one single beam*

Where, taking into account the geometrical considerations represented in Figure 1.1.1 and Figure 1.1.2, the angles are defined as follows:

$$\theta_s = \frac{23.56° - 9.96°}{2} = 6.8° \tag{1.1.3}$$

$$\theta_i = \frac{23.56° + 9.96°}{2} = 16.76° \tag{1.1.4}$$

Finally, it is necessary to check the feasibility of the gain requirement. Standard antenna theory [14] provides an upper bound for the theoretical directivity of an antenna having a conical main beam with no sidelobes as:

$$D_{MAX} = \frac{4\pi}{\Omega_{beam}} \tag{1.1.5}$$

where Ω_{beam} is the main beam solid angle, which is usually estimated as [14] :

$$\Omega_{beam} = (\theta_{3dB})^2 \tag{1.1.6}$$

where $\theta_{3\text{dB}}$ is the half-power beamwidth angle (in radians) in any cut of the conical beam. From the specification of the 4dB angle (i.e. FoV), it is possible to obtain $\theta_{3\text{dB}}$ using the cosine square assumption for the pattern as follows:

$$\theta_{3dB} = 0.88 FoV = 12° = 0.2094\ rad \tag{1.1.7}$$

Introducing this value in equations (1.1.3) and (1.1.4), the maximum theoretical directivity that can be achieved is 25.4 dBi. Thus, it provides a wide margin in the design of a 19 dB gain antenna.

1.2. Strategies & technologies

In order to develop a multi-beam antenna system able to provide multi-cell coverage in the scenario exposed in section 1.1 where each beam must present the radiation pattern described in Figure 1.1.2, several strategies and technologies where studied. This section shows an overview of the considered alternatives.

1.2.1. Radiators

1.2.1.1. Printed array

Usually the radiation pattern of a single element is relatively wide, a common technique to increase the directivity without increasing the electrical size of this single element is to form an assembly of radiating elements in an electrical and geometrical configuration.

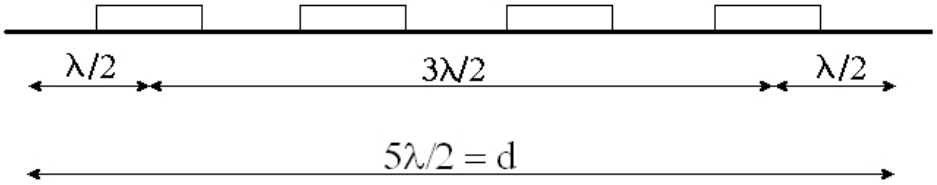

Figure 1.2.1.1.1. *Side view of a 4x4 printed array*

According to [15], the directivity of an 4x4 patch array at 30 GHz can be computed as (taking into account Figure 1.2.1.1.1):

$$D = \frac{A}{\lambda^2}4\pi = \frac{d^2}{\lambda^2}4\pi = \frac{0.025^2}{0.01^2}4\pi \approx 78.5 \Rightarrow 19dB \quad (1.2.1.1.1)$$

and the relation between directivity and HPBW is given by:

$$D = \frac{32400}{\theta_x \theta_y} \Rightarrow \theta_x = \theta_y = 20° \quad (1.2.1.1.2)$$

where

θ_x is the HPBW on the x direction

θ_y is the HPBW on the y direction

The array configuration could be changed in order to enhance its characteristics as follows:

	D	$\boldsymbol{\theta_x \cong \theta_y}$
4X4	19dB	20°
8X8	24dB	11.3°
16X16	29dB	6°

Table 1.2.1.1.1. *Printed array configurations*

Using this technology multi-beam could be achieved in two different ways: using different planar arrays opportunely positioned in different planes. The arrays are the same, and each array radiates broadside (Figure 1.2.1.1.2.(a)). Or all the arrays belong to the same plane but each array has a different radiation pattern (Figure 1.2.1.1.2.(b)), in this case each beam points to a different direction due to the phase of the alimentation of each array.

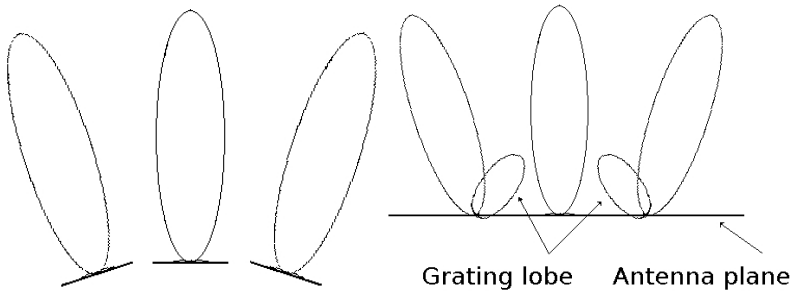

Figure 1.2.1.1.2. *Multi-beam array alternatives*

Finally, in order to achieve circular polarization an external polarizer should be used in combination these printed arrays.

This strategy presents some advantages such as low profile, low cost, easy manufacturability, and configurability. However, its feeding network is complex and it cannot handle very high powers.

1.2.1.2. Helix antenna

A conducting wire bended in the form of a helix constitutes an electromagnetic radiator where the radiation characteristic of the antenna can be tuned by controlling the size of its geometrical properties. The main benefit of using this strategy in the scenario exposed in section 1.1 is that although its general polarization is elliptical, circular polarization is easily achievable over different frequency ranges. This technology is already used for GPS system and for satellite communications [16].

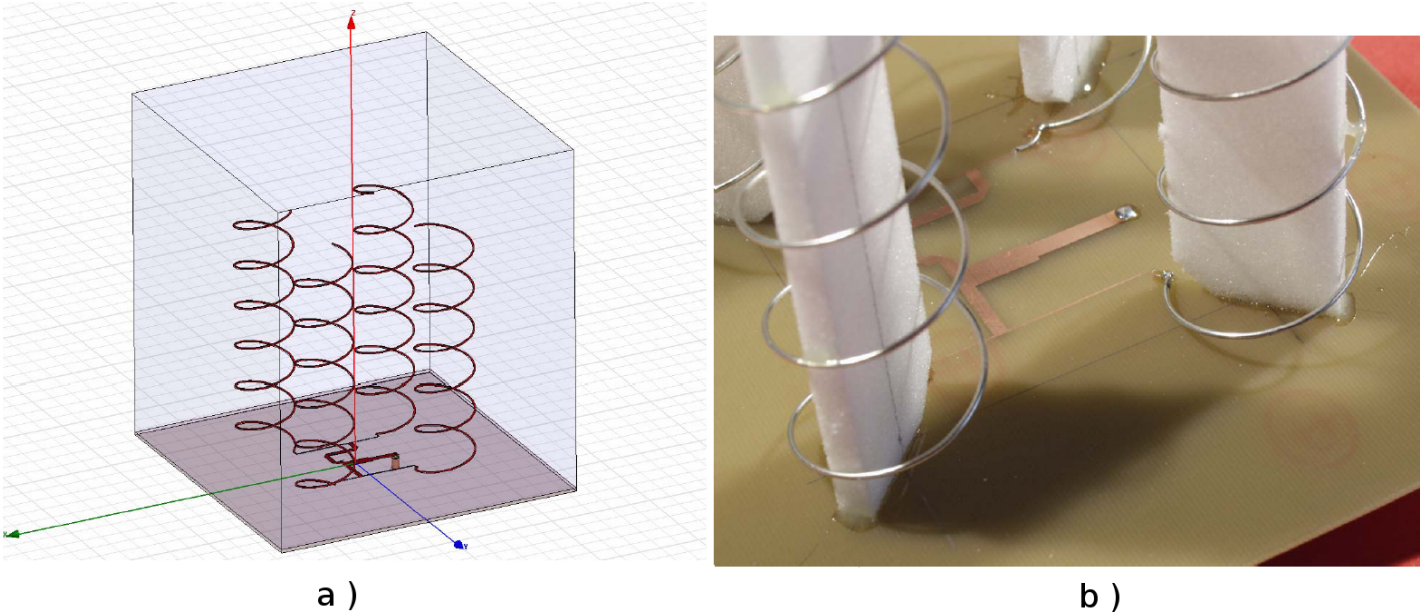

Figure 1.2.1.2.1. *(a) HFSS model, (b) prototype*

This antenna can be also used to conform an antenna array to enhance its performance as shown in Figure 1.2.1.2.1, using an array the maximum possible directivity that can be achieved is up to 33 dB. The prototype shown in this figure was tested in LEMA to check its performance obtaining the following results:

Frequency	3.5 GHz
S_{11} at 3.5 GHz	-22dB
G	13.7 dBi
$Beamwidth_{-10dB}$	35°
BW_{-10dB}	700MHz
Dimensions	150x150 mm

Table 1.2.1.2.1. *Helix antenna properties*

It does not accomplish the requirements exposed in section 1.1, but its performance can be improved by increasing the number of elements in the array.

Therefore, this strategy presents some advantages such as circular polarization, low cost and beam shape strongly dependent in the antenna design. However, it presents a big volume, helixes are difficult to manufacture for 30GHz applications and mechanical delicate. In addition, the feeding network was implemented in a microstrip circuit that limits the power handling.

1.2.1.3. Waveguide feed in combination of a lens

A different alternative could be to use simple waveguide radiating elements that does not produce a directive radiation pattern, but used in combination with a lens the radiation will be focused to achieve the desired behavior. Using this technology not only interesting focusing properties (gain up to 30dB) can be achieved but also multiple beams can be easily achieved by using one lens fed by several feeds as shown in Figure 1.2.1.3.1.

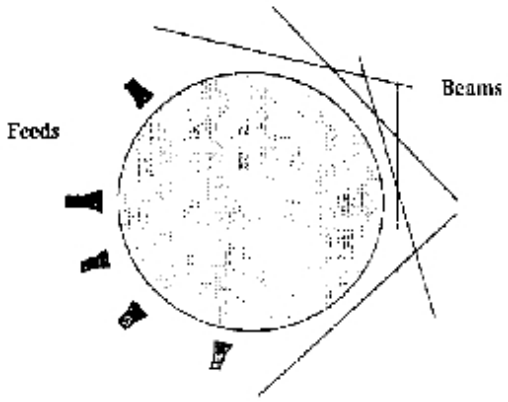

Figure 1.2.1.3.1. *Waveguide feeds in combination of a lens*

Although the volume of this antenna system could be considered as a big drawback, it presents a very important advantage that makes this system worth to be studied. As the feeds are waveguides, which in turn are going to be fed by a coaxial line as it is going to be explained next, they present a huge capacity in power handling. Additionally, interaction with the lens can be controlled by designing a proper horn and the EM interaction between different feeds is low by using waveguide technologies because each feed is mechanically independent from the others Therefore, this technology is the one that has been chosen in the scope of this project to be studied in depth.

Next, an overview of the feed design that was carried out is presented. In Figure 1.2.1.3.2 the general sections conforming the feed are depicted.

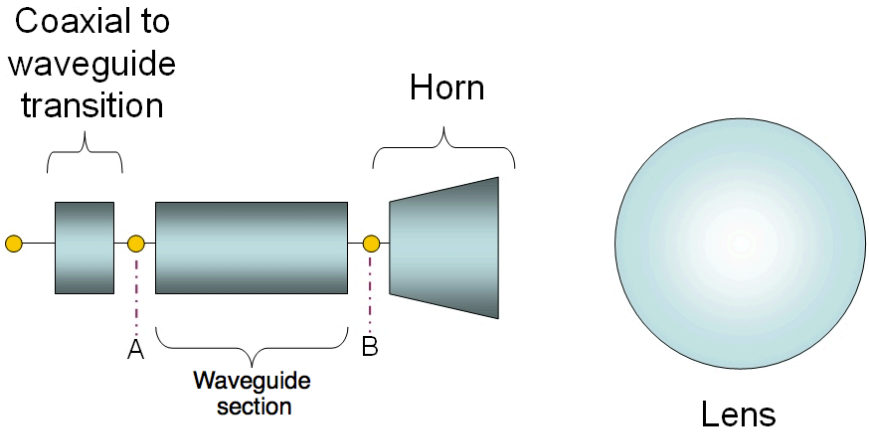

Figure 1.2.1.3.2. *Feed sections*

The coaxial to waveguide transition allows to excite the fundamental mode in circular waveguide, this part plays an important role in the antenna system because determines the bandwidth of the antenna. In the waveguide section if higher modes appear they will be evanescent and after this section only the fundamental mode will be propagating. Since the fundamental mode in circular waveguide is linear polarized a polarizer is necessary to achieve circular polarization, but this will be discussed in section 1.2.3. Since the impedance of a circular waveguide is different from the impedance in free space, a horn has to be designed to transform it smoothly. Moreover, the horn helps to illuminate the lens properly.

Antenna characteristics are especially sensitive to the coaxial to waveguide transition and thus it is going to be explained in more detail. The most efficient way to excite the fundamental mode in circular waveguide via coaxial connector is shown in Figure 1.2.1.3.3, where the external coaxial conductor is welded to the waveguide and the internal coaxial conductor goes into the waveguide to couple the electromagnetic field. The internal coaxial conductor is orthogonal to the longitudinal waveguide internal wall to excite the fundamental mode.

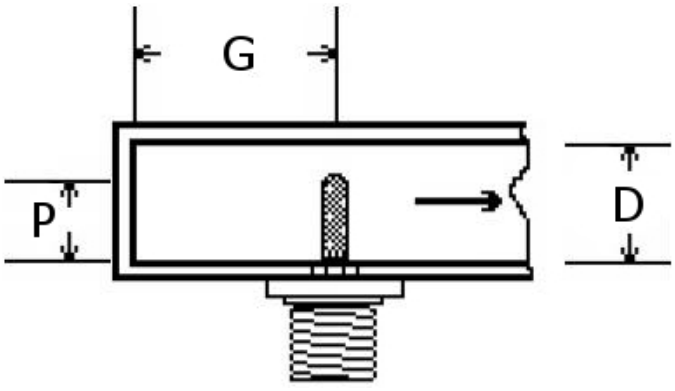

Figure 1.2.1.3.3. *Coaxial to waveguide transition*

The distance G between the coaxial pin and the waveguide ending selects the feed working frequency, while the pin depth P plays an important role to determine the bandwidth. And the waveguide is a standard circular waveguide for mono-modal applications in Ka-Band whose diameter D is 7 mm.

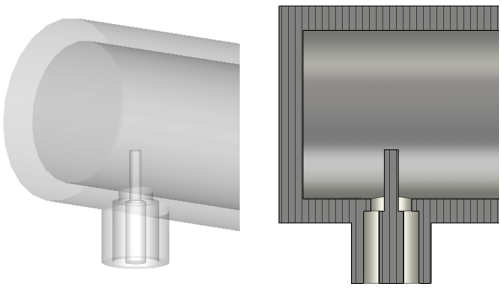

Figure 1.2.1.3.4. *CST modeling of coaxial to waveguide transition*

As it can be seen in Figure 1.2.1.3.4, the transition section has been modeled in CST Microwave Studio where dimensions G and P have been optimized for communications in Ka-band. Ensuring a return loss lower than -25 dB between 27.5 GHz and 31.3 GHz by choosing the values in Table 1.2.1.3.1.

G	3.72 mm
D	7.3 mm
P	2.05 mm

Table 1.2.1.3.1. *Optimum parameters of the coaxial to waveguide transition*

A 2.4 mm Bulkhead Connector Assembly, whose physical characteristics can be observed in Figure 1.2.1.3.5, was used as transition because it presents good performances up to 60GHz.

Figure 1.2.1.3.5. *2.4 mm Bulkhead Connector Assembly*.

The aperture of the horn and its length are optimized to improve the reflection coefficient of the structure. A big aperture improves the matching between waveguide and free space but also increases the feed directivity. In a multi-feed scenario, large apertures would also result in restrictions concerning the angular distances between feeds. Moreover, the lens needs to be illuminated by a moderately directive primary source, thus it is not convenient to design a large and highly directive horn aperture. Final dimensions are shown in Figure 1.2.1.3.5 below.

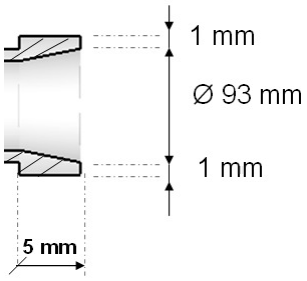

Figure 1.2.1.3.5. *Optimum parameters of the horn.*

Finally, it could be interesting to summarize the benefits of using this technology in comparison with the technologies shown in previous sections 1.2.1.1 and 1.2.1.2 for HAPS applications:

- The use of waveguide feeds allows to handle high power;
- Interaction with the lens can be controlled by designing a proper horn;
- Using waveguide technologies, each feed is mechanically independent from the others. This usually leads to a weak electromagnetic coupling between feeds (on the other hand, if printed feeds were used, they would typically share the same substrate thus increasing the chances of mutual coupling through, for instance, surface waves)
- Waveguide feeds can be accurately and inexpensively realized in aluminum or brass by using digital milling machines;
- Circular polarization is easily achievable by combining circular waveguides and polarizers.

1.2.2. Lenses

In last section 1.2.1, it was exposed that the chosen radiator technology needs to focus the outcoming beam by means of a lens. Thus, this section describes different alternative lenses that could be used for this purpose.

1.2.2.1. Spherical homogeneous dielectric lens

A spherical dielectric lens presents the same focusing aperture in all directions, and hence theoretically it can support any number of simultaneous beams in arbitrary directions. In practice, of course there is a limit to the number and direction of beams. A spherical lens properly designed gives far-field radiation patterns similar to those of parabolic reflectors of comparable size.

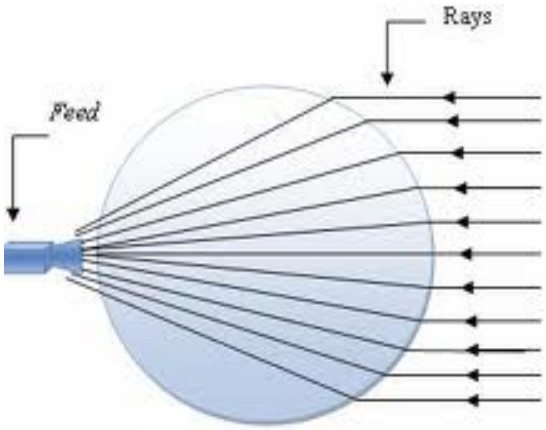

Figure 1.2.2.1.1. *Focusing effect of a spherical homogeneous dielectric lens*

The cross sectional area of the lens, A, can be estimated from the desired directivity by using a classical formula [14]:

$$A = \frac{\lambda^2}{4\pi} D \qquad (1.2.2.1.1)$$

where λ is the central frequency wavelength. This results in a lens radius R of 30 mm. Thus, taking into account that the horn aperture diameter is 95 mm, in order to acheive a correct illumnination of the lens the minimum distance between the center of the lens and the horn aperture has to be 49 mm.

On the other hand, the lens focal point distance F (the distance between the lens center and its theoretical focal point) is given by the following formula valid for small angles and homogeneous dielectric lens [17]:

$$F = \frac{Rn}{2(n-1)} \quad (1.2.2.1.2)$$

where n is the refractive index of the lens material. Choosing Teflon as dielectric material, the expression is reduced to:

$$F=1.61R \quad (1.2.2.1.3)$$

and hence for a lens radius R of 30 mm the resulting focal distance is equal to 48.3 mm. So this consists in an optimum design where the horn apertures can be placed practically at the focal distance of the lens to properly illuminate the lens.

1.2.2.2. Luneburg lens

An ideal Luneburg lens will focus a plane wave precisely to a point on the lens surface. This is achieved by the continuous variation of the dielectric constant as a function of radius [18]:

$$\epsilon_r = 2 - r^2 \mid r = \frac{R}{R_o} \quad (1.2.2.2.1)$$

where

ϵ_r is the relative permittivity

R is the radius

R_o is the lens outer radius.

Unfortunately, such a lens cannot be practically constructed. The lens can be approximated, however, by a quantized version with a finite number of spherical concentric shells, which is more easily realizable. A graphical representation of the relationship between index of refraction and lens radius is shown in Figure 1.2.2.2.1 where three different focusing radius cases are exposed ($R_f \equiv$ focal radius of the lens).

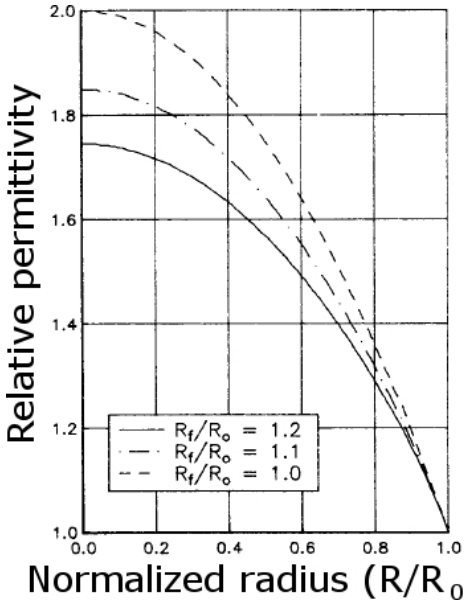

Figure 1.2.2.2.1. *Relative permittivity as a function of lens radius in Luneburg lenses*

The solid curve (R_f/R_o= 1.0) is the standard Luneburg lens described by equation 1.2.2.2.1. Since R_f equals R_o, a lens with this permittivity variation will focus to a point on its outer surface. Each of the remaining curves describes a permittivity variation for a lens which presents its focal point some distance away from its surface.

A practical realization example of a Luneburg lens and its focusing effect can be observed in Figure 1.2.2.2.2 below.

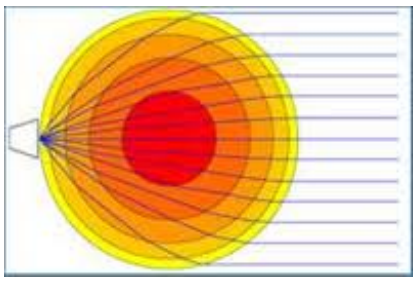

Figure 1.2.2.2.2. *Focusing effect in a Luneburg lens*

The quantized version of the Luneburg lens consists of a finite number of shells approximating the continuous variation of dielectric constant given by equation 1.2.2.2.1. Having a non continuous variation of the dielectric constant implies two different effects: first, the focusing point will be placed some distance away from its surface (focusing error); in addition, due to the discontinuities between different permittivity shells, reflections appears in each material interface. These two effects are a function of the number of shells used to make up the lens, and the method of incrementing the shells.

Different quantization methods are available in literature for selecting the radius and dielectric constants of the shells, and it was found that the best incrementing method for an antenna is a function of the feed pattern. Analysis of various incrementing schemes through numerical computer simulation has indicated that incrementing by constant ratio of index of refraction from one shell to the next was near optimal for broad beam feeds, and that incrementing by constant steps in radius worked reasonably well.

On other hand, the number of shells has demonstrated to be even more relevant than the quantization scheme for the lens behavior. It is obvious that by increasing the number of shells, the lens behavior gets closer to the ideal one and therefore, theoretically, the performances of the lens improve. But it was found in [18] a study in the number of shells that demonstrate that there is a threshold effect, and that above a given, and quite small, number of shells both the directivity and side lobe levels no longer improve. The parameters defining the quantized Luneburg lenses used in this study, which come from the discretization of equation 1.2.2.2.1, are shown in Table1.2.2.2.1 below and the resulting directivity and sidelobe levels for each of them can be analyzed in Figure 1.2.2.2.3.

N	shell normalized radii	shell relative permettivity
1	0.82	1.67
2	0.63 0.89	1.80 1.4
3	0.53 0.75 0.93	1.86 1.57 1.28
4	0.47 0.67 0.82 0.94	1.88 1.67 1.44 1.22
5	0.43 0.60 0.74 0.85 0.95	1.91 1.73 1.55 1.36 1.18
6	0.39 0.56 0.68 0.78 0.88 0.96	1.93 1.77 1.61 1.46 1.31 1.16
7	0.37 0.52 0.63 0.73 0.82 0.89 0.97	1.93 1.80 1.67 1.53 1.40 1.27 1.13
8	0.34 0.49 0.59 0.69 0.77 0.84 0.91 0.97	1.94 1.82 1.71 1.59 1.47 1.35 1.24 1.12

Table 1.2.2.2.1. *Radius and permittivity of shells for quantized Luneburg lenses*

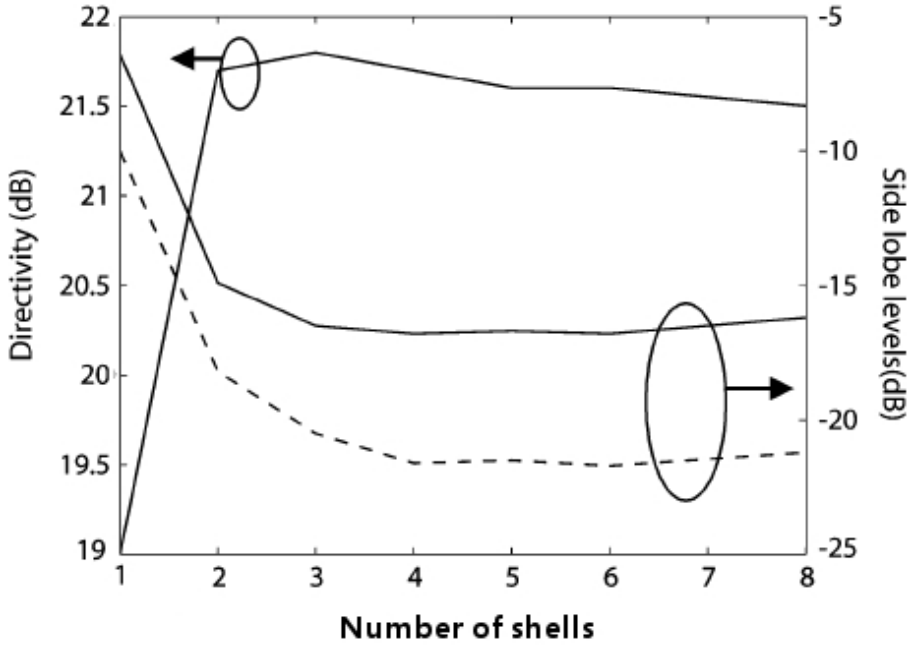

Figure 1.2.2.2.3. *Directivity and sidelobe levels as a function of number of shells for quantized Luneburg lenses*

Taking into account these results, it is reasonable to use a small number of shells to reduce the manufacturing difficulty and thus the air gap effects that can alter significantly the lens antenna performances.

Although the Luneburg lens exhibits a better performance that the homogeneous spherical lens, as it is going to be showed in section 1.2.4 by means of simulation results, using the homogeneous spherical lens requirements are met and obviously its fabrication is much simpler and thus cheaper than for the Luneburg lens. Therefore, the homogeneous spherical lens is the option that is going to be implemented and studied in the complete system for the scope of this project.

1.2.3. **Polarizers**

As it has been already mentioned in the introduction and in Section 1.1, many wireless communications services need using circular polarization and, as it has been highlighted in section 1.2.1.3, the polarization coming out of the antenna system that has been decided to use (i.e. cylindrical waveguide terminated in a horn combined with a spherical lens) is linear. Therefore, it is necessary to include a polarizer that transforms the polarization from linear to circular.

The design of a polarizer fulfilling the requirements intrinsic to the scenario has been the key point (i.e. the task implying more time devoted and effort) during the development of this project. Consequently, the study of this technology presented in this section constitutes a much deeper analysis compared with previous sections.

First some introductory concepts are going to be exposed in section 1.2.3.1 to understand what a polarizer is, and then different strategies to achieve this polarization conversion are analyzed in sections 1.2.3.2, 1.2.3.3 and 1.2.3.4.

1.2.3.1. Introductory concepts

Polarization

Polarization of a radiated wave is defined as *the property of an electromagnetic wave describing the time varying direction and relative magnitude of the electric field vector; specifically, the figure traced as a function of time by the extremity of the vector at a fixed location in space, and the sense in which it is traced, as observed along the direction of propagation,* [14]. According to this definition, if an incoming wave is observed from a fixed spatial point, the observer will perceive a rotation of the electric field vector during time as illustrated in Figure 1.2.3.1.1 (a) and the polarization property of this electromagnetic wave is the geometric figure described by the end of this vector from an observation point facing the direction in which this wave propagates as shown in Figure 1.2.3.1.1(b). The plane containing the electric and magnetic fields is called the plane of polarization and it is orthogonal to the direction of propagation, this is the plane where the polarization ellipse is described.

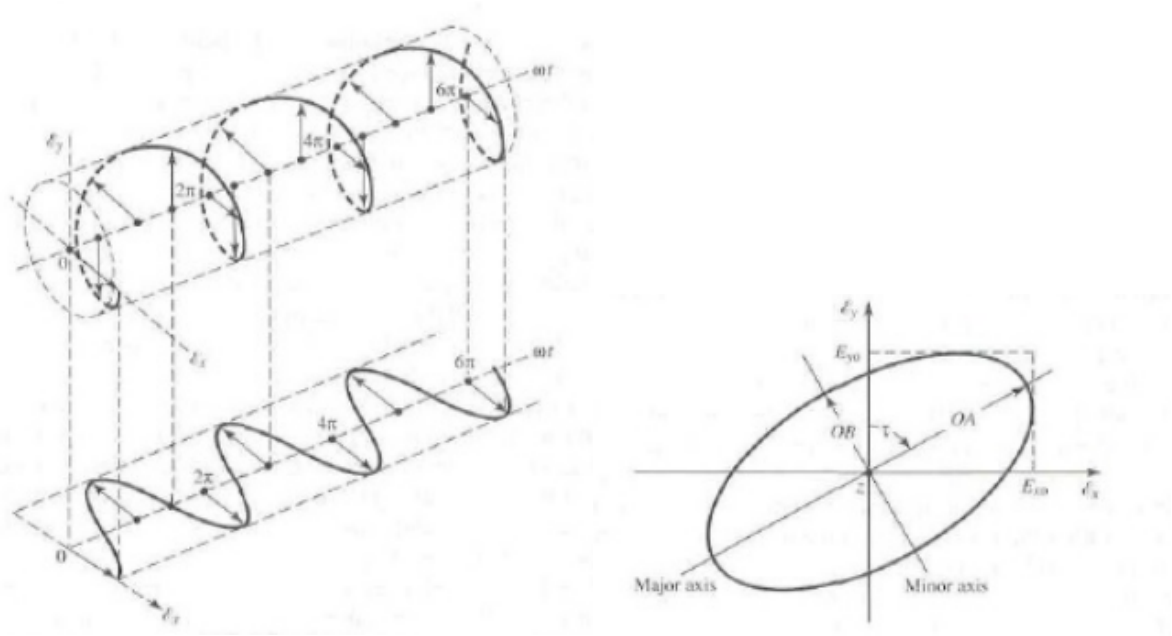

(a) Rotation wave (b) Polarization ellipse

Figure 1.2.3.1.1 *Rotation of a plane wave and its polarization ellipse at z=0 as a function of time. [14]*

As stated in [19], the main concern in antenna engineering is the polarization properties of plane waves or of waves that can be considered to be planar over the local region of observation, and for plane waves we need only to specify the polarization properties of the electric field vector since the magnetic field vector is simply related to the electric field vector.

It is also important to remark that the polarization of an antenna in a specific direction is defined to be the polarization of the far-field wave radiated in that direction from the antenna. Usually, the polarization of an antenna remains relatively constant throughout the main lobe, but it varies considerably in the minor lobes. Therefore, when we design an antenna or a polarizer to provide a specific polarization, we will study the resulting polarization in the far-filed region and within the area of the main lobe.

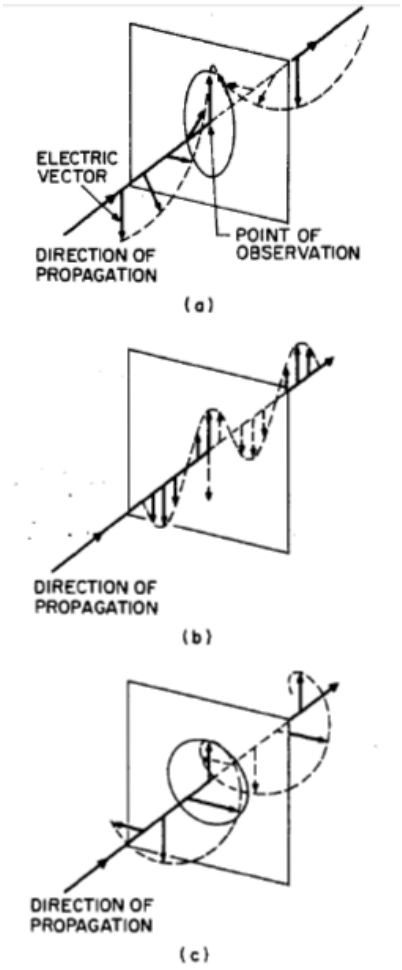

Figure 1.2.3.1.2 *(a) Elliptical polarization. (b) Linear polarization. (c) Circular polarization (right-hand). [19]*

Polarization may be classified as linear, circular, or elliptical. All these three cases are graphically represented in Figure 1.2.3.1.2. In general, the figure that the electric field traces is an ellipse, and the field is said to be elliptically polarized. However, exist two special cases of the elliptical polarization which are of major importance: when the vector that describes the electric field of a transverse electromagnetic wave at a point in space as a function of time is always directed along a line, we can consider that the ellipse presents a major axis extremely bigger than the minor one and it is known as linear polarization (LP); in the opposite case, when both axis present the same dimension the ellipse becomes a circle and it is known as circular polarization (CP).

In order to complete the definition of polarization we should take into account the sense of the wave's rotation, and there are two possibilities: the figure of the electric field is traced in a clockwise (CW) or counterclockwise (CCW) sense. CW rotation of the electric field vector is designated as right-hand circular polarization (RHCP) and CCW as left-hand circular polarization (LHCP).

Now some parameters that characterize the polarization are going to be mathematically described in order to be able to measure the quality of the results produced by a polarizer. The instantaneous field of a plane wave, propagating in the negative z direction, can be defined as:

$$E(z,t) = \hat{a}_x \cdot E_x(z,t) + \hat{a}_y \cdot E_y(z,t) \qquad (1.2.3.1.1)$$

Where the instantaneous components are given by:

$$E_x(z,t) = E_{xo} \cdot \cos(\omega \cdot t + k \cdot z + \vartheta_x) \qquad (1.2.3.1.2)$$

$$E_y(z,t) = E_{yo} \cdot \cos\left(\omega \cdot t + k \cdot z + \vartheta_y\right) \qquad (1.2.3.1.3)$$

And the amplitudes E_{xo} and E_{yo} are the maximum magnitudes of the x and y components.

Making use of this definition of the instantaneous field the different types of polarization can be more rigorously defined as follows.

- *Linear polarization*. The time-phase difference between the two components must be:

$$\Delta\vartheta = \vartheta_y - \vartheta_x = n \cdot \pi; \quad n = 0, 1, 2, 3, \ldots \tag{1.2.3.1.4}$$

- *Circular Polarization*. The magnitudes of the two components are the same and the time-phase difference between them is odd multiple of $\pi/2$:

$$E_{xo} = E_{yo} \tag{1.2.3.1.5}$$

$$\Delta\vartheta = \vartheta_y - \vartheta_x = \begin{cases} +\left(\frac{1}{2} + 2 \cdot n\right)\pi; & n = 0, 1, 2, \ldots for\ CW \\ -\left(\frac{1}{2} + 2 \cdot n\right)\pi; & n = 0, 1, 2, \ldots for\ CCW \end{cases}$$

- Elliptical polarization. The time-phase difference between the two components is odd multiple of $\pi/2$ and their magnitudes are not the same or the time-phase difference between the two components is not equal to a multiple of $\pi/2$. For this polarization an important parameter can be defined to characterize the polarization: the ratio of the major axis to the minor axis is referred to as the axial ratio (AR).

$$AR = \frac{major\ axis}{minor\ axis}; 1 \leq AR \leq \infty\ or\ 0 \leq AR_{dB} \leq \infty \tag{1.2.3.1.6}$$

  The orientation of the ellipse is specified by the angle between the major axis and a reference direction when viewed looking in the direction of propagation, this is called the tilt angle.

Polarizers

A polarizer is defined as a device designed to transform the polarization of an incident electromagnetic wave, which in most cases arrives with an undefined or undesired polarization, in order to obtain a well-defined polarization fitting our requirements. The most common types of polarizers are the linear and the circular polarizers.

As its name suggests, a linear polarizer provides an output wave characterized by a LP oriented in a defined direction by means of the absorption or reflection of the undesired components of the incoming polarization. Figure 1.2 illustrates how a wire-grid polarizer obtains a vertical polarization. In this example, the electric field components parallel to the wires see the structure as a metallic surface and thus, all their energy is reflected backwards and dissipated by the Joule effect heating the wires because they induce the movement of electrons along the wires. However, the electric field components perpendicular to the wires cannot induce the movement of electrons along a big surface, they do it along the wires' width. Therefore, only a small part of their energy is dissipated or reflected and most of it is able to pass thorough the grid. Linear polarizers, in general, are widespread in common optical applications such as sunglasses or photographic filters.

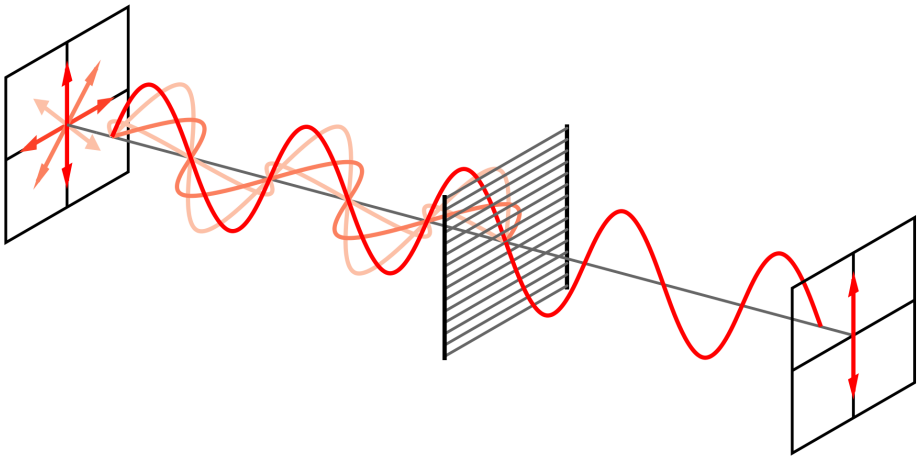

Figure 1.2. *Wire-grid linear polarizer.*

Any wave of arbitrary polarization can be synthesized from two waves orthogonally polarized to each other. For example, if a vertically and a horizontally polarized waves coexist and the two waves have equal amplitude but 0º phase difference, the resulting wave is linearly polarized with 45º orientation. Furthermore, a circularly polarized wave can be produced if each of the two waves has the same amplitude and a 90º phase difference between them. If they have other than the same amplitude and/or other than a 90º relationship, the resulting wave will be elliptically polarized.

Using the above-mentioned theory to synthesize an arbitrary polarization, circular polarizers give us the opportunity to create a circularly polarized wave from a linearly polarized one and vice versa. In order to turn linear into circular polarization, we cannot simply reject certain components, this time we need to modify them in such a way that we obtain a resulting polarization composed out of two orthogonal components with equal amplitude and a phase shift of 90 degrees between them. A graphical representation of this conversion is given in Figure 1.3. Although circular polarizers have become popular nowadays in the non-scientific arena thanks to the 3D movies, they have been in use for electromagnetic applications since 1980's.

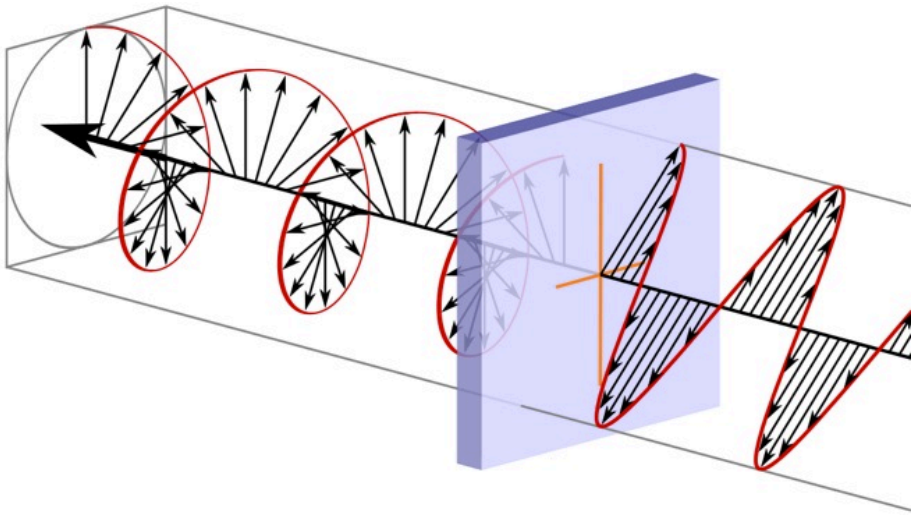

Figure 2. *Conversion from linear to circular polarization.*

The use of circular polarizers in antenna applications presents important advantages, but first of all we should take into account the importance of using CP in communication applications. When the electromagnetic field is transmitted with LP, the output voltage of the receiver is highly dependent in the orientation of the transmitting and receiving antennas. However, this dependence could be reduced using elliptical polarization and it could be minimized for circular polarization. In scenarios where the antennas are located in mobile devices it is really important to minimize the relevance of the antenna's orientation.

On the other hand, the benefit of using circular polarizers is that it could be possible to use very simple linearly polarized antennas and, making use of polarizers, CP will be provided. This way, problems related with the orientation of the antennas will be avoided while maintaining a simple antenna design that could be one of the requirements for a specific application in order to reduce costs by simplifying the manufacturing process.

1.2.3.2. Elliptical sections based polarizer

Based on the studies published in [20], a polarizer developed by the insertion of different iris sections in the waveguide was implemented and studied. This section describes the design and optimization of this polarizer realized in circular waveguide with insertion of elliptical waveguide sections or stretches. The device is compact and it requires to be manufactured by milling techniques only. Figure 1.2.3.2.1 graphically represents a scheme of this variety of polarizers.

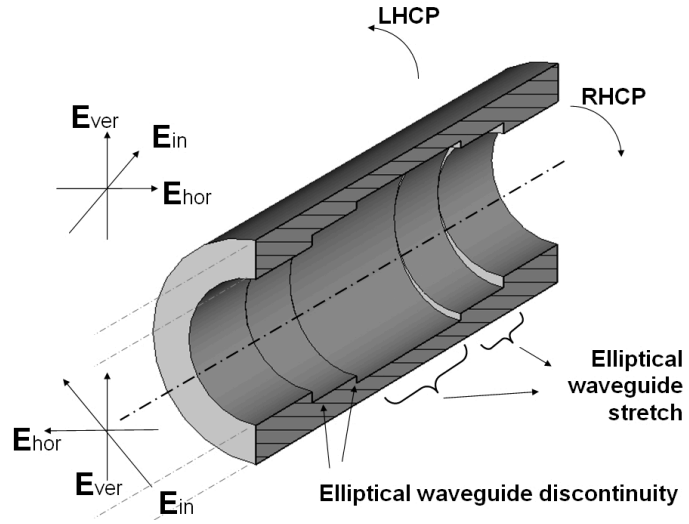

Figure 1.2.3.2.1. *Elliptical sections based polarizer scheme*

An incident vertical field E_{in} may be considered as the superposition of two fields, one with vertical polarization E_{ver} and the other with horizontal polarization E_{hor}. The vertically polarized electric field E_{ver} propagates along a line loaded by essentially capacitive discontinuities, while the field E_{hor} propagates along a line loaded by essentially inductive discontinuities. When the wave comes out of the polarizer, after passing through a certain number of sections, the fields E_{ver} and E_{hor} should have a phase difference equal to 90° in order to acheive the circular polarization as it has been explained in section 1.2.3.1 in the definition of polarizer. RHCP or LHCP is produced depending on the orientation of the incident field, as it can be seen in Figure 1.2.3.2.1.

A full-wave electromagnetic model has been developed using the electromagnetic (EM) simulator CST Microwave Studio, where two different full-wave analyses are necessary, one for each polarization. It is important to highlight here that in the CST modeling a dense mesh has been used to model the most conflictive regions, i.e. close to the elliptical discontinuities and in the coaxial pin area. Once it is modeled, an optimization was performed using three variables to be adjusted:

- Number of the elliptical waveguide stretches;
- Relative distances of elliptical waveguide stretches;
- Major diameter of the elliptical waveguide stretch (minor diameter is chosen to ensure a perfect surface continuity among polarizer and coaxial feed);

and three parameters are used to check the improvement of the optimization:

- Band width (BW) and central frequency;
- Phase difference between polarization components;
- Return loss, actually the reflection coefficient was monitored.

Three different models where studied using there, five and nine elliptical sections respectively. Next, their characteristics and the resulting behavior of the polarizers are going to be shown in the following figures from 1.2.3.2.2 to 1.2.3.10 and tables from 1.2.3.2.1 to 1.2.3.2.3. In the figures where the axial ratio (AR) is analyzed, the AR of the electric field is monitored for $\theta = 0°$ (broadside direction) and for $\theta = 15°$ within the frequency band of interest.

3 sections polarizer

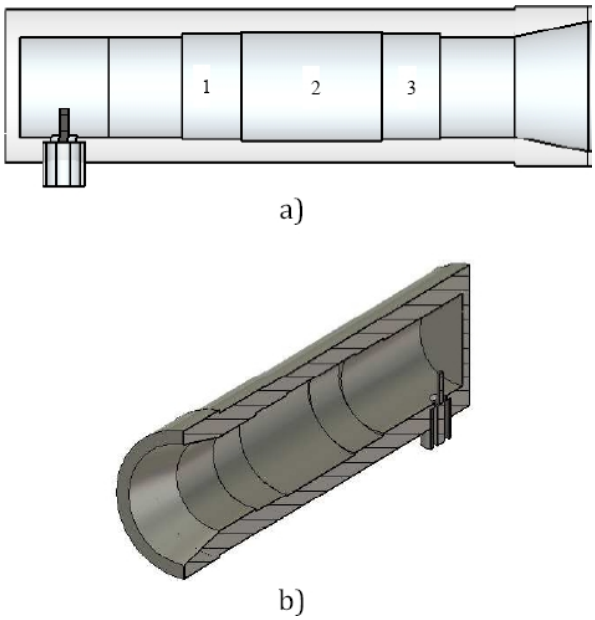

Figure 1.2.3.2.2. *3 sections polarizer scheme*

Section	Length [mm]	Minor Axis [mm]	Major Axis [mm]
1 and 3	$4.0816 \approx \frac{\lambda_g}{5}$	3.5	3.92
2	$9.6928 \approx \frac{\lambda_g}{2.1}$	3.5	4.27

Table 1.2.3.2.1. *3 sections polarizer scheme*

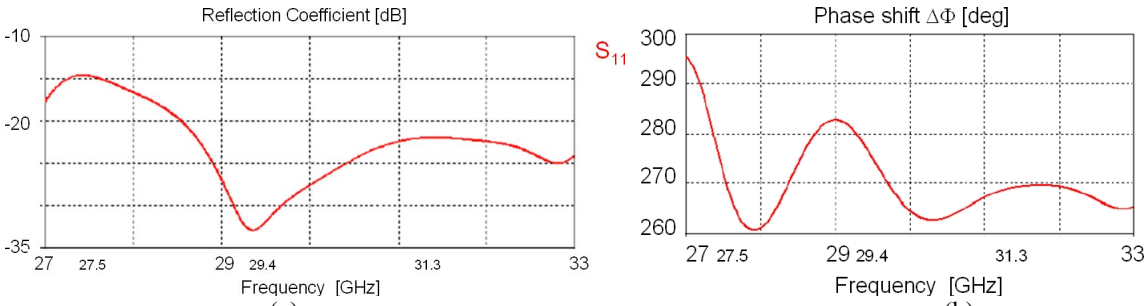

(a) (b)

Figure 1.2.3.2.3. *3 sections polarizer without lens (a) Reflection coefficient, (b) phase difference*

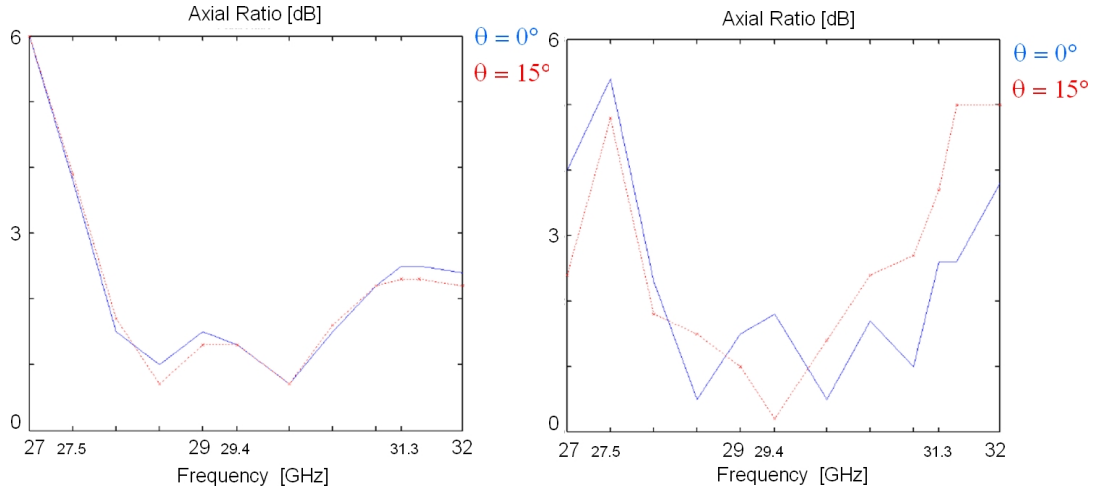

(a) (b)

Figure 1.2.3.2.4. *3 sections polarizer axial ratio (a) without lens, (b) with lens*

As it can be seen in this Figures the polarizer BW in not enough to cover the whole frequency band with a correct performance. Therefore, it has been decided to study an alternative polarizer with more elliptical sections to increase the BW.

5 sections polarizer

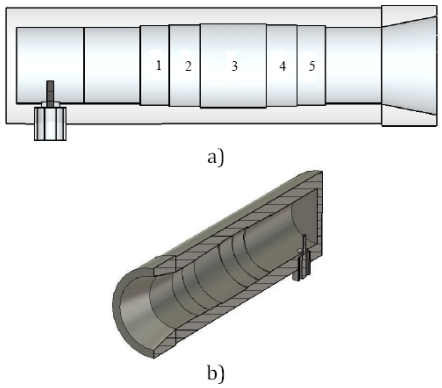

a)

b)

Figure 1.2.3.2.5. *5 sections polarizer scheme*

Section	Length [mm]	Minor Axis [mm]	Major Axis [mm]
1 and 5	$2.624 \approx \frac{\lambda_g}{7.8}$	3.5	3.6686
2 and 4	$2.829 \approx \frac{\lambda_g}{7.2}$	3.5	3.9403
3	$6.068 \approx \frac{\lambda_g}{3.3}$	3.5	4.2120

Table 1.2.3.2.2. *5 sections polarizer scheme*

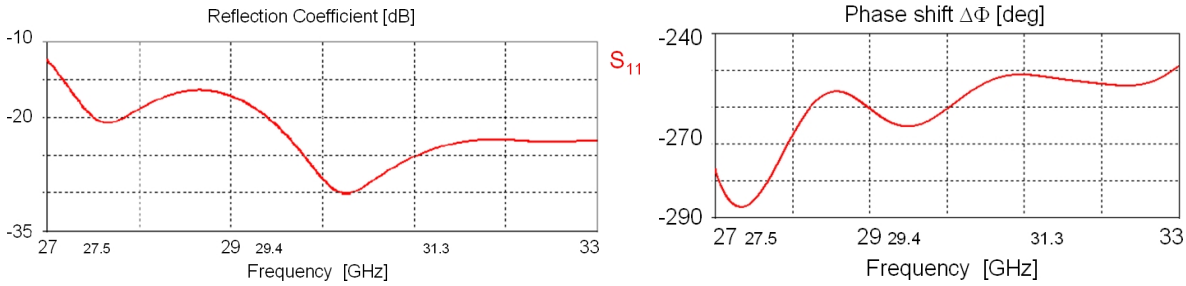

(a) (b)

Figure 1.2.3.2.6. *5 sections polarizer without lens (a) Reflection coefficient, (b) phase difference*

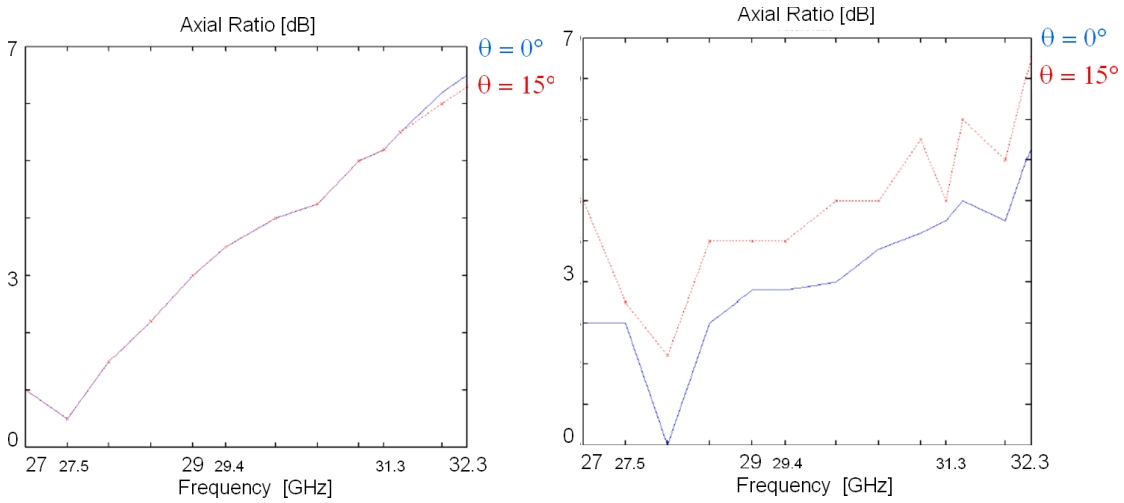

(a) (b)

Figure 1.2.3.2.7. *5 sections polarizer axial ratio (a) without lens, (b) with lens*

As it can be seen in this Figures the polarizer BW in not enough to cover the whole frequency band with a correct performance. Therefore, it has been decided to study an alternative polarizer with more elliptical sections to increase the BW.

9 sections polarizer

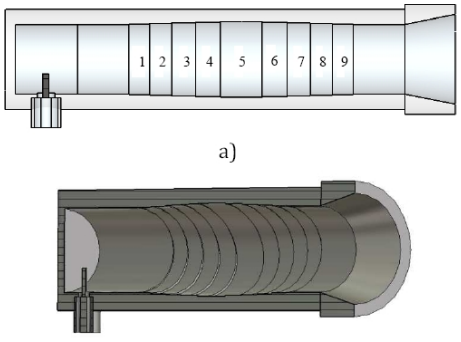

a)

b)

Figure 1.2.3.2.8. *9 sections polarizer scheme*

Section	Length [mm]	Minor Axis [mm]	Major Axis [mm]
1 and 9	$2.624 \approx \frac{\lambda_g}{7.8}$	3.5	3.5668
2 and 8	$2.624 \approx \frac{\lambda_g}{7.8}$	3.5	3.7366
3 and 7	$2.624 \approx \frac{\lambda_g}{7.8}$	3.5	3.9065
4 and 6	$2.624 \approx \frac{\lambda_g}{7.8}$	3.5	4.0762
5	$6.068 \approx \frac{\lambda_g}{3.3}$	3.5	4.2460

Table 1.2.3.2.3. *9 sections polarizer scheme*

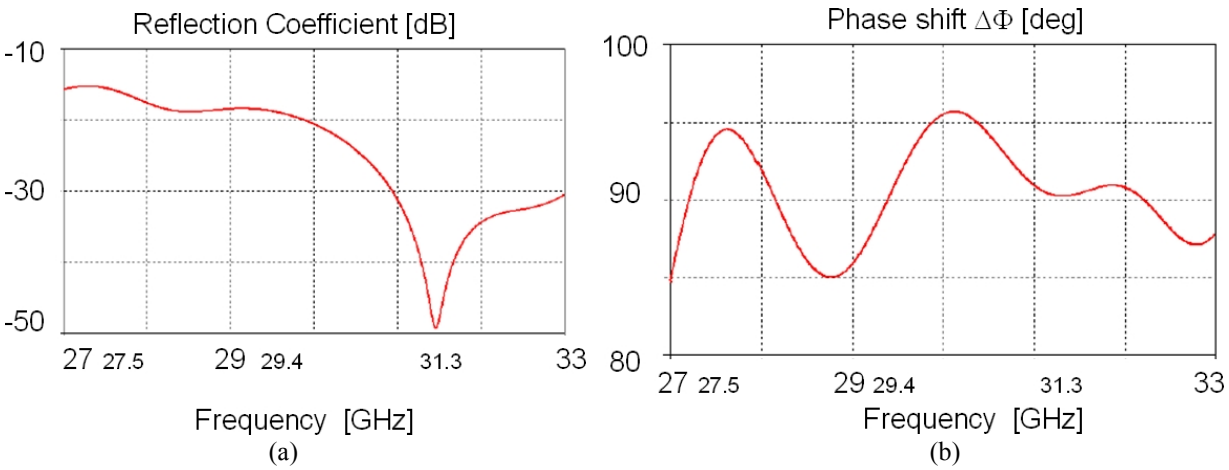

(a) (b)

Figure 1.2.3.2.9. *9 sections polarizer without lens (a) Reflection coefficient, (b) phase difference*

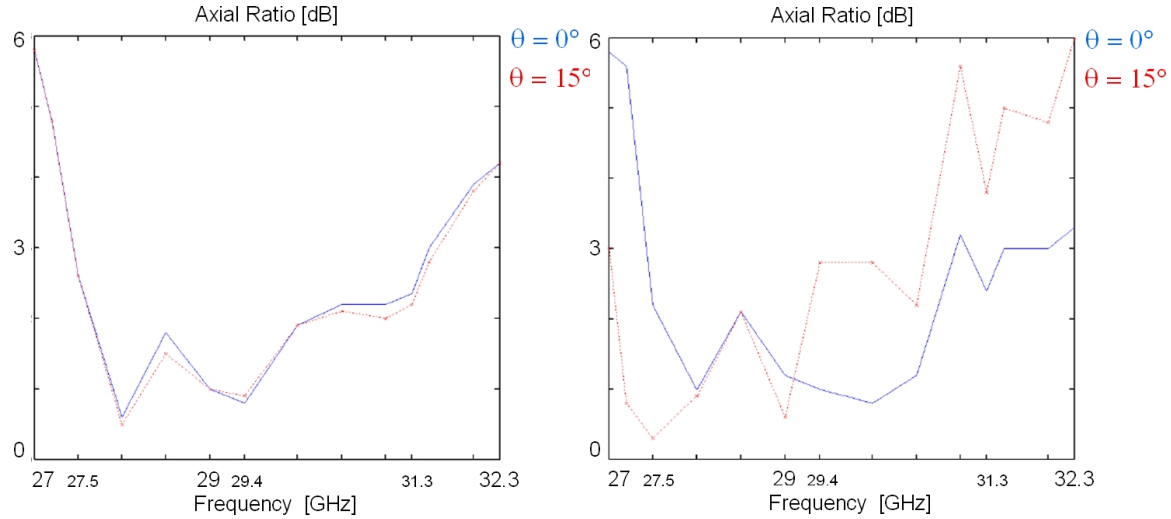

(a) (b)

Figure 1.2.3.2.10. *9 sections polarizer axial ratio (a) without lens, (b) with lens*

Conclusions

From the analysis of the figures above several conclusions can be extracted:

- The return loss decreases as the number of elliptical sections increase
- But it is not possible to assure that the axial ratio is better as the number of elliptical sections increase
- Although the BW is not enough, this polarizer could be used in a sub-band within the Ka-band because it has been demonstrated that the desired directivity is achievable by placing the feed's aperture close to the lens surface.
- The axial ratio is degraded when the wave goes through the lens and this degradation is higher in the case where the observation point is shifted from the broadside direction within the cell.

Due to the degradation caused by the lens this polarizer is not suitable in this scenario because the radiating element is not directive enough without the lens, and thus the use of the lens is mandatory to achieve the radiation pattern depicted in Figure 1.1.2. Consequently, different polarizer alternatives were studied and they are going to be exposed in following sections.

1.2.3.3. Dielectric septum polarizer

A septum polarizer can been designed placing a metal septum ([20], [22]) or a dielectric septum ([23]) at the center of the waveguide where the electric fields are strongest. Metal septum polarizer does not necessitate the presence can work in a narrow band where only the dominant modes are accessible and have a large reflection. To have wide band behavior dielectric septum polarizer is necessary.

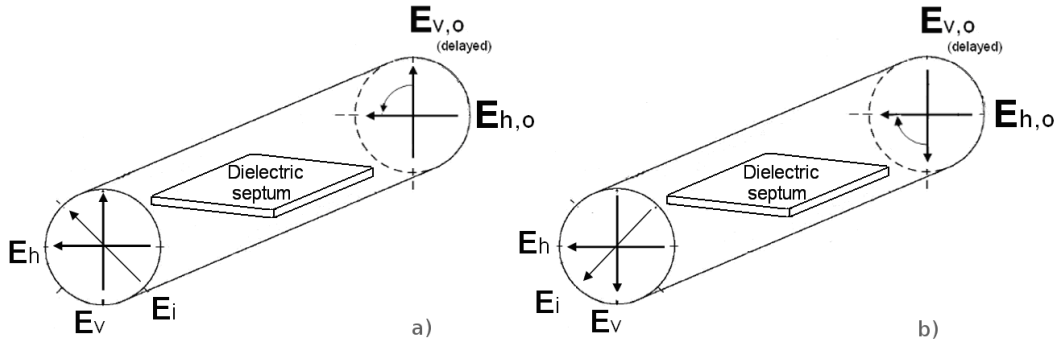

Figure 1.2.3.3.1. *Schematic representation of dielectric septum circular waveguide polarizer. (a) Vertical incident field => LHCP, (b) horizontal incident field => RHCP.*

Figure 1.2.3.3.1 illustrate a schematic view of a circular polarizer with dielectric septum. As it was done in the study of the polarizer shown in section 1.2.3.2, the incident field E_i is decomposed in two orthogonal components E_h and E_v, which in this case are parallel and perpendicular to the dielectric septum respectively and obviously present the same phase. E_i must be inclined 45° with respect to the septum in order to obtain a decomposition in two orthogonal components with equal magnitude. When the wave propagates through the septum region, E_h is strongly perturbed because its electric field lines are parallel to the septum and this electric field is stronger in the septum region. On the other hand, E_v is weakly perturbed because its electric field lines are perpendicular to the septum. Therefore, the polarizer is designed to delay $E_{h,o}$ (i.e. horizontal component of the outgoing wave) as it propagates through the septum region by 90° with respect to $E_{v,o}$ (i.e. horizontal component of the outgoing wave), and hence the outgoing wave is circularly polarized. RHCP or LHCP is produced depending on the direction of the incident field E_i, as illustrated in Figure 1.2.3.3.1.

In order to improve the impedance matching, the rectangular-shaped dielectric septum of Figure 1.2.3.3.1 has been smoothly modified and transformed into the tapered shape shown in Figure 1.2.3.3.2. The tapering at both ends of the dielectric septum has been optimized for matching the impedance for both polarization decompositions.

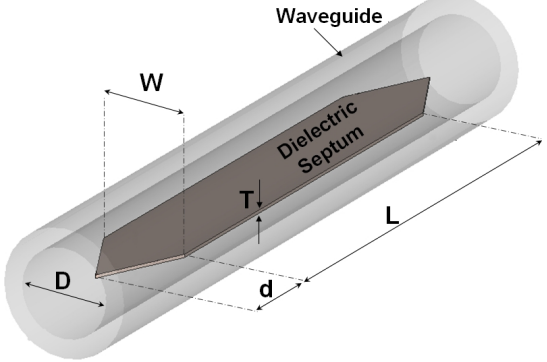

Figure 1.2.3.3.2. *Parameters of a dielectric septum circular waveguide polarizer*

As it was done for the analysis of the polarizer exposed in section 1.2.3.2, a full-wave electromagnetic model has been developed using the EM simulator CST Microwave Studio, where two different full-wave analyses are necessary, one for each polarization. It is important to highlight here that in the CST modeling a dense mesh has been used to model the most conflictive regions, i.e. around the septum polarizer and in the coaxial pin area as it can be seen in Figure 1.2.3.3.3. In order to simplify the optimization design process, the following parameters remained fixed during the process:

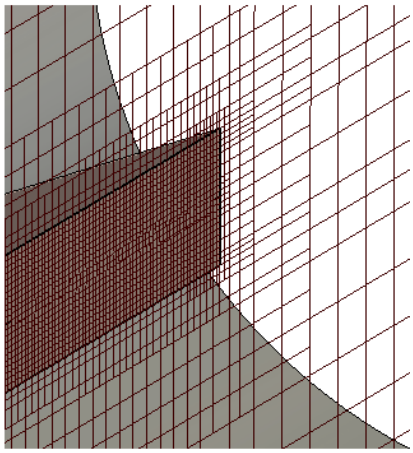

Figure 1.2.3.3.3. *Mesh detail.*

- septum width: *W*;
- septum dielectric constant: ϵ_r;
- septum thickness: *T*.

For mechanical reasons the septum has to touch the internal waveguide wall, so the septum width W must be equal to 7.20 mm in order to ensure a good mechanical contact between septum and waveguide wall. And the dielectric substrate chosen to build the polarizer, which sets ϵ_r and T, is Rogers RT5870 (ϵ_r =2.33,tanδ=0.0012 and T=1.02mm). Therefore, the relevant parameters for the optimization are:

- septum length: L;
- septum end extension (taper length): d.

During the optimization process three parameters are used to check the improvement that the changes imply:

- BW and central frequency;
- Phase difference between polarization components;
- Return loss, actually the reflection coefficient was monitored.

The initial values and bounds of L and d have been chosen according to the recommendations found in [24]. According to this, septum length L should be in the range [λ/2 - λ], where λ is the signal wavelength; whereas taper length d should be in the range [λ/4 - λ/2]. Adjusting the septum length L, the differential phase shift has been controlled. By optimizing d, both the central frequency and return loss can be adjusted. Table 1.2.3.3.1 below reports the final polarizer dimensions.

L	6.20 mm
d	10.67 mm
C	7.30 mm
T	1.02 mm
W	7.20 mm

Table 1.2.3.3.1. *Optimized dimensions of the dielectric septum polarizer*

Until now the analysis of the polarizer has been carried out considering only the case of the isolated polarizer. Now it is going to be analyzed in the real scenario of the feed, i.e. including the coaxial to waveguide transition and the horn as it is shown in Figure 1.2.3.3.4 below.

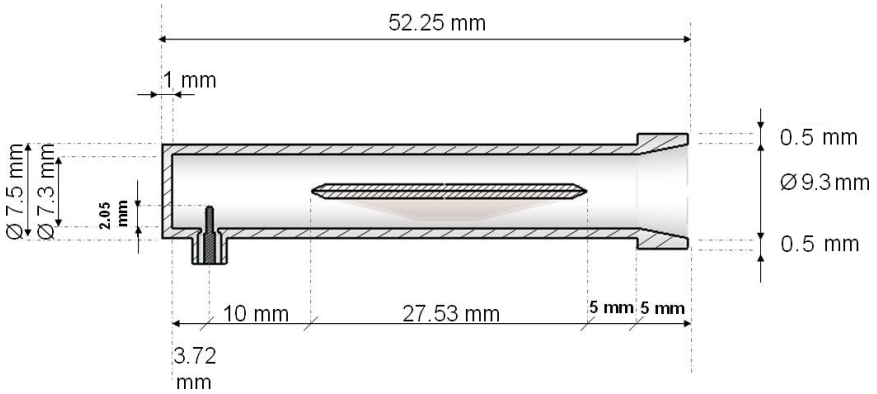

Figure 1.2.3.3.4. *Waveguide feed with dielectric septum polarizer*

The distance between the dielectric septum and the coaxial connector pin is optimized to improve the return loss while keeping the quality of the circular polarization. Since the polarizer is designed to work in mono-modal conditions, its distance to the coaxial pin has to be larger than λ/4 because the fundamental mode is strongly perturbed around the coaxial pin.

The aperture of the horn and its length are optimized to improve both the axial ratio and the reflection coefficient of the structure. A big aperture improves the matching between waveguide and free space but also increases the feed directivity. In a multi-feed scenario, large apertures would also result in restrictions concerning the angular distances between feeds. Moreover, the lens needs to be illuminated by a moderately directive primary source, thus it is not convenient to design a large and highly directive horn aperture. Final dimensions are shown in Figure 1.2.3.3.4.

Finally, its performance is going to be shown in the following figures from 1.2.3.2.2 to 1.2.3.10. In the figures where AR is analyzed, the AR of the electric field is monitored for θ = 0° (broadside direction) and for θ = 15° within the frequency band of interest.

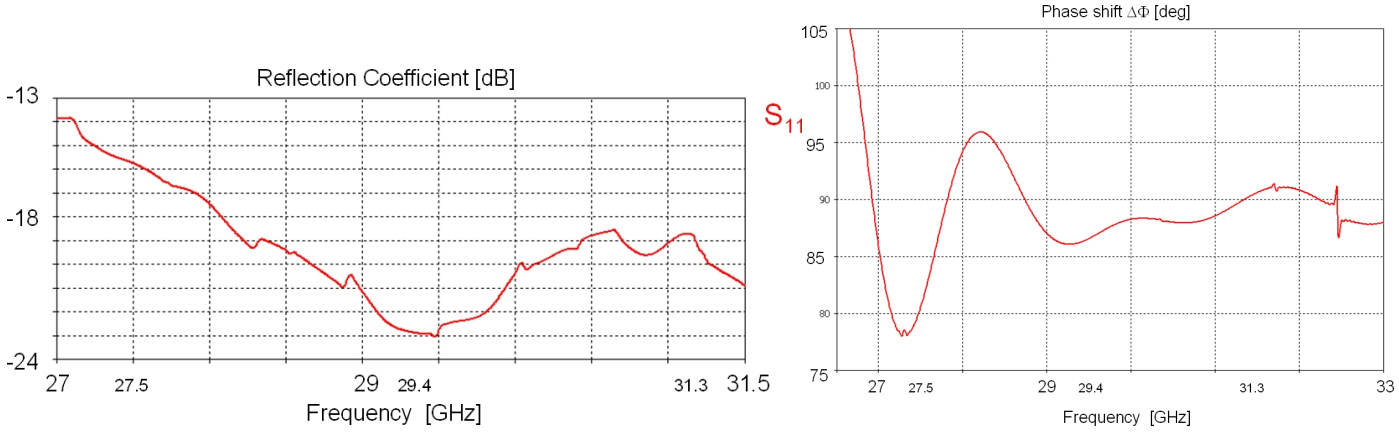

(a) (b)

Figure 1.2.3.3.5. *Dielectric septum polarizer (a) Reflection coefficient with lens, (b) phase difference*

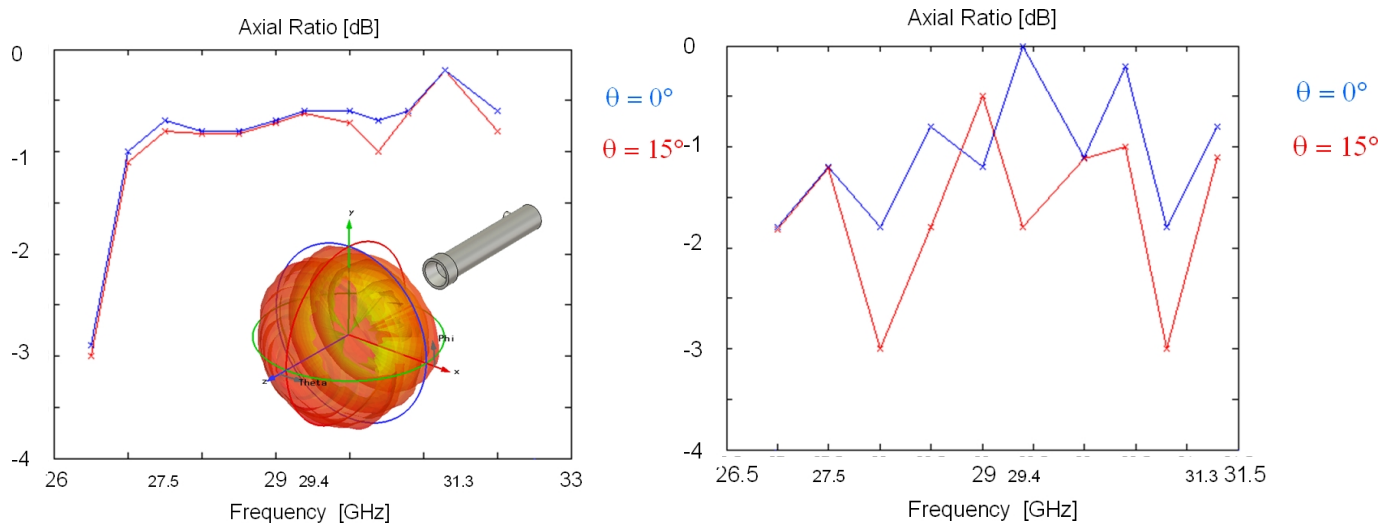

(a) (b)

Figure 1.2.3.3.6. *Dielectric septum polarizer axial ratio (a) without lens, (b) with lens*

Taking into account these results, it could be said that this polarizer is adequate in this scenario because it presents a small reflection coefficient, it presents a phase difference between polarization components around 90° and hence it presents a good axial ratio. But the axial ratio is degraded when the wave goes through the lens and this degradation is higher in the case where the observation point is shifted from the broadside direction with the cell.

Due to the degradation caused by the lens this polarizer is not suitable in this scenario because the radiating element is not directive enough without the lens, and thus the use of the lens is mandatory to achieve the radiation pattern depicted in Figure 1.1.2. Consequently, another different polarizer was studied based in the idea of performing the polarization change after the lens. This is the alternative exposed in next section.

1.2.3.4. Meander Line polarizer

The meander-line polarizer is the alternative that has been chosen to overcome the problems that will be explained in detail in section 1.3. Basically, the idea of using this polarizer came from the possibility to avoid the AR degradation as the wave passes through the lens by performing the polarization change after the lens.

Since this is the alternative that is going to be developed in the scope of this project, a deep theoretical analysis of this structure will be presented in this section, where a complete definition is exposed and also the state of the art in this kind of structures is going to be studied. With all this theoretical background a prototype of meander-line polarizer is going to be designed and optimized in section 3 for the scenario's conditions explained in section 1.1.

Definition

A meander-line polarizer (MLP) is defined as a passive broadband device used to convert the polarization properties of a wave. These polarizers are widely used due to their low insertion loss, broadband performance and ease to manufacturing.

The MLP was conceived at the Stanford Research Institute in 1966. It was based in the same electrical concept as the one explained by Lerner in [25] where he presented a polarization converter for CP in 1963. Lerner's polarizer uses a different physical configuration involving much narrower lines than the ones used in the MLP for the same bandwidth and center frequency. Since the tolerances of these line widths are critrica1, Young

decided to implement the MLP to achieve circular polarization and he published his studies and results in 1973, [26].

Typically, MLP are used to convert a wave from LP to CP and vice versa. When designed properly, the MLP permits a linear polarized antenna to generate a CP without any significant variations in the pattern performance. Nevertheless, nowadays the MLP´s scope has been broaden including applications such as: converting horizontal polarization to vertical polarization, [27]; crating arbitrary rotation of LP, [28]; and converting CW circular polarization to CCW circular polarization, [29].

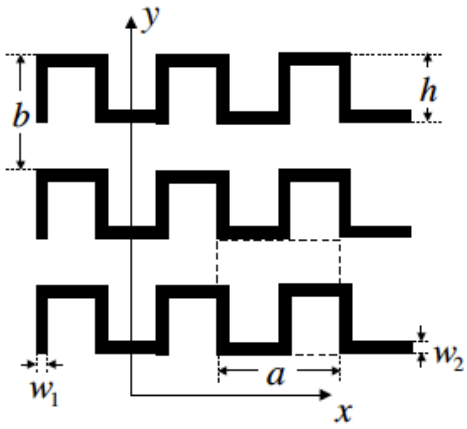

Figure 1.2.3.4.1. *Meander-line grid. [29]*

MLP makes use of a meander-line metallized planar structure as the one shown above in Figure 1.2.3.4.1. This structure is characterized by an impedance that is either inductive or capacitive depending upon the polarization of the E field according to Figure 1.2.3.4.2. If the electric field is parallel polarized to the grid, the grid appears as a shunt inductance producing a phase delay in the electric field. If the E field is orthogonal polarized to the grid, the grid will appear as a shunt capacitance and in this case the electric field's phase will be advanced.

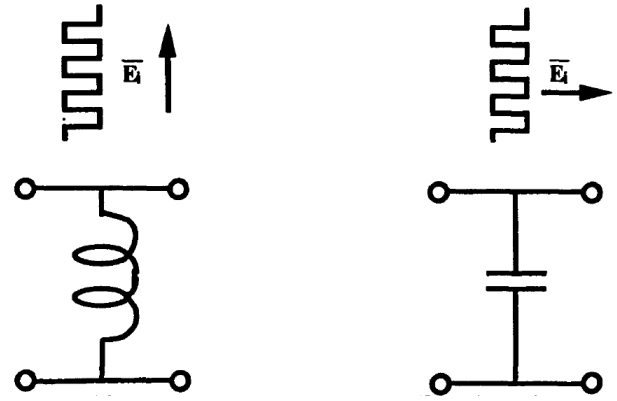

Figure 1.2.3.4.1. *Meander-line impedance as a function of polarization. [30]*

In a similar way as a certain polarization can be synthesized from two waves orthogonally polarized to each other, it is possible to define a linearly polarized electric field as its decomposition in two orthogonal in phase components. Therefore, it could be interesting to use as decomposition axes parallel and perpendicular directions with respect to the meander-line axis as indicated in Figure 1.2.3.4.3. Using equations 2.1 and 2.2, where ψ is the angle of the meander line axis with respect to the incident electric field, the decomposition of the electric field in two components parallel and perpendicular to the meander-line is straightforward.

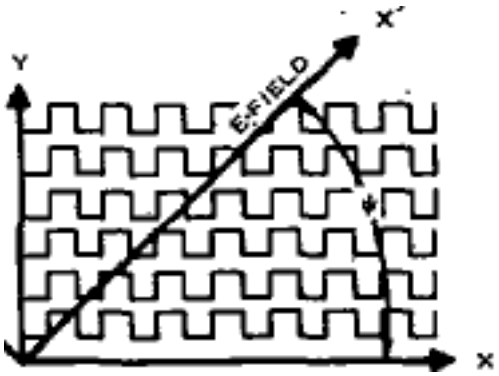

$$E_{\perp} = E_{inc} \cdot \sin\psi \qquad (1.2.3.4.1)$$

$$E_{\parallel} = E_{inc} \cdot \cos\psi \qquad (1.2.3.4.2)$$

Figure 1.2.3.4.3. *Decomposition of the incident field. [31]*

Consequently, when a linearly polarized electric field breaks through a meander-lines structure, its perpendicular and parallel components will be advanced and delayed respectively. This effect results in a transmission coefficient differential phase shift Δθ between the two orthogonal components of the incident electric field. By adjusting the values of Δθ and ψ, any input polarization may be converted to any output polarization.

The original functionality of the MLP was to use this phase difference (Δθ) to cause a linearly polarized wave, which is polarized at ψ = 45º to the grid, to become circularly polarized. The incident linearly polarized field has equal components parallel and orthogonal to the meander-line that are originally in phase with each other. The component of the field orthogonal to the meander-line is advanced 45º and the component of the field parallel to the meander-line is retarded 45º. Since these components are now equal in magnitude and 90º out of phase, a circularly polarized wave is emitted.

Several layers of meander-lines are often used to make the polarizer have better wideband characteristics. Hence, the general MLP physical model (graphically represented in Figure 1.2.3.4.3) is composed out of several layers etched on a thin dielectric and supported mechanically by foam or honeycomb in a sandwich configuration resulting in a relatively inexpensive design. Therefore, Δθ is determined by the dimensions of the meander lines, the thickness and relative permittivity of the dielectric layers, and the spacing between the sheets. And ψ can be fixed by a mechanical rotation of the polarizer or the antenna.

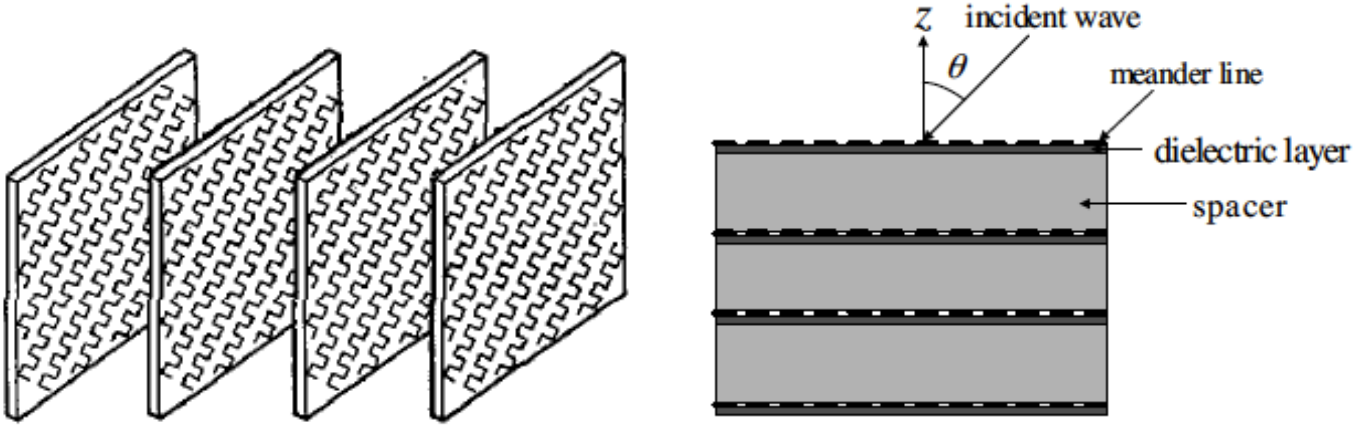

Figure 1.2.3.4.4. *Physical model of a MLP. [31] and [29]*

One of the preferred characteristics of this type of polarizer is its independence from the antenna properties. The polarizer may be thought of as an add-on to the antenna that does not affect its performance parameter. A properly designed polarizer will not significantly affect the beam-width of the antenna and, with correct placement, will not degrade the antenna SWR. Meander-line polarizers have been used with a wide variety of antenna types, from simple flat-panel polarizers to be placed over the aperture of horn antennas to more complex circular versions to be built around the circumference of bicone antennas.

Finally, some of the conclusions obtained by the pioneers in the study of the MLP are going to be reviewed to have a more in depth knowledge of this structure. These conclusions have been chosen because they present special relevance in the design and optimization process for MLPs.

Young presented in [26] a study of the MLP's stability over frequency, in this document it is stated that by spacing the elements about a quarter-wavelength apart this results in a small up-shift of the pass-band of the inductive filter, and a small down shift of the pass-band of the capacitive filter, as indicated in Figure 1.2.3.4.5(c). Hence the common or useful bandwidth is reduced, and goes from f_{L_1} to f_{C_2} as indicated in Figure 1.2.3.4.5(e). Since the overlap of the two pass-bands is considerable, the common bandwidth is still very adequate. The phase shift through each filter has almost the same slope (Figure 1.2.3.4.5(d)), so that if the differential phase shift is 90º at one frequency in the common pass-band, it remains close to 90º everywhere in the common pass-band, Figure 1.2.3.4.5(f).

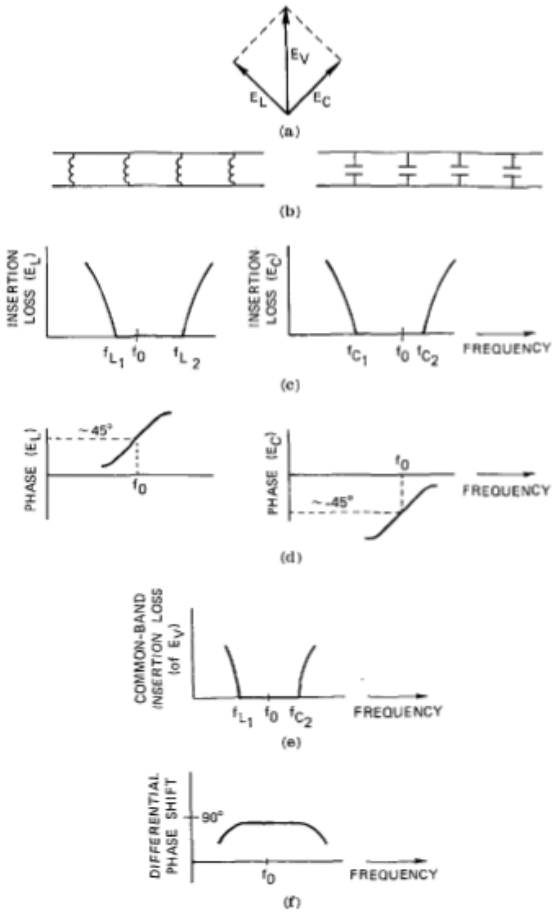

Figure 1.2.3.4.5. *Stability over frequency. [26]*

Moreover, Terrent performed in [32] an analysis of how each parameter defining the meander-line polarizer affects its performance. He concluded that spacing apart the meander lines (D_y) decreases the absolute value of the susceptances (Figure 1.2.3.4.5(a)) whereas variations in the periodicity of the meander line (D_x) and the permittivity of the dielectric (e_r) have slight influences (Figure 1.2.3.4.5(b) and (c)). D_y determines the value of the differential phase shift, the choice of which depends on the number of polarizer layers. The range of D_y is limited in order to avoid the propagation of higher order modes (grating lobes). The h, a_h, and a_v, parameters permit one to obtain, over the desired frequency range, a differential phase shift as flat as possible which is very important for polarizer design (Figure 1.2.3.4.5(d) and (e)).

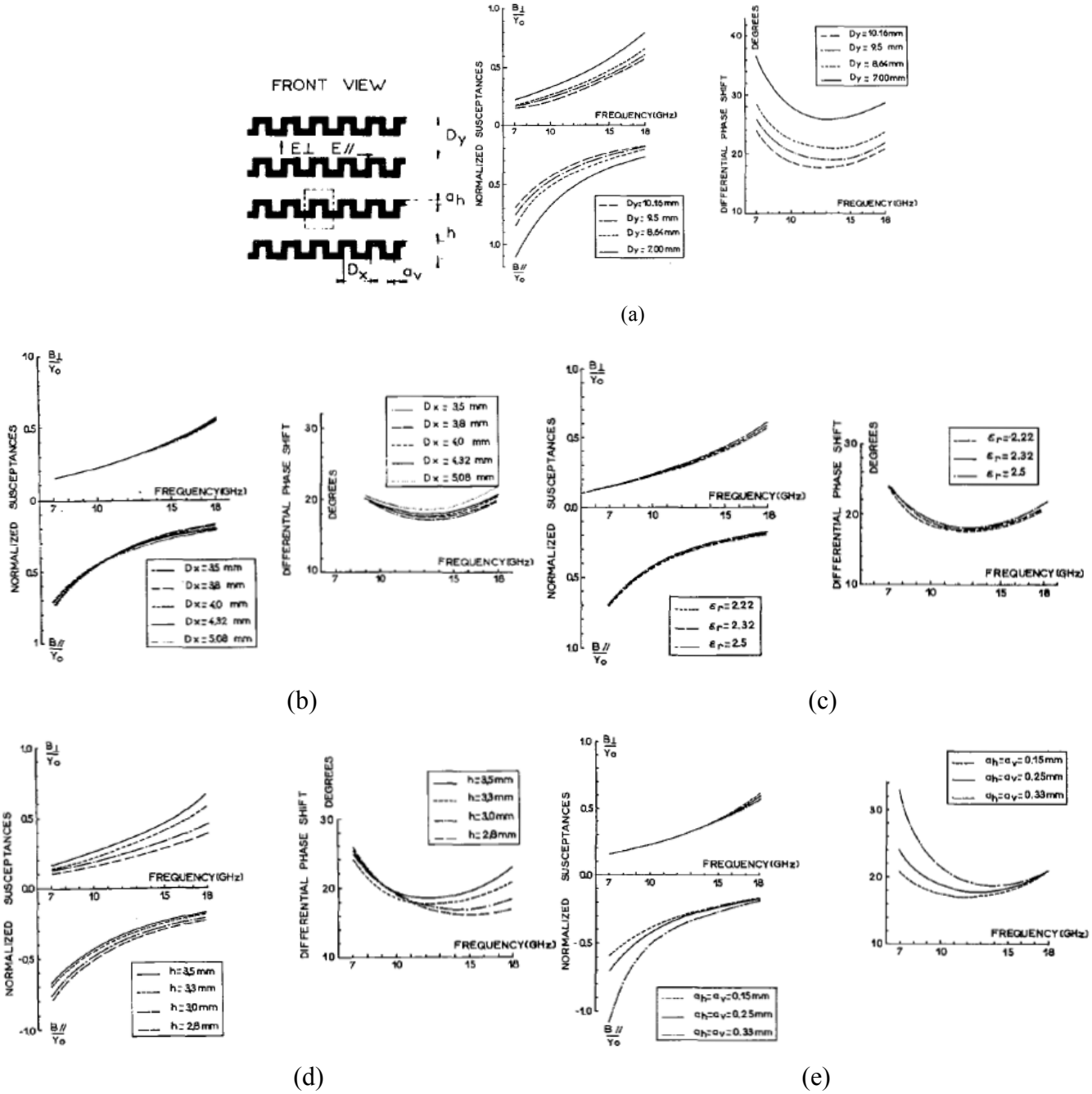

Figure 1.2.3.4.5. *Influence of meander-line geometry in the overall performance. [32]*

- **Young's Solution for Insertion Loss**

Young identified the loss mechanisms in meander-line designs, [26]. He identified and characterized as loss sources in the MLP: the meander-line loss, dielectric substrate loss and the loss of spacing between meander-line sheets. The loss term associated with the meander-lines is directly related to the Q of the inductive filter. The total loss of the meander-line design is

$$\Delta L_A \approx \frac{12.5}{wQ_{u,total}} dB \mid w \equiv filter\ bandwidth, Q_{u,total} \equiv unloded\ Q\ due\ to\ all\ loss\ sources \quad (1.2.3.4.3)$$

Where the unloaded Q due to all loss mechanisms is defined by

$$\frac{1}{Q_{u,total}} = \frac{1}{2}\left(\frac{1}{Q_{u,L}} + \frac{1}{Q_{u,C}}\right) + \frac{1}{Q_{u,spacer}} + \frac{1}{Q_{u,dielecric}} \quad (1.2.3.4.4)$$

Where the unloaded Q due to the inductive filter is defined by:

$$\frac{1}{Q_{u,L}} \approx \left(\frac{2500\delta}{\rho\lambda}\right)\left(\frac{w_1(h-w_2)}{h-w_2+{}^{a}/_{2}}\right)\log_{10}\left(\frac{a}{w_1}\right) \quad (1.2.3.4.5)$$

$$\delta \equiv metallization\ thickness$$

$$\rho \equiv metallization\ resistivity$$

$$\lambda \equiv free\ space\ wavelength$$

$$w_1, w_2, a, h \rightarrow are\ given\ by\ \text{Figure 1.2.3.4.1. Meander} - \text{line grid}$$

In these calculations, $Q_{u,C}$ is considered much larger than $Q_{u,L}$ and therefore can be ignored. Also the Q of the spacer and dielectric can be ignored if the thickness is less than 10 mils, which is true when the working frequency is high enough (in this study we are considering the Ka band, thus this condition is accomplished).

- **Terret's Solution for Scattering Using MoM**

Terret developed in [32] a moment method (MoM; an overview of this classical tool in electromagnetics will be presented in the following section) solution for meander-lines by subdividing a meander-line unit cell into 6 modules (as shown in Figure 1.2.3.4.6) to obtain the current density flowing over the meander-lines.

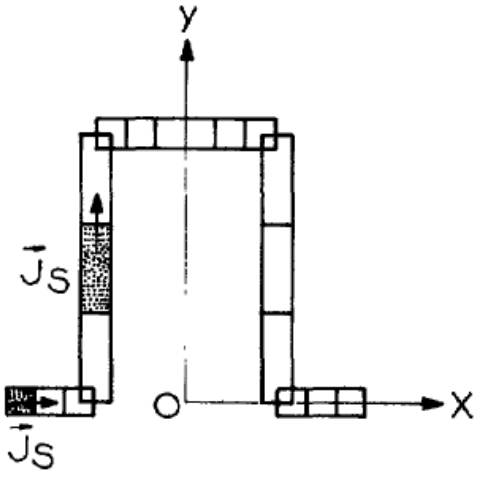

Figure 1.2.3.4.6. *Subdivision of the periodic cell. [32]*

In this method the electromagnetic field is developed into Floquet modes (this concept will be explained in the following section). The boundary conditions, combined with the orthogonality of the Floquet modes over a unit cell, lead to a Fredholm integral equation of the first kind for the unknown current density J_s. This integral equation can be solved by using the MoM and by expanding the unknown J_s in terms of a set of basis functions $\{f_n\}$ and testing on the same basis.

Upon finding the current density we can obtain the transfer matrix T of the array corresponding to transverse electric (TE) and transverse magnetic (TM) incident waves, i.e. the parallel and perpendicular decomposition components of the incident wave.

- **Chu and Lee's Analytical Solution**

Chu and Lee offered in [31] an analytical model to compute the impedances of meander-line sheet for both orthogonal and parallel solutions. The admittance seen by the perpendicular polarization E-field is consisting of three parts. The first part is due to the horizontal line segments parallel to the meander-line axis. The second part is due to the vertical line segment that is perpendicular to the meander-line axis. And the third part is due to the addition contribution due to the combination of the horizontal segments and the vertical segments which forms a periodic structure of approximate rectangular opening. For meander-line dimensions as shown in Figure 1.2.3.4.1, the admittance expression for perpendicular polarization is defined by:

$$Y_\perp = jB_\perp = j(B_C + B_L + B_\blacksquare) \tag{1.2.3.4.6}$$

where

$$B_C = K_2 \frac{4b}{\lambda}\left[-\ln\sin\left(\frac{\pi(b-w_2)}{2b}\right)\right]/\eta_0 \tag{1.2.3.4.7}$$

$$\eta_0 \equiv characteristic\ impedance\ of\ free\ space, \eta_0 = \sqrt{\frac{\mu_0}{\varepsilon_0}} = 377\Omega$$

$$\lambda \equiv free\ space\ wavelength$$

$$B_L = K_3\left[\frac{\eta_0 h}{\lambda}\ln\left(\sin\left(\frac{\pi w_1}{a}\right)\right)\right]^{-1} \tag{1.2.3.4.8}$$

$$B_\blacksquare = \frac{1}{\beta-\frac{1}{\beta}}K_1\frac{-\ln\left(\sin\left[\frac{\pi}{4}\left(\frac{a-2w_1}{8a}+\frac{b-h}{2b}\right)\right]\right)}{\frac{1}{2}\left(\frac{b}{h}+\frac{a}{\frac{a}{2}+w_1}\right)+\frac{1}{4}\left[\left(\frac{b}{\lambda}\right)^2+\left(\frac{a}{\lambda}\right)^2\right]} \tag{1.2.3.4.9}$$

$$\beta = \left[1-0.205\left(\frac{a-2w_1}{8a}+\frac{b-h}{2b}\right)\right]\Big/\left[\frac{1}{2}(a+b)/\lambda\right] \tag{1.2.3.4.10}$$

The impedance seen by the parallel polarization E-field consists of two parts. The first part is due to the horizontal line segment parallel to the meander-line axis. The second part is due to the vertical line segment that is perpendicular to the meander-line axis. For meander-line dimensions as shown in Figure 1.2.3.4.1, the impedance expresion for parallel polarization is defined by: (1.2.3.4.11)

$$Z_\parallel = jX_\parallel = j(X_1+X_2) = \frac{j\eta_0 a}{2\lambda\left[1-\left(\frac{fh}{5.62}\right)^2\right]}\left\{K_4\left[-\frac{b}{a}\ln\left(\frac{\pi w_2}{2b}\right)\right]+K_5\left[\frac{2h}{a}\ln\left(\frac{4a}{\pi w_1}\right)-0.492\right]\right\}$$

$$f \equiv frequency\ [GHz]$$

The empirical constants K_1, K_2, K_3, K_4 and K_5 for the meander-line circuit are to be determined by measuring the insertion phases due to each individual panel of the inner and outer panels

In Chu's solution, the effective sheet impedance of the meander-lines can be incorporated into a transmission line analogy for both orthogonal and parallel solutions, as shown in Figure 1.2.3.4.7 below. This transmission line model is composed of several sections (as many as MLP layers) connected in cascade configuration. Each section models the meander-line sheet as its corresponding admittance computed using the formulas aforementioned and the dielectric and spacer as their transmission line equivalents. Using this model it is possible to compute the transmission coefficients for both orthogonal and parallel decompositions.

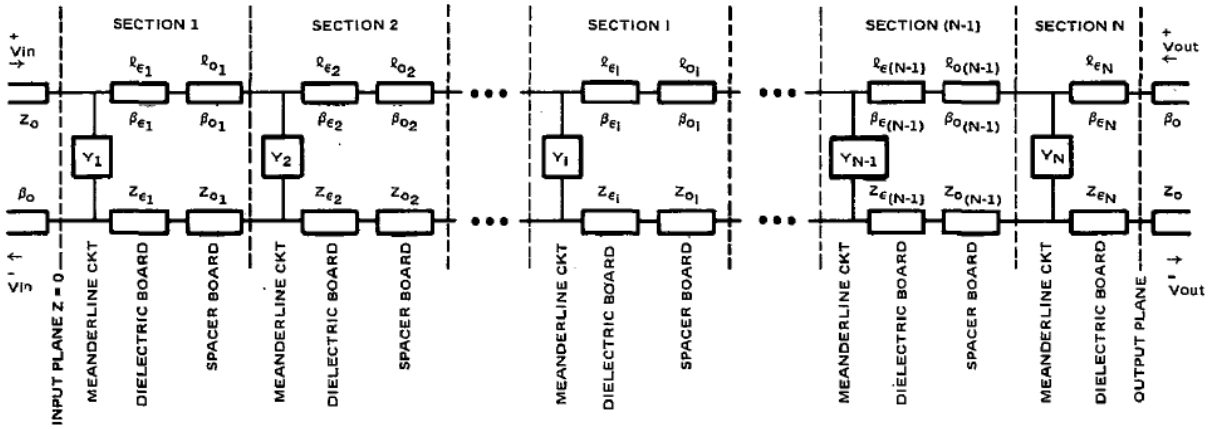

Figure 1.2.3.4.7. Transmission line model of a MLP

- **Numerical solutions for MLP susceptances**

This section details the numerical solutions traditionally used to mathematically predict the susceptance of a meander-lines sheet. Although they have been selected due to their usefulness to solve this particular problem, these mathematical tools are wide spread not only in the resolution of electromagnetic problems but also in much more general scenarios.

- **Method of Moments (MoM)**

MoM is one of the most widely used numerical methods in electromagnetics and it is also used in some others engineering communities (electrical, mechanical and civil engineering). MOM is a numerical technique that converts the integral equations, which are used to solve radiation and scattering problems, into a linear system that can be solved numerically using a computer. It was introduced in electromagnetics in 1993 by Harrington [33].

The basic approach in the MoM is to expand the unknown quantity (whose determination is the goal of this computation) using a set of known functions with unknown coefficients. The resulting equation is converted into a linear system of equations by enforcing the boundary conditions (for example the electric potential) at a number of points on the object. And the resulting linear system is finally solved numerically for the unknown coefficients.

In order to formalize this process, the problem can be generalized as it is described in [34]:

$$L(f) = g \tag{1.2.3.4.12}$$

where L is a linear operator, g is a known forcing function, and f is unknown. In electromagnetic problems, L is typically an integro-differential operator, f is the unknown function (charge, current) and g is a known excitation source (incident field). f is expanded into a sum of weighted basis functions that are chosen to model the expected behavior of the unknown function throughout its domain, and can be scalars or vectors depending on the problem:

$$f = \sum_{n=1}^{N} a_n f_n \tag{1.2.3.4.13}$$

$$\xrightarrow[(3.4.1.1)]{} \sum_{n=1}^{N} a_n L(f_n) \approx g \tag{1.2.3.4.14}$$

Therefore, the goal is to minimize the residual given by:

$$R = g - \sum_{n=1}^{N} a_n L(f_n) \tag{1.2.3.4.15}$$

Generalizing the method by which the boundary conditions are enforced, an inner product or *moment* between a basis function $f_n(r')$ and a testing or weighting function $f_n(r)$ can be defined as:

$$< f_n, f_m >= \int_{f_m} f_m(r) \int_{f_n} f_n(r')dr'dr \tag{1.2.3.4.16}$$

$$\xrightarrow[\substack{(3.4.1.4)\\ R=0}]{} \sum_{n=1}^{N} a_n < f_n, L(f_n) > = < f_n, g > \tag{1.2.3.4.17}$$

which results in the NxN matrix equation

$$Za = b \quad / \quad z_{mn} = < f_n, L(f_n) >, \qquad b_m = < f_n, g > \tag{1.2.3.4.18}$$

- **Floquet theory**

In the study of MLPs it is very important to take into account the fact that a meander-lines sheet can be considered periodic in the parallel and perpendicular directions with respect to the meander-lines axes.

On this premise, the studies published by Floquet in [35] are of special interest. In this document Floquet presents a theorem useful for solving linear differential equations with periodic coefficients. And the aforementioned periodicity of a meander-lines sheet yields to periodic coefficients in the equations system that is used to solve radiation and scattering problems.

The Floquet theory gives a canonical form for each fundamental matrix solution of this linear system. It gives a coordinate change that transforms the periodic system to a traditional linear system with constant, real coefficients.

This theory is used by commercial software to solve electromagnetic problems, such as CST Microwave Studio or Ansoft HFSS. These tools provide a special feature for doubly periodic boundaries where a unit cell must be defined with periodic boundary conditions and floquet's ports. The Floquet port is closely related to a Wave port in the sense that a set of modes is used to represent the fields on the port boundary. The new modes are the so-called Floquet modes that appear in section concerning Terret's Solution for Scattering Using MoM. Basically, Floquet modes are plane waves with propagation direction set by the frequency, phasing, and geometry of the periodic structure. An example of the use of Floquet ports in HFSS is shown in Figure 1.2.3.4.8 below.

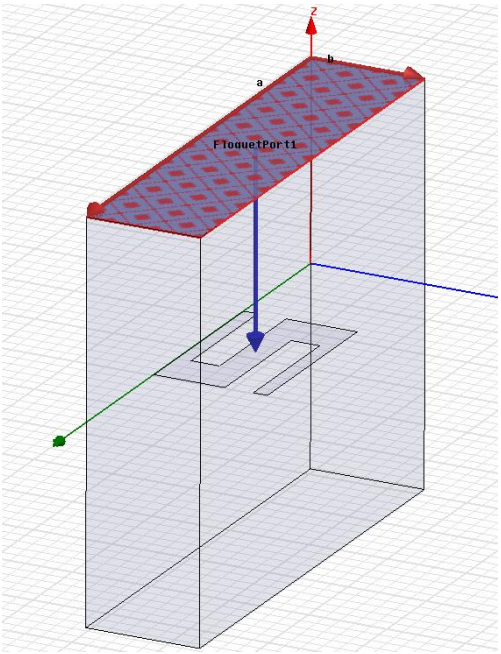

Figure 1.2.3.4.8. HFSS floquet port

- **Periodic moment method, PMM**

PMM is a derivation of the moment method for doubly-infinite arrays using Floquet's theorem. It was developed by Munk and colleagues at Ohio State University to solve the numerical analysis of antenna arrays, frequency selective surfaces and gratings.

Following this studies Henderson developed a PMM code [36] to compute the transmission and reflection coefficients of doubly infinite structures. This code analyzes *multiple infinitely periodic, planar arrays of arbitrary shaped scatterers embedded in a lossy stratified dielectric medium*. A periodic array of identical elements models the scatters by means of a reference element, the unit cell.

This code has been widely used in the design of periodic planar structures such as MLP and its PMM theory is implemented as a special solver in commercial software, such as CST or HFSS, to solve problems with periodic boundary conditions.

1.2.4. **Complete system**

Sections 1.2.1, 1.2.2 and 1.2.3 have presented the study of the different strategies and technologies that could be used to fulfill the requirements. Based in this study, it has been decided to design, optimize, prototype and test a complete system composed out of three components:

- Circular waveguide feeds terminated with a horn.
- Dielectric homogeneous spherical lens.
- External MLP after the lens.

Figure 1.2.4.1 below shows a graphical representation of the complete system that has been used in simulations for the simplified case of only one beam.

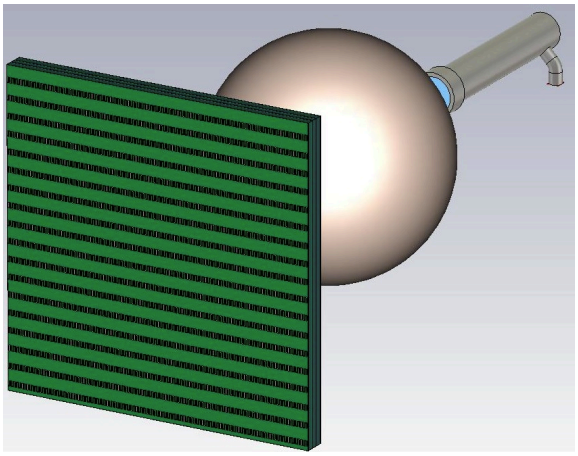

Figure 1.2.4.1. *Complete system with only one feed*

The design and optimization of the MLP is one of the main topics of this project, thus the results concerning the MLP (basically the AR results) will be studied in detail in section 3. On the other hand, it could be interesting to demonstrate before going further that using this technology of feed plus lens requirements are met. Therefore, in Figure 1.2.4.2 results on the antenna system's radiation pattern are shown and Table 1.2.4.1 summarizes the performance characteristics of this system composed out of the fed plus the lens. In addition, the reflection coefficient has been analyzed in Figure 1.2.4.3, where it can be seen that it is lower than -15 dB within the frequency band of interest and the antenna bandwidth is more than 13%.

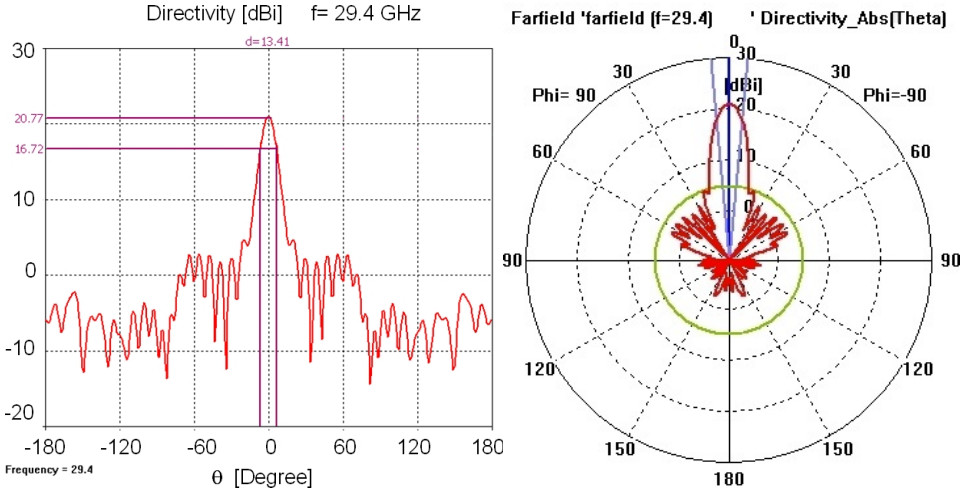

Figure 1.2.4.2. *Radiation pattern of feed plus lens*

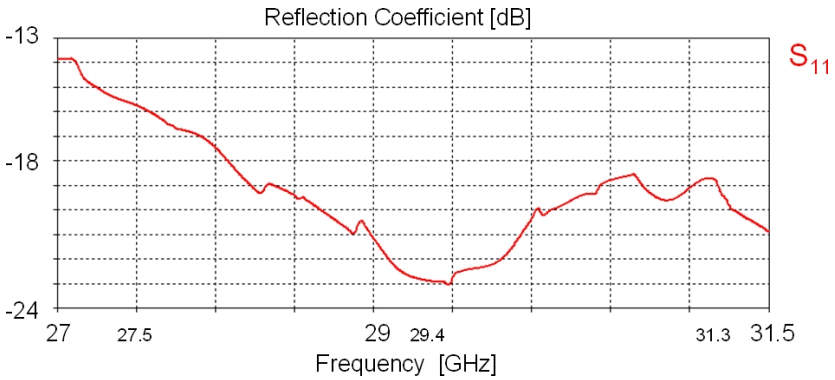

Figure 1.2.4.3. Reflection coefficient of feed plus lens

Working Frequency Band	26.8-32.5 GHz
Bandwidth	5.7 GHz (≈19%)
Directivity	21 dBi
Beamwidth at -4 dB (FoV)	13.4°
Side Lobe Level (SLL)	< -18 dB

Table 1.2.4.1. *Performance characteristics of feed plus lens*

As it can be checked, all the scenario initial specifications given in Table 1.1.1 are achieved. The antenna covers all the expected frequencies and shows indeed a frequency bandwidth broader than required (19% instead of 13%). The directivity of 21 dBi let a 2 dB difference to meet the gain requirement of 19dB. It means that the ohmic and dielectric losses of the real antenna must be lower than 2 dB. In addition, the sidelobe is within the specifications.

On the other hand, as it was exposed in section 1.1, for the complete scenario it is necessary to analyze the case of multibeam system in order to provide cellular communications according to the geometrical considerations fixed by the specifications. Therefore, in order to produce 7 cells on the ground, as shown in Figure 1.1.1, 7 independent beams have to be radiated by the lens. By placing 7 feeds at the same distance from the lens surface, 7 identical beams are generated. Each feed radiates broadside and illuminates the lens properly. The lens focuses the radiation coming from every feed and shapes it into a directive beam. Each feed has to be positioned around the lens in such a way that each beam points to the corresponding cell center on the ground and all the feeds' longitudinal axes intersect at the lens center. From geometrical considerations the distance between adjacent cell centers is given by:

$$d = 2R_{cell} \cos 30° = 4.33 \text{ Km} \tag{1.2.4.1}$$

This distance determines in turn the angular position of the feeds around the lens guaranteeing adequate coverage of the ground. The angle between adjacent feeds must be:

$$\theta_s = \arctan\left(\frac{4.33 \cdot 10^3}{H_{HAPS}}\right) = 12° \tag{1.2.4.2}$$

Therefore, the resulting antenna system including the lens plus 7 feeds must be set up in the configuration showed in Figure 1.2.4.4 below. This model is the one that has been used to analyze the interaction between feeds in the complete scenario by means of EM simulations using CST.

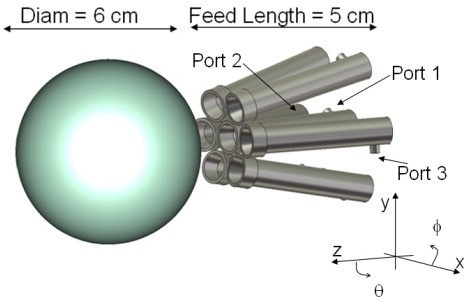

Figure 1.2.4.4. *Multibeam antenna model.*

In order to analyze the influence of adjacent feeds, the radiation pattern produced by this antenna system model has been simulated and results can be seen in Figure 1.2.4.5, where two relevant cutting planes has been selected ($\phi = 0°$ and $\phi = 60°$) taking into account the antenna system geometry. As it can be checked each single beam radiation pattern of the multi-beam antenna does not change significantly compared to the radiation pattern of a single feed antenna (Figure 1.2.4.2).

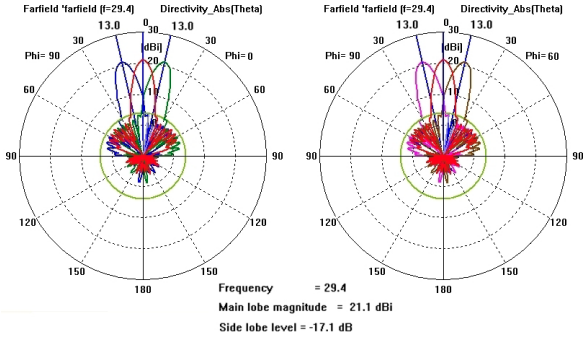

Figure 1.2.4.5. *Complete system radiation pattern in planes* $\phi = 0°$ *and* $\phi = 60°$

Others interesting characteristics to analyze the influence of adjacent feeds are the scattering parameters. Due to symmetrical reasons, and taking into account future limitations on prototyping to compare results, only three scattering parameters have been analyzed: S_{11}, S_{21} and S_{23}; according to the notation of Port 1, 2 and 3 as defined in Figure 1.2.4.3. The active reflection coefficient of the central feed in the presence of the other six, i.e. S_{11} in Figure 1.2.4.6, is quite similar to the one of the single feed antenna shown in Figure 1.2.4.3. This anticipates a weak coupling between feeds and promises quite identical results for all the S_{ii}in the multi-feed simulation. Indeed the coupling between adjacent feeds is lower than -32 dB within the working frequency band as it can be checked in Figure 1.2.4.6 below.

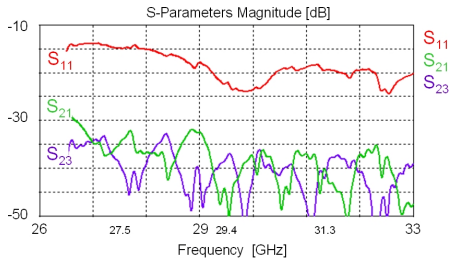

Figure 1.2.4.6. *Scattering parameters of 7 feed plus lens model*

Therefore, in this section has been demonstrated the independence between ports, as well as the agreement with the scenario specifications, in the case of a multibeam antenna system using the waveguide feed plus lens technology. Since the performances of one waveguide feed are not influenced by the presence of the others, the multi-beam antenna can be easily designed, focusing the attention on only one feed.

1.3. Related problems

In previous sections different strategies and technologies have been studied in the scenario of HAPS cellular communication system, analyzing their benefits and drawbacks. Finally, a concrete technology (i.e. waveguide feed + lens) has been chosen due to its benefits over the other analyzed alternatives. Nevertheless, this technology presents several problems that must be studied in order to propose alternatives or solutions to overcome them. This section summarizes the different problems that have been identified and whose solution is the main task in the scope of this project.

1.3.1. Beam footprint of external cells

So far the design of the antenna system has taken into account that the desired radiation pattern is the one presented in the scenario (section 1.1) and depicted in Figure 1.1.2. This radiation pattern produces a projection on the ground (footprint) with circular shape and with the power distribution considerations given by the specifications. But this assumption is completely true only in the case of orthogonal incidence of the beam main axis with respect to the ground plane, i.e. only for the central feed of the model considered in Figure 1.2.4.4.

Nevertheless, in the case of oblique incidence the scenario is different and its footprint corresponds to the cut of a cone with an oblique plane which, as Apollonius of Perga (ancient Greek geometer and astronomer famous for his writings o conic sections) demonstrated, results in an ellipse as can be seen in Figure 1.3.1.1 where a cone is cut by a parallel plane (orthogonal incidence on the ground) and by a oblique plane (orthogonal incidence on the ground).

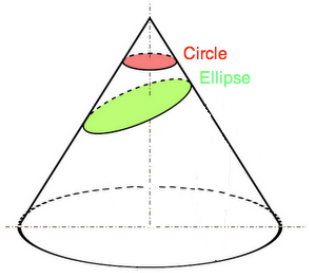

Figure 1.3.1.1. *Possible footprints for orthogonal and oblique incidence*

This deformation of the footprint with respect to the circular shape produced by orthogonal incidence increases with the incidence angle, producing a bigger ellipticity effect as cells are projected further from the central one as can be seen in Figure 1.3.1.2. In the scenario under study in this project, where only seven cells are considered, all the external cells presents the same incidence angle (12°) and thus the ellipticity effect is the same for all of them. Therefore, the external cells of the cluster are slightly deformed and exhibit an elliptical shape with axes lengths equal to 5.24 and 5 Km, which means an ellipticity of 5%. However, if the scenario is extended in future applications in order to provide bigger clusters (i.e. containing more cells) by including additional feeds around the seven that are considered here, the new outer cells will suffer a bigger ellipticity effect. Consequently, this effect should be compensated, and this is only possible by changing the radiation pattern associated to the external cells in order to provide a circular shape footprint. Section 3 presents a characterization of this problem, propose several possible solutions to compensate the effect and they are analyzed by means of EM simulations and measurements.

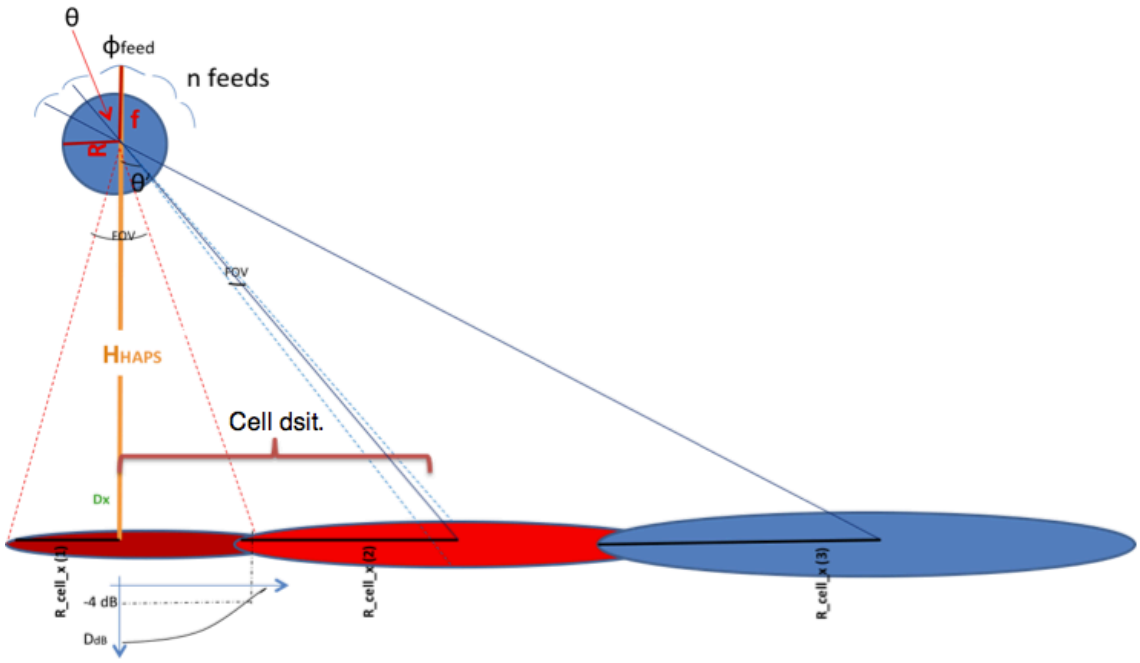

Figure 1.3.1.2. *Ellipticity effect on outer cells of the cluster*

1.3.2. Axial ratio degradation

In section 1.1 where the scenario specifications were set, it was introduced the need of circular polarization for many wireless communications services such as GPS and TV broadcasting. In order to measure the quality of the produced circular polarization, according to the definition of polarization presented in section 1.2.3.1, it is necessary to compute the relation of the two orthogonal instantaneous components of the electric field in phase and magnitude. Taking into account equation 1.2.3.1.5, they must be equal in magnitude and their phase difference equal to 90° in order to produce perfect circular polarization. When these conditions are not met, the resulting geometric figure described by the end of the electric field vector is an ellipse. The parameter used to measure the quality of the circular polarization is the ratio between the two axes of the ellipse, i.e. the axial ratio. According to equation 1.2.3.1.6 the AR is equal to 0 dB in the case of perfect circular polarization and it increases when the difference between axes increase.

The first approach to produce circular polarization (once it was decided to adopt strategy 1.2.3.1 to design the radiator) was to design a feed that, including an internal septum polarizer, produces a circular polarized wave which would be focused by a lens to achieve the desired radiation pattern. However, as it was demonstrated in sections 1.2.3.2 and 1.2.3.3, where two different internal polarized were analyzed, the circular polarization provided by the feed is degraded as the wave passes through the lens (see Figure 1.3.2.1) and thus the axial ratio increases as it can be seen in Figures 1.2.3.2.4, 1.2.3.2.7, 1.2.3.2.10 and 1.2.3.3.6. Furthermore, as it can be seen in these figures, although degradation of the axial ratio is not very important in the broadside direction, i.e. in the center of the cell, it increases as the observation point is moved apart from the cell center.

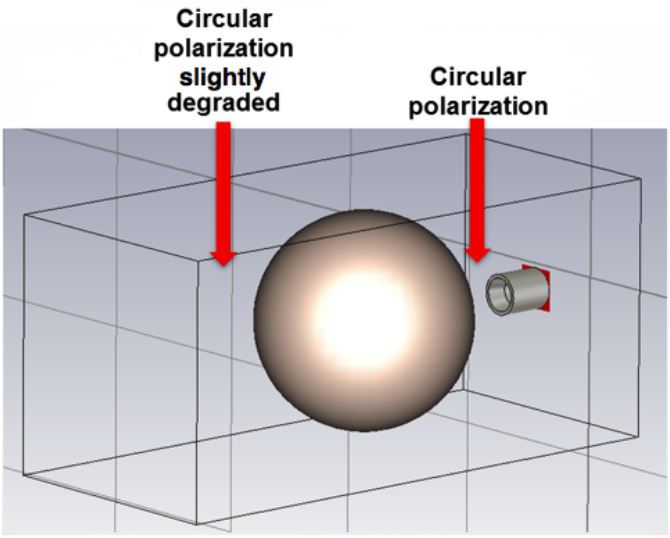

Figure 1.3.2.1. Polarization scheme in the case of internal polarizer

In order to overcome this problem it has been introduced in section 1.2.3.4 an alternative polarizer (MLP) that, due to its low insertion loss and broadband performance (apart from it ease to manufacture), has been selected to be placed after the lens to produce the polarization conversion on all the beams at the same time after been focused be the lens in order to avoid the polarization degradation that it introduces (see Figure 1.3.2.1). Nevertheless, using this structure could imply some limitations in the positions of the external feeds and some of its characteristics lead to problems in the full wave analysis of the structure (CST simulations). In section 3 all these intrinsic problems to the MLP will be analyzed and it will be demonstrated that with an adequate optimization procedure it is possible overcome these issues and thus providing a solution that works not only in the scenario of this project but also in future scenarios were bigger clusters with more cells are required.

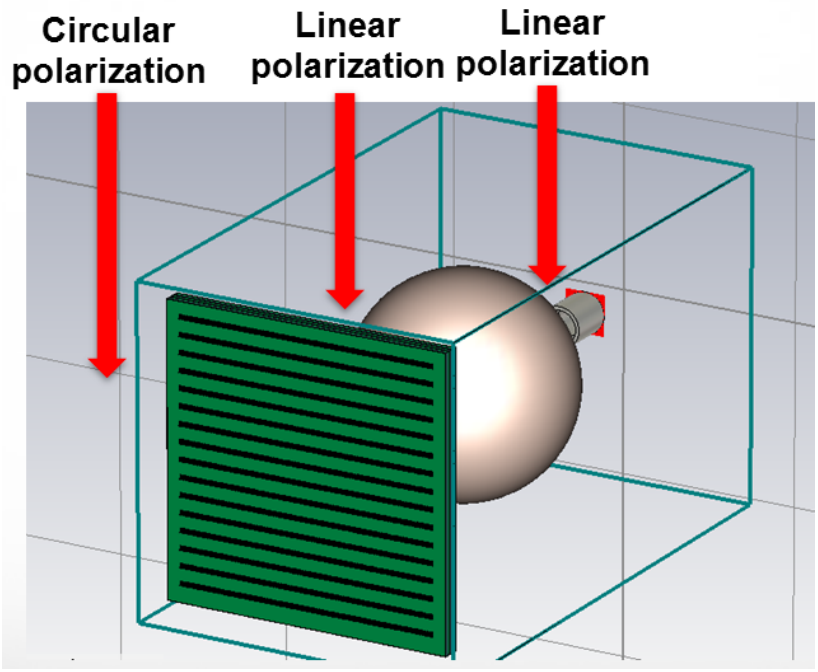

Figure 1.3.2.2. Polarization scheme in the case of external polarizer after de lens

1.3.3. **Feeds coupling**

In section 1.2.4, where the influence of adjacent feeds was analyzed for the model that includes seven feeds plus lens, it was shown in Figure 1.2.4.5 how the coupling between adjacent feeds is lower than -32 dB within the working frequency band. Nevertheless, in a mobile communications scenario were a feed tries to receive a very weak signal coming from the ground while a small part of the energy ($s_{21} \leq -32dB$) coming from adjacent feeds is also received, the weak signal could remain embedded in the signal coming from adjacent feeds and thus not being possible to process the ground signal.

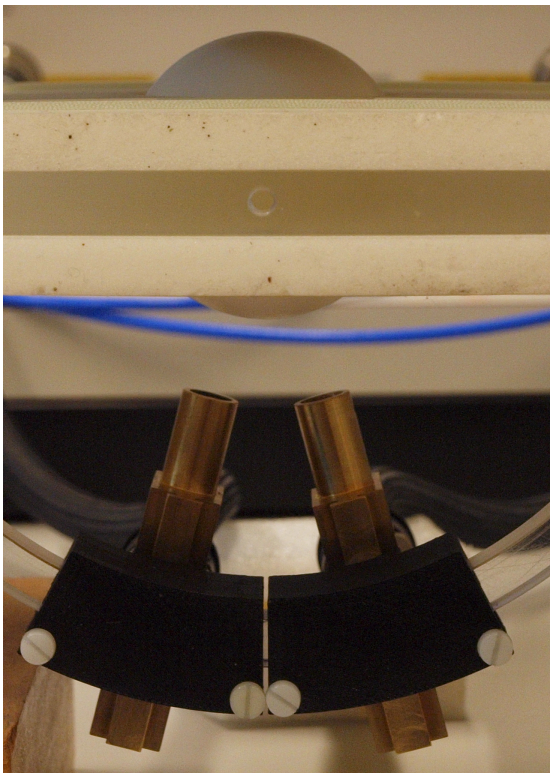

Figure 1.3.3.1 *Analysis of feed's coupling*

Therefore, although initially out of the scope of this project, several ideas have been proposed and tested to reduce the coupling between adjacent feeds even more. Section 4 contains the analysis of the different techniques proposed as well as the conclusions that have been extracted. Furthermore, based on these conclusions new techniques to reduce the coupling are proposed.

2. Correction of beam footprint.

In previous section 1.3 it has been explained how the beam footprint of the external cells suffers a deformation from the ideal circular shape to an elliptical shape and thus being no more possible to obtain the correct geometrical cell distribution on the ground to conform an hexagon which maximizes coverage in a multi-HAPS scenario.

This section exposes the work carried out to analyze and to overcome the ellipticity problem. In section 2.1 a software characterization of the problem has been performed by means of several Matlab scripts. Then Section 2.2 goes through the different alternatives studied to overcome the problem including simulations, measurements and the mechanical design of different devices needed to perform the measurements.

2.1. Software problem characterization

In order to characterize the problem several Matlab functions and scripts have been implemented. Section 2.1.1 presents the description of this software and section 2.1.2 shows the results of the application of this tool in the analysis of the problem, obtaining concrete conclusions in the changes that should be performed on the radiation pattern to correct the ellipticity effect.

2.1.1. Software description

Different Matlab functions and scripts have been developed in order to provide the project with a tool capable of computing the power distribution on the ground given by a certain radiation pattern (which comes from a text file exported from CST simulations) and taking into account the concrete scenario characteristics.

On the other hand, although this first tool is very useful to characterize and analyze the problem, it could be really interesting to face the opposite problem in order to know how to modify the radiation pattern, and hence the antenna system, to achieve a circular shape of the beam footprint in different situations. Therefore, a second tool has been developed which, by means of different Matlab functions and scripts, given a concrete power distribution on the ground estimates the radiation pattern that should be used in that scenario to obtain the correct power distribution.

- **Computation of the power distribution on the ground**

The first step to compute the beam footprint is to process the radiation pattern text file given by CST simulations. Making use of the function ‘transform’ (see Annex 1) the number of points used to perform the operation can be selected and then it transforms the input data into a matrix containing the discrete values of the radiation pattern transformed into a confortable coordinates system as can be seen in Figure 2.1.1 below.

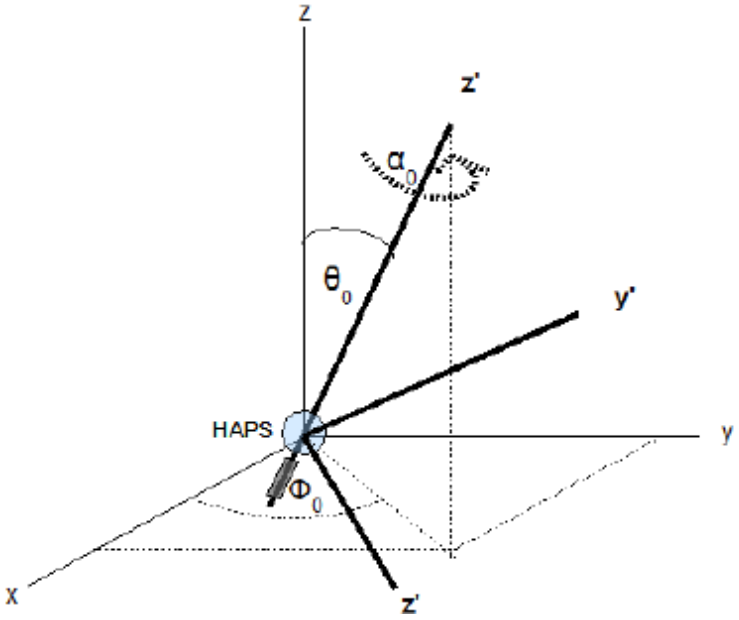

Figure 2.1.1.1. *Coordinates system change in the transformation of the radiation pattern*

This transformation can be summarized in tree steps:

1) Change form the original spherical coordinates system (θ', ϕ') to the Cartesian coordinates system (x',y',z').

2) Rotate the coordinates system in order to obtain (x,y,z). This operation is not so trivial and may be interesting to note how it is performed:

$$\begin{pmatrix} x \\ y \\ z \end{pmatrix} = T_{\propto} \cdot T_{\theta} \cdot T_{\phi} \cdot \begin{pmatrix} x' \\ y' \\ z' \end{pmatrix} = T_T \cdot \begin{pmatrix} x' \\ y' \\ z' \end{pmatrix} \quad (2.1.1.1)$$

where:

$$T_{\propto} = \begin{bmatrix} \cos \propto & \sin \propto & 0 \\ -\sin \propto & \cos \propto & 0 \\ 0 & 0 & 1 \end{bmatrix} \quad (2.1.1.2)$$

$$T_{\theta} = \begin{bmatrix} \cos\theta & 0 & -\sin\theta \\ 0 & 1 & 0 \\ \sin\theta & 0 & \cos\theta \end{bmatrix} \quad (2.1.1.3)$$

$$T_{\phi} = \begin{bmatrix} \cos\phi & \sin\phi & 0 \\ -\sin\phi & \cos\phi & 0 \\ 0 & 0 & 1 \end{bmatrix} \quad (2.1.1.4)$$

3) Change form the Cartesian coordinates system (x,y,z) to the spherical coordinates system (θ, ϕ).

Once the radiation pattern has been processed to obtain discrete power values located on a confortable coordinates system, the computation of the power footprint is performed by means of the function 'footprint' (see Annex 1). In order to carry out this computation the Friis formula [14] has been used in the following way:

$$P_R = P_T \cdot G_T(\theta, \phi) \cdot \left(\frac{\lambda}{4\pi d}\right)^2 \cdot G_R \quad (2.1.1.5)$$

where:

P_R is the received power

P_T is the transmitted power that is set to 1

G_T is the transmitter gain, i.e. the transformed directivity D

G_R is the receiver gain that is set to 1

$d = {H_{HAPS}}/{cos\,(\theta_s)}$ According to the geometrical considerations of the scenario definition

Using equation (2.1.1.5) the power distribution on the ground is computed as the relation in dBs between power received and the maximum power received in such a way that the function 'footprint' produces a matrix which maps the power distribution:

$$10\log\left(\frac{P_R}{P_{R_{MAX}}}\right) = 10\log\left(P_T \cdot D(\theta,\phi)\cdot\left(\frac{\lambda}{4\pi}\right)^2\right) - 20\log\left({H_{HAPS}}/{cos\,(\theta_s)}\right) - 10\log\left(P_{R_{MAX}}\right) \quad (2.1.1.6)$$

- **Computation of the corrected radiation pattern**

In order to know how the radiation pattern, and hence the antenna system, should be modified to produce a circular beam footprint in the case of oblique incidence the function 'footprint_inv' has been developed. This function receives as input the matrix which maps the power distribution (in the same format as the result computed by 'footprint') and making use of equation 2.1.1.6 computes the required directivity in the spherical coordinates system (θ, ϕ) as follows:

$$10\log\left(D(\theta,\phi)\right) = 10\log(P_R) + 20\log\left({H_{HAPS}}/{cos\,(\theta_s)}\right) - 10\log\left(P_T\left(\frac{\lambda}{4\pi}\right)^2\right) \quad (2.1.1.7)$$

Once the corrected radiation pattern has been obtained, it is possible to invert the transformation performed in section 2.1.1 to present the result in the original spherical coordinates system (θ', ϕ') and produce with it a text file in the same format as the one used as input for 'footprint' function. Therefore, it is possible to check the validity of the corrected radiation pattern to compensate the ellipticity effect. Making use of equations 2.1.1.1, 2.1.1.2, 2.1.1.3 and 2.1.1.4, the coordinates system change needs to compute the inversion of the transformation matrix:

$$\begin{pmatrix} x' \\ y' \\ z' \end{pmatrix} = {T_T}^{-1} \cdot \begin{pmatrix} x \\ y \\ z \end{pmatrix} \quad (2.1.1.8)$$

2.1.2. Problem characterization

Using the geometrical characteristics of the scenario depicted in section 1.1 it has been computed the beam footprint produced by any of the six external feeds. Figure 2.1.2.1 shows the resulting power distribution on the ground and Table 2.1.2.1 contains the parameters that characterize the ellipticity of the external cells given by the -4 dB curve.

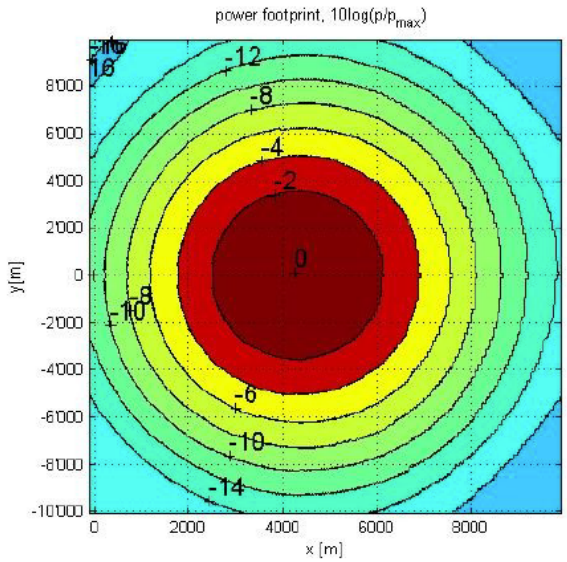

Figure 2.1.2.1. *Power distribution on the ground for external cells.*

Ellipse long axis	5200 m
Ellipse short axis	5044 m
Ellipticity	3.1%

Table 2.1.2.1. *Ellipticity of external cells.*

As it can be appreciated in these results, the external cells suffer a shape deformation according to what it was anticipated in section 1.3 producing a 3.1% ellipticity in the -4 dB curve, i.e. in the cell boundary. Although this effect is quite small in the case of an scenario with 7 cells, future applications may require architectures with bigger clusters making use of more cells and thus the new outer cells will present a much more elliptic boundary.

Therefore, in order to be able to clearly see the effects of the radiation pattern correction in the footprint, it has been studied the power distribution on the ground in the case of having a second and third ring of feeds (see figure 1.2.4.4). In this case the resulting footprint of the external cells, which lay around 14 Km away from the central cell, is shown in Figure 2.1.2.2 and Table 2.1.2.2 contains the parameters that characterize the ellipticity of the external cells' boundary.

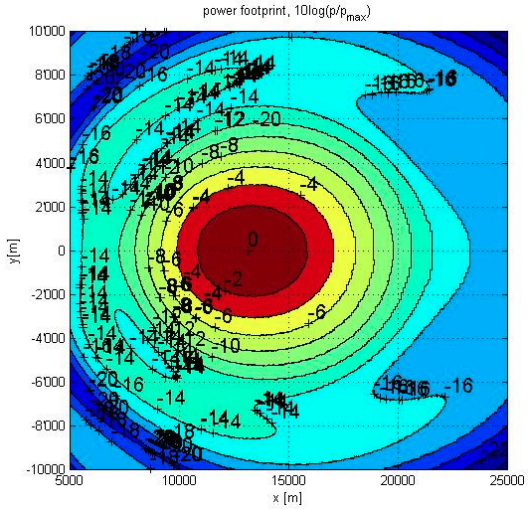

Figure 2.1.2.2. *Power distribution on the ground for external cells in the case of 3 rings of feeds.*

Ellipse long axis	7206 m
Ellipse short axis	6081 m
Ellipticity	18.5%

Table 2.1.2.2. *Ellipticity of external cells in the case of 3 rings of feeds.*

As it can be observed in these results, the effects on the shape deformation of the cell's boundary can be appreciated much more clearly than before producing a 18.5% ellipticity and thus the correction on the beam's radiation pattern will be more intense.

Using the power distribution on the ground depicted in Figure 2.1.2.2, it has been computed the corrected radiation pattern that should be produced by the external feeds of the third ring of feeds in order to compensate the ellipticity effect. The resulting radiation pattern is shown in Figure 2.1.2.3 and from its analysis it has been concluded that the directivity should be increased in the direction of the ellipse long axis ($\phi = 0°$) while maintaining the same directivity in the direction of the ellipse short axis ($\phi = 90°$) as it has been depicted in Figure 2.1.2.4.

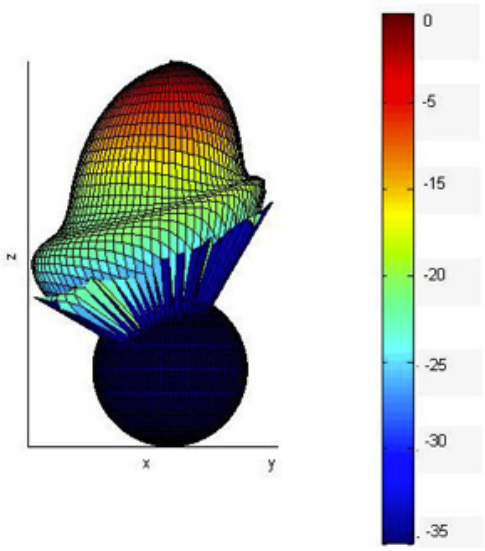

Figure 2.1.2.3. *Corrected radiation pattern.*

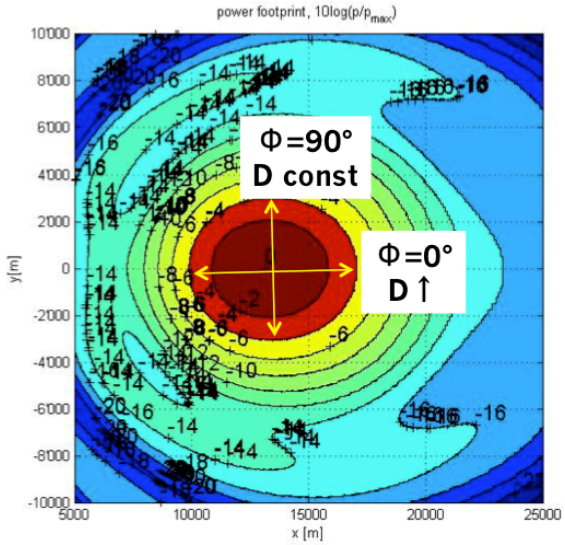

Figure 2.1.2.4. *Directivity corrections needed to compensate the ellipticity effect.*

Once the new radiation pattern has been computed it could be interesting to feedback with this result the script that compute the resulting power distribution on the ground. This way it would be possible to check the correctness on the conclusions that have been extracted about the directivity to correct the ellipticity effect. The resulting corrected footprint can be observed in Figure 2.1.2.5 and Table 2.1.2.3 contains the parameters that characterize its ellipticity in the cell boundary.

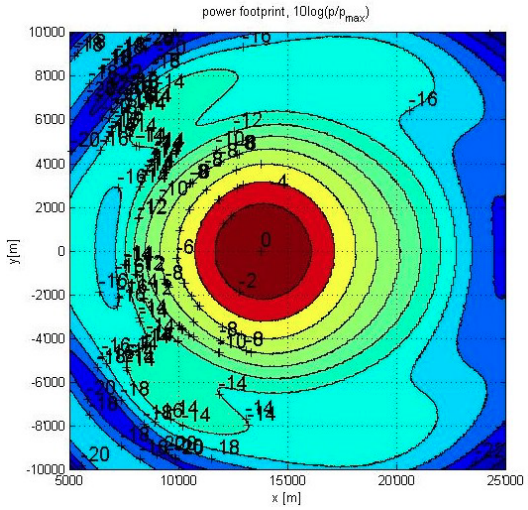

Figure 2.1.2.5. Corrected *power distribution on the ground for external cells in the case of 3 rings of feeds.*

Ellipse long axis	6476 m
Ellipse short axis	6400 m
Ellipticity	1.2%

Table 2.1.2.3. Corrected e*llipticity of external cells in the case of 3 rings of feeds.*

As it can be observed in these results and compared with the results exposed in Figure 2.1.2.2 and Table 2.1.2.2, the changes performed in the radiation pattern depicted in Figure 2.1.2.3 are able to correct the ellipticity of the cell's boundary from 18.5% to 1.2% and thus verifying the correctness of the conclusions on the needed directivity changes shown in Figure 2.1.2.4.

It can be perceived in Tables 2.1.2.2 and 2.1.2.3 that in the case of three rings of feeds the cell boundary not only suffers a deformation into an elliptical shape but also suffers an enlargement making the cell bigger. This is due to the fact that in this case the distance between the HAPS and the cell is bigger than before. In order to compensate this effect, and thus to have cells with the same dimension, the beam should be focused even more for this case. However this problem is out of the scope of this project because, as can be observed in Table 2.1.2.1, in the case of the scenario depicted in section 1.1 where only 7 cells are considered the distance between the HAPS and the external cells is very close to the distance for the case of the central cell and thus the effect of the cell boundary enlargement can be considered negligible.

2.2. Possible solutions

As it has been studied in section 2.1.2 in order to correct the ellipticity effect of the external cells the directivity should be increased in the direction of the ellipse long axis ($\phi = 0°$) while maintaining the same directivity in the direction of the ellipse short axis ($\phi = 90°$). This section goes through the different alternatives that have been analyzed as possible solutions to correct the radiation pattern in such a way.

Section 2.2.1 presents the first approach consisting in changing the relative position of the feed with respect to the lens sphere, first changing the tilt angle of the feed with respect to the sphere center and second changing the offset distance of the feed with respect to the sphere center. The second approach is exposed in section 2.2.2, where the lens shape is changed.

2.2.1. Feeds position

The first approach explored to correct the beam footprint was to act on the feed's position with respect to the lens. This section presents the work carried out to analyze the system behavior when changing the tilt angle of the feed with respect to the sphere center and when changing the offset distance of the feed with respect to the sphere center. This work includes the simulation of the changes making use of CST, the measurements obtained in the different situations, the mechanical design of the feed's holders needed to position the feeds in order to carry out the measurements and the conclusions that can be extracted from this analysis.

- **Tilt angle of the feed with respect to the sphere center**

This section exposes the work carried out in the study of the ellipticity correction for the external cells by changing the tilt angle between the feed's longitudinal axis and the radial axis of the sphere orthogonal to the frame structure, see Figure 2.2.1.1.(a) below which has been obtained from the mechanical design performed using SolidWorks, which is the 3D mechanical CAD program used by the EPFL's workshops.

As it can be observed in Figures 2.2.1.1.(a) and 2.2.1.1.(b), a plastic piece has been designed and built to position the feed in the correct place and with the correct orientation during the measurements. Taking into account all the dimensions of the components already machined (i.e. the spherical lens, the frame which holds it in place, the support arc and the feed), this plastic holder has been designed to maintain the feed's aperture at the focal distance with respect to the lens center for all the possible positions of the feed. Moreover, although it cannot be appreciated in these pictures, it has been designed a sticker to be glued on this piece in order to have an accurate enough reference to know the tilt angular position of the feed in each measure.

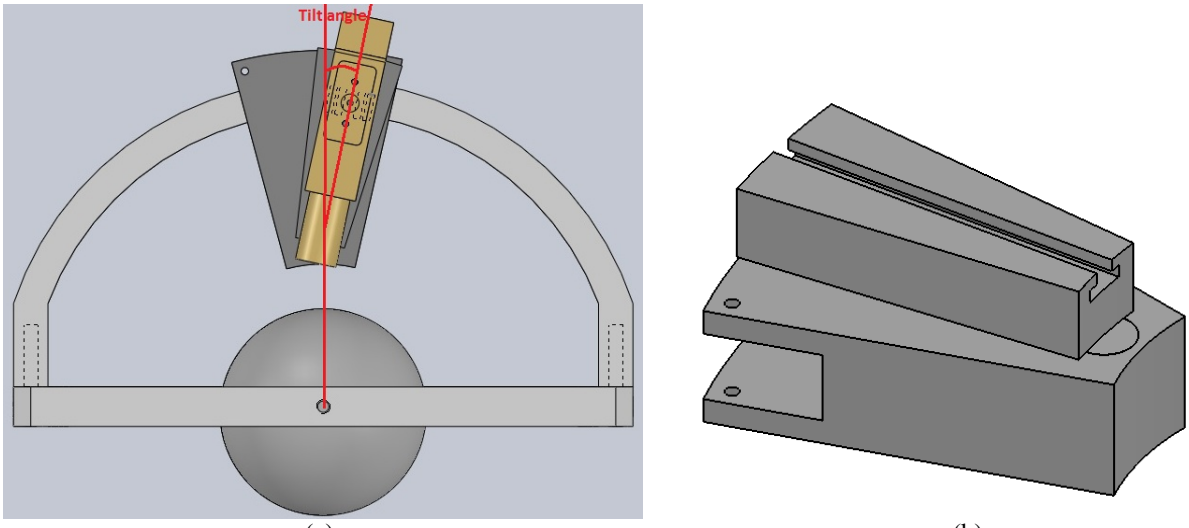

(a) (b)

Figure 2.2.1.1. *SolidWorks design for the tilt experiments. (a) whole system, (b) detail*

Prior to the measurements, this experiment was simulated by means of a full wave analysis making use of CST Microwave Studio. For this simulation, the spherical lens and the cylindrical waveguide feed were modeled using the adequate materials, i.e. brass for the feed and Teflon for the lens, and the dimensions obtained in the design shown in section 1.2, see Figure 2.2.1.2 below. The excitation used for the simulation holds the whole frequency band, i.e. from 27.5 GHz up to 31.3 GHz, and farfield monitors on equally spaced discrete frequency points have been placed in order to analyze the radiation pattern of the system over the frequency span. The background material has been selected as air and the boundaries are set as open boundaries. The mesh precision has to be high enough to model correctly the coaxial transition of the feed (which contains more details) but trying not to mesh too much the lens because it is homogeneous and do not present fine details; if necessary, it is possible to selectively increase the mesh resolution only in the coaxial transition of the feed. Finally all this system is simulated making use of the Transient Solver, which does a broadband calculation of S-parameters from one single calculation run by applying DFT's to time signals.

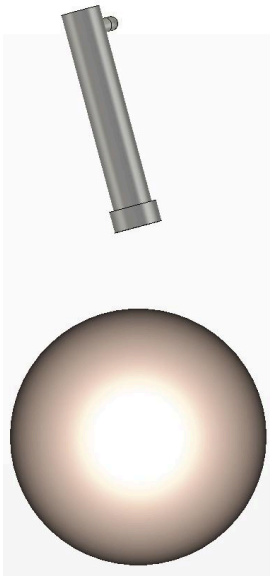

Figure 2.2.1.2. *CST simulation setup for the tilting experiment.*

Last step in the experiment is to determine the accuracy on the simulations by comparing these results with the results obtained from measurements. The scenario depicted in Figure 2.2.1.1.(a) was mounted in LEMA's anechoic chamber, see Figure 2.2.1.3; the transmitting system was fed by a microwave generator and mounted on a rotatory structure, which performed an angular sweep between -30º to 30º. In order to measure the produced radiation pattern it has been used the spinning dipole technique in the receptor, which will engage the possibility to measure the axial ratio when using the polarizer, as it will be explained in section 3. This receptor will be connected to a spectrum analyzer, which in turn is connected to dedicated PC using specialized software developed in LEMA to process the results and store them in a file with an adequate format.

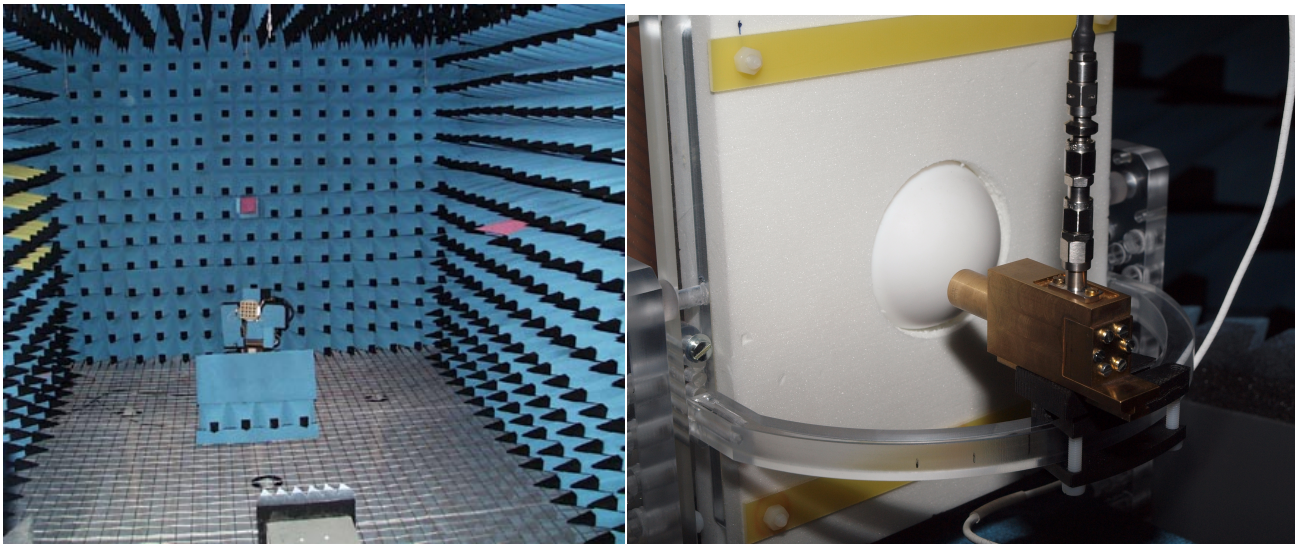

(a) (b)

Figure 2.2.1.3. *Anechoic chamber setup for the tilt experiments. (a) whole setup, (b) transmitter detail*

In order to process results from simulations as well as results from measurements it has been implemented a Matlab script, which reads the text files containing the data and extract the desired information to plot in a graph the most relevant results. In the following Figure 2.2.1.4 it is shown one of the most relevant experiment that have been done on changing the tilt angle with respect to the sphere center; in this case, the angle between the feed's longitudinal axis and the radial axis of the sphere orthogonal to the frame structure is equal to 15º and the frequency under study is 30 GHz.

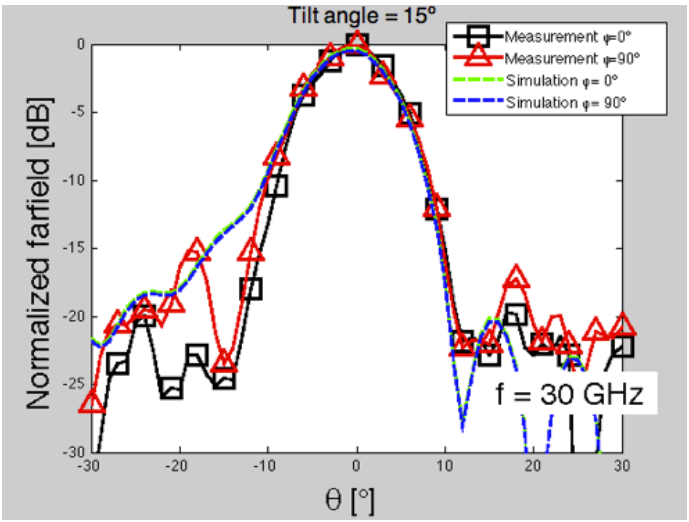

Figure 2.2.1.4. *Radiation pattern on simulations & measurements for tilt angle = 15º*

As it can be observed in Figure 2.2.1.4, results obtained by means of full wave analysis using CST give the same results than the measured results (continuous vs dotted traces) within the region of a cell, i.e. between 0 and -4 dB (which is the normalized power in the cell's boundary) or between -6.8º and 6.8º (which is half of the FoV angle and thus it also determines the cell's boundary). Taking this fact into account, it can be concluded that it is possible relay in the results provided by CST simulations to determine the power distribution on the ground within the cell region in the case of using a feed in combination of the lens.

On the other hand, the objective of this experiment is to determine the validity of this method to correct the ellipticity of the external cells and, as it was demonstrated in section 2.1.2, the solution requires increasing the directivity in the plane $\phi = 0°$. As it can be seen in Figure 2.2.1.4 the directivity is the same for both cutting planes ($\phi = 0°$ and $\phi = 90°$). Therefore, taking into account that results for different tilting angles produce a similar behavior, it can be concluded that this alternative is not valid to compensate the ellipticity effect on the external cells.

By the analysis of Figure 2.2.1.4 further information can be extracted. Due to the fact that the waveguide longitudinal axis does not point to the lens center, the focusing effect given by the lens is not the same than before and thus the directivity is decreased. Furthermore, it can be appreciated a small change in the beam shape coming out of the lens, in this case the beam presents a slight asymmetry. It is interesting to know that this change in the feed position produces an asymmetry in the beam shape because this information may be used for future purposes in deferent scenarios.

Conclusions:

- Same directivity on planes $\phi = 0°$ and $\phi = 90°$ => Solution not valid to correct the ellipticity effect on external cells.
- Agreement between CST simulations' results and measurements results => It is possible to trust on simulations results.
- Waveguide longitudinal axis does not point to the lens center => Overall directivity is decreased.
- Asymmetry in the beam shape => It could be used for future purposes.

• Offset distance of the feed with respect to the sphere center

This section exposes the work carried out in the study of the ellipticity correction for the external cells by changing the offset distance of the feed with respect to the sphere center, see Figure 2.2.1.5.(a) below.

As it can be observed in Figures 2.2.1.5.(a) and 2.2.1.5.(b), a plastic piece has been designed and built to position the feed in the correct place during the measurements. Taking into account all the dimensions of the components already machined (i.e. the spherical lens, the frame which holds it in place, the support arc and the feed), this plastic holder has been designed to maintain the feed's aperture aligned in height with respect to the lens center for all the possible positions of the feed. As it will be discussed later this offset displacement implies that the feeds aperture is no more placed at the focal distance of the lens for any offset different from cero.

Comparing this case with the previous one, where the tilt angle was varied, this time it is easier to determine with high accuracy the position of the feed and thus, instead of designing a sticker to determine the feed position, this time the position was measured making use of a digital caliber.

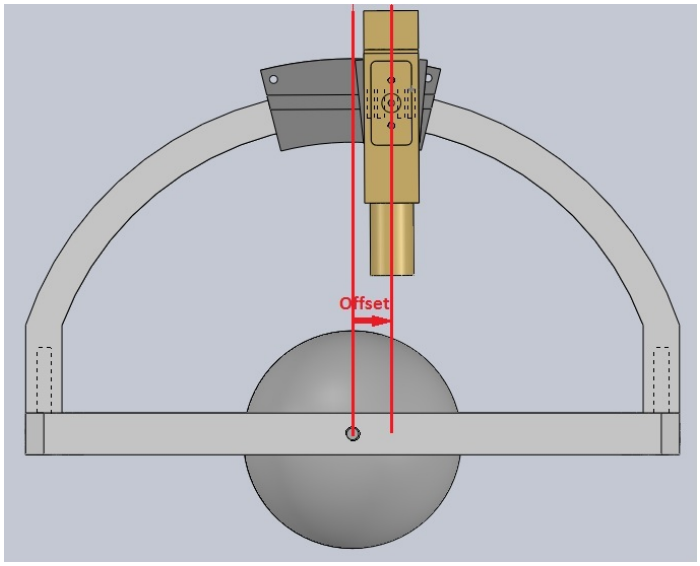

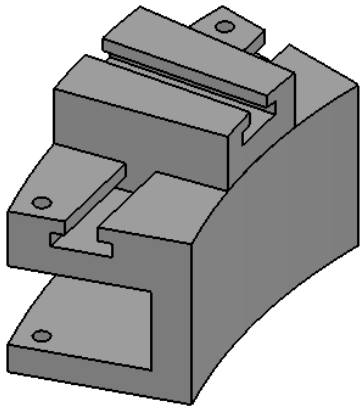

Figure 2.... (b)

Figure 2.2.1.5. *SolidWorks design for the offset experiments. (a) whole system, (b) detail*

Prior to the measurements, this experiment was simulated by means of a full wave analysis making use of CST Microwave Studio. For this simulation, the spherical lens and the cylindrical waveguide feed were modeled using the adequate materials and the dimensions obtained in the design shown in section 1.2, see Figure 2.2.1.6 below. The excitation used for the simulation holds the whole frequency band and farfield monitors have been placed in order to analyze the radiation pattern of the system over the frequency span. The background material has been selected as air and the boundaries are set as open boundaries. The mesh precision has to be high enough to model correctly the coaxial transition of the feed but trying not to mesh too much the lens. Finally all this system is simulated making use of the Transient Solver.

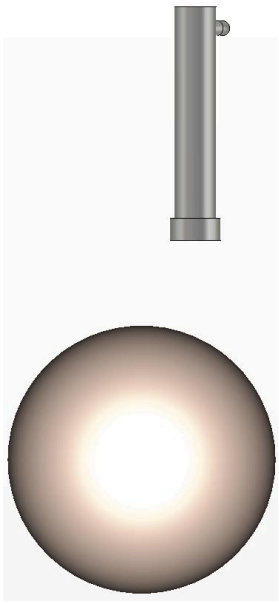

Figure 2.2.1.6. *CST simulation setup for the offset experiment.*

Last step in the experiment is to determine the accuracy on the simulations by comparing these results with the results obtained from measurements. The scenario depicted in Figure 2.2.1.5.(a) was mounted in LEMA's anechoic chamber, see Figure 2.2.1.7; the transmitting system was fed by a microwave generator and mounted on a rotatory structure; this time the angular sweep has been reduced going from -30º to 5º in order to increase the measurements' speed (as it will be analyzed in Figure 2.2.1.8, this angular sector contains the region of interest). In order to measure the produced radiation pattern it has been used the spinning dipole technique in the receptor and it will be connected to a spectrum analyzer, which in turn is connected to dedicated PC using specialized software developed in LEMA to process the results and store them in a file with an adequate format.

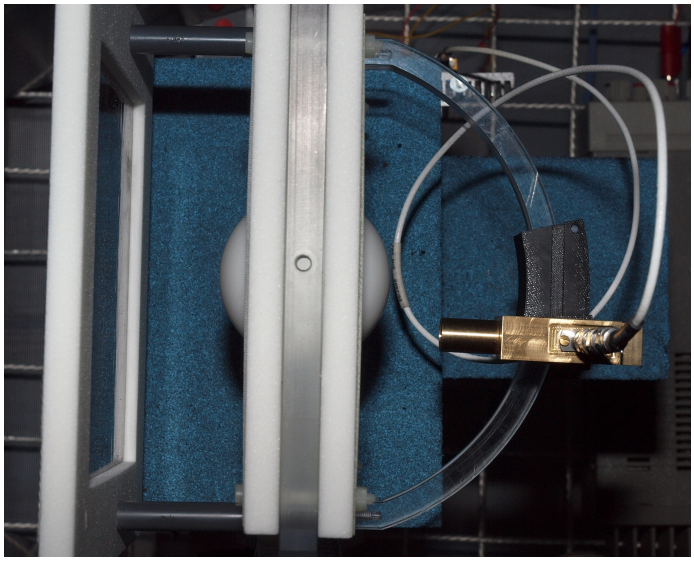

Figure 2.2.1.7. *Anechoic chamber setup for the offset experiments.*

Making use of the Matlab script developed to process results from simulations and measurements, following Figure 2.2.1.8 shows one of the most relevant experiments that have been done on changing the offset distance of the feed with respect to the sphere center; in this case, the offset distance is equal to 12mm and the frequency under study is 30 GHz.

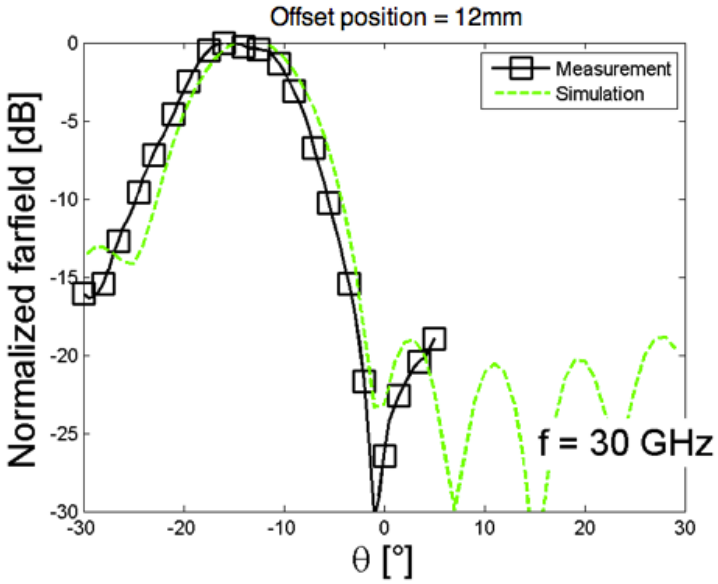

Figure 2.2.1.8. *Radiation pattern on simulations & measurements for offset distance = 12mm*

The most interesting and obvious conclusion about the results given in an offset feed situation is that the beam suffers a steering effect. This effect can be clearly appreciated in Figure 2.2.1.8 where the maximum of the normalized farfield moves from $\theta = 0º$ (in the case of using no offset) to $\theta = -15º$. It is really interesting to know that this change in the feed position produces a steering in the outcoming beam because this situation could be useful for different applications as it will be seen later on. Moreover, using this effect it is possible to change feeds distribution of the complete prototype shown in Figure 1.2.4.4 in order to have a planar distribution of the seven feeds' apertures and thus being more simple to be mounted in the HAPS.

As it can be observed in Figure 2.2.1.8, results obtained by means of full wave analysis using CST give results very close to the measured results (continuous vs dotted traces) over the entire studied angular sector. Taking this fact into account, it can be concluded that it is possible to use simulations to know in advance an estimation of the system behavior.

On the other hand, the objective of this experiment is to determine the validity of this method to correct the ellipticity of the external cells and, as it was demonstrated in section 2.1.2, the solution requires increasing the directivity in the plane $\phi = 0°$ while maintaining the same directivity in the plane $\phi = 90°$. However, the steered case implies a difficulty to realize these measurements: plane $\phi = 0°$ still contains the desired information (it is the plane shown in Figure 2.2.1.8) but now the plane $\phi = 90°$ does not contain relevant information because the beam has been steered, see Figure 2.2.1.9 below. The measurements that were performed only contain the information in planes $\phi = 0°$ and $\phi = 90°$ and, as plane $\phi = 90°$ contains no relevant information it has been decided to represent only plane $\phi = 0°$ in Figure 2.2.1.8. In order to obtain the correct information by means of measurements both transmitting and receiving antennas should be rotated in order to be able to measure the correct plane; however, in the anechoic chamber only the transmitting system is mounted on a rotatory platform and thus not being possible to obtain conclusions on the ellipticity correction from measurements.

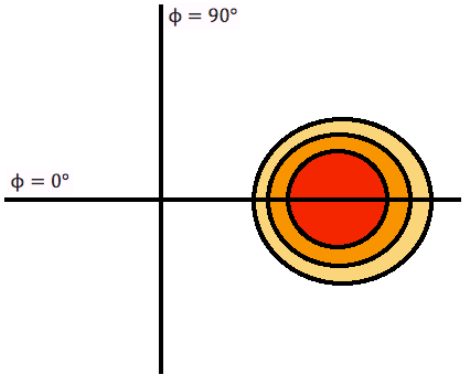

Figure 2.2.1.9. *Measured cutting planes for the offset experiments*

Nevertheless, in order to obtain conclusions on the ellipticity correction in the case of introducing an offset in the feed's position, it has been decided to use the results given by CST simulations in combination with the Matlab tool exposed in section 2.1 to compute the beam footprint produced by this radiation pattern in the considered scenario. Results are shown in Figure 2.2.1.10 below and the information about the ellipticity is shown in Table 2.2.1.1. Taking into account that it has been concluded that it is possible to relay in simulations results due to their agreement with measurements, it

can be assured that this way of studding the ellipticity compensation is consistent. By the observation of these results, and taking into account that results for different tilting angles produce a similar behavior, it can be concluded that this technique is not valid to compensate the ellipticity effect on the external cells.

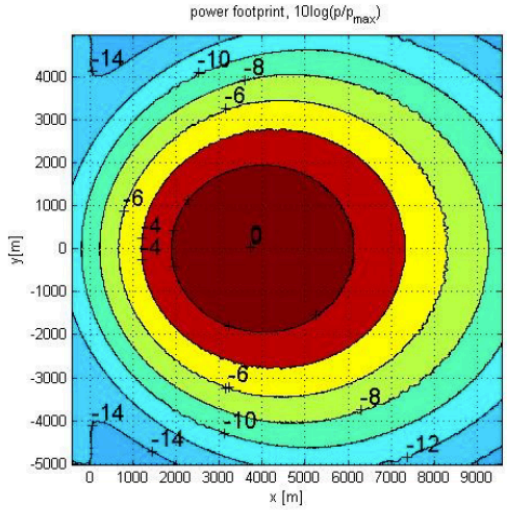

Figure 2.2.1.10. *Power distribution on the ground for the offset experiments*

Ellipse long axis	7403 m
Ellipse short axis	6394 m
Ellipticity	15.8%

Table 2.2.1.1. *Ellipticity of external for the offset experiments.*

By the analysis of the results obtained in this experiment for different offset positions, further information can be extracted. Introducing an offset in the feed's position implies two effects: a shift of the feed's aperture from the focal point and now the waveguide longitudinal axis does not point to the lens center. Therefore, the focusing effect given by the lens is not the same than before and thus the directivity is slightly decreased and the bigger the offset is, the more the beam shape coming out of the lens will change, being no more symmetric. It is interesting to know that this change in the feed position produces an asymmetry in the beam shape because this information may be used for future purposes in deferent scenarios.

Conclusions:

- Similar directivity on the two relevant cutting planes => Solution not valid to correct the ellipticity effect on external cells.
- Feed offset implies a beam steering => Useful to change the feeds' distribution with respect to the lens.
- Agreement between CST simulations' results and measurements results => It is possible to use simulations to know in advance the system behavior.
- Waveguide longitudinal axis does not point to the lens center and aperture moved away from the focal point => Overall directivity is decreased.
- Waveguide longitudinal axis does not point to the lens center and aperture moved away from the focal point => Asymmetry in the beam shape which could be used for future purposes.

2.2.2. **Lens shape**

The second approach explored to correct the beam footprint was to act on the lens shape. This section presents the work carried out to analyze the system behavior when the lens shape is modified in order to increase the focusing effect in a concrete direction. This work includes the simulation of the lens shape modifications by means of a full wave analysis making use of CST Microwave Studio; unfortunately, due to the complexity to manufacture lenses with different shapes this time it has not been possible to compare simulations results with measurements results.

According to the spherical lenses theory exposed in section 1.2.2.1 and taking into account equation 1.2.2.1.1, in order to increase the focusing effect of the lens (i.e. increase the resulting directivity) its cross sectional area have to be increased. On the other hand, as it was demonstrated in section 2.1.2, the solution requires increasing the directivity in the plane $\phi = 0°$ while maintaining the same directivity in the plane $\phi = 90°$. Therefore, in order to increase the focusing effect only in plane $\phi = 0°$, it is necessary to increase the cross sectional area of the lens only for this direction and thus the lens shape is an ellipse with revolution symmetry along its mayor axis, with its mayor axis aligned with $\phi = 0°$ and with its minor axis aligned with $\phi = 90°$, see Figure 2.2.2.1. Maintaining the minor axis with the same dimension as the original spherical lens (i.e. the radius was equal to 30 mm and thus the minor axis is equal to 60 mm) and increasing the lens size along the mayor axis, it is achieved a bigger cross sectional area only in the desired direction.

For the CST Microwave Studio simulation, the elliptical lens and the cylindrical waveguide feed were modeled using the adequate materials and the dimensions obtained in the design shown in section 1.2 for the feed and changing the lens ellipticity, see Figure 2.2.2.1 below. The excitation used for the simulation holds the whole frequency band and farfield monitors have been placed in order to analyze the radiation pattern of the system over the frequency span. The background material has been selected as air and the boundaries are set as open boundaries. The mesh precision has to be high enough to model correctly the coaxial transition of the feed but trying not to mesh too much the lens. Finally all this system is simulated making use of the Transient Solver.

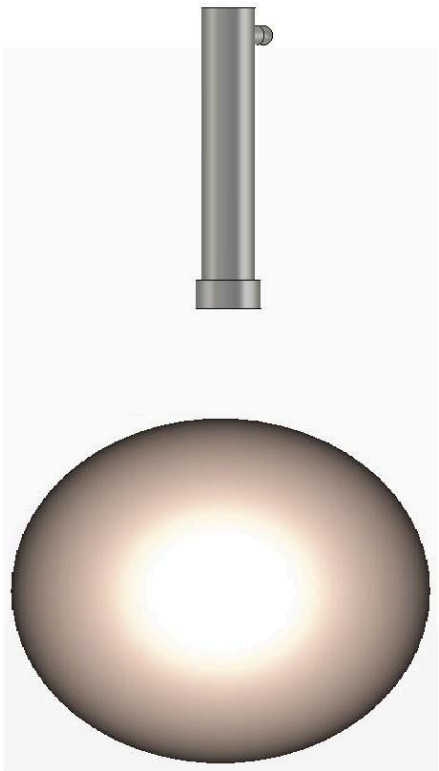

Figure 2.2.2.1. *CST simulation setup for the offset experiment.*

Making use of the Matlab script developed to process results from simulations, following Figures 2.2.2.2 and 2.2.2.3 show one of the most relevant experiments that have been done on changing the lens shape; in this case, the mayor axis of the elliptical lens has been increased 5% with respect to the original size corresponding to the spherical lens and the frequency under study is the central point of the frequency band, 29.4 GHz.

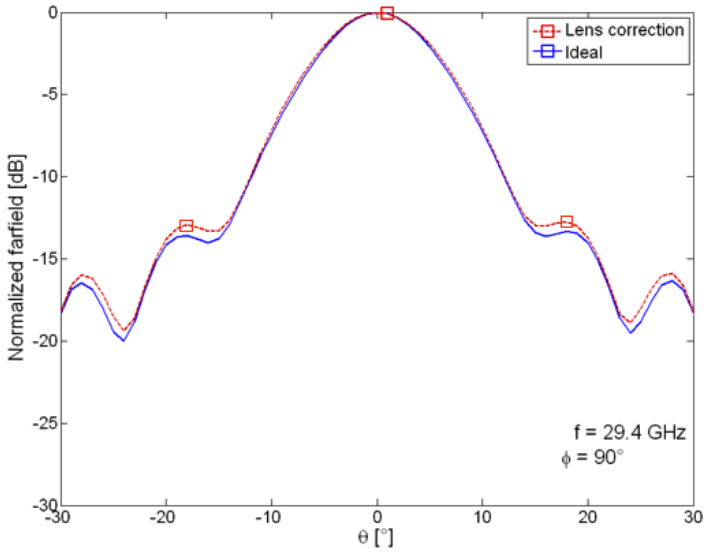

Figure 2.2.2.2 *Radiation pattern on simulations for 5% elliptical lens on* $\phi = 90°$

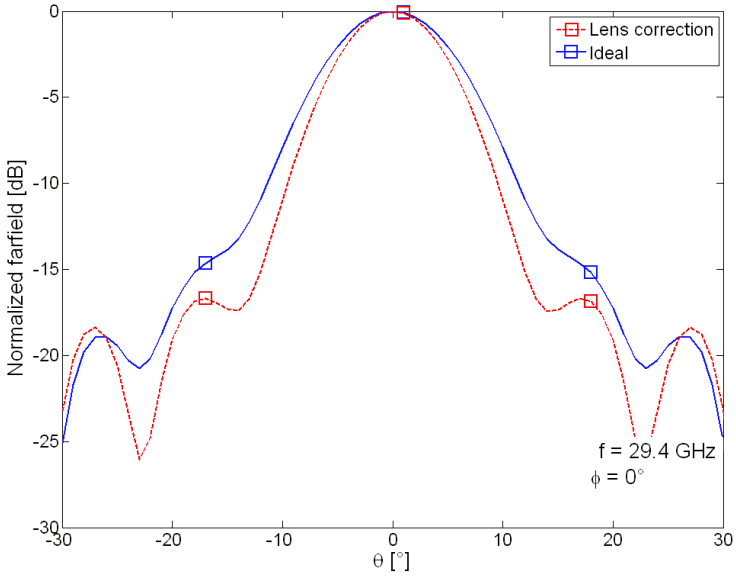

Figure 2.2.2.3 *Radiation pattern on simulations for 5% elliptical lens on* $\phi = 0°$

As it can be observed in Figures 2.2.2.2 and 2.2.2.3, two traces are plotted for both cutting planes. The blue trace is the radiation pattern produced by a spherical lens and it will be used as a reference to check the effects of changing the lens shape.

In Figure 2.2.2.2 it can be seen how the radiation pattern produced for the elliptical lens is the same than the one produced by a spherical lens and thus it can be concluded that changing lens shape in the way that it has been explained in this section does not interfere with the directivity in the $\phi = 90°$ plane. On the other hand, in Figure 2.2.2.3 it can be clearly appreciated the difference between the radiation pattern

produced by the spherical lens and the one produced by the elliptical lens in the $\phi = 0°$ plane; in this case, as the cross sectional area of the lens has increased, the directivity has increased as well.

Therefore, taking into account that results from different experiments shows that the more the ellipticity of the lens is increased the more the directivity in the $\phi = 0°$ plane is increased, it can be concluded that this alternative is valid to compensate the ellipticity effect on the external cells. Moreover, taking into account that results shown in section 2.2.1 demonstrate that acting on the feed position is not possible to correct the ellipticity effect, it can be deduced that the way to compensate the ellipticity effect on the external cells is to act on the radiators, i.e. either on the lens shape as it has been studied on this section or even in the feed's horn or waveguide by adding a small metallization or dielectric piece to change the current distribution in the feeds aperture (this latter idea is proposed as future work but it has not been studied in depth in this project).

The problem of changing the lens shape is that if the lens shape has been optimized to compensate the ellipticity effect on a concrete feed, this lens will not work correctly for a different feed, see Figure 2.2.2.4 where the optimum lens shape has been depicted for feeds corresponding to ports 2 and 3 according to the notation exposed in Figure 1.2.4.4.

Figure 2.2.2.4. *Optimum lens shape for feeds corresponding to ports 2 and 3.*

Therefore, a possible solution to overcome this problem could be to design a lens shape to be the approximation of the lens shape obtained for a concrete feed but with revolution symmetry with respect to the longitudinal axis of the central feed in order to satisfy the requirements for the different positions of the six external feeds. However, due to the complexity to machining a lens with such shape it could be interesting to develop the idea of acting on the feed's horn or waveguide.

Conclusions:

- Same directivity on plane $\phi = 90°$ and increment on the directivity for plane $\phi = 0°$ => Solution valid to correct the ellipticity effect on external cells.
- Acting on the feed position is not valid to compensate the ellipticity effect but acting on the lens shape is valid => In order to compensate the ellipticity effect it is necessary to act on the radiators.
- Optimization of the lens shape for a concrete feed does not work for the other feeds positions. => It is necessary either to design a lens shape with revolution symmetry or study the alternative of acting on the feed's horn or waveguide.

3. External polarizer. MLP

In previous section 1.3 it has been explained how the circular polarization provided by a feed with internal septum polarizer is degraded as the beam passes through the lens and thus it has been decided to study the possibility of removing the internal polarizer in order to perform the polarization conversion after the lens by placing an external polarizer, which changes the polarization for all the beams in the same plane; see Figures 1.3.3 and 1.3.4. Therefore, based in what it has been found in literature about polarizers, the ideal candidate in this scenario would be the MLP (which has been theoretically analyzed in depth in section 1.2.3.4) because it is able to change the polarization of the incoming wave while maintaining low insertion loss, broadband performance and being easy to manufacture. The only special requirement for the MLP in this scenario is that every feed should be positioned to radiate illuminating the MLP with linear polarization in such a way that the electric field forms a 45º angle with respect to the mender-line axis, see Figure 1.2.3.4.3.

This section exposes the work carried out to overcome the polarization degradation problem by using an external MLP. The use of MLPs implies several problems related with the full wave analysis for its simulation and also related with a limitation on the incidence angle; section 3.1 exposes these problems associated with the use of MLPs. Section 3.2 goes through the analysis of the first approach to optimize this structure which makes use of CST Microwave Studio. Finally, section 3.3 exposes the second approach for the MLP optimization, where a transmission line theory optimization procedure has been developed and, making use of it, its performance for orthogonal and for oblique incidence is analyzed.

3.1. Problems associated with MLPs

Although using a MLP as external polarizer after the lens solves the problem of the polarization degradation introduced by the lens, the MLP implies different problems that need to be studied and analyzed in order to try to solve them. Section 3.1.1 presents the description of the problems related with the MLP full wave analysis by means of CST Microwave Studio and section 3.1.2 explains how the problem of the limitation in the incidence angle incurs in the limitation of future applications.

3.1.1. Modeling problems

According to the methodology followed during the project, the MLP was modeled using CST Microwave Studio in order to perform a full wave analysis to simulate its behavior together with the antenna system under study and thus being possible to optimize the structure for the scenario's specifications.

As initial point to model the MLP it has been used the polarizer design proposed by Leo Young in [26], see Figure 3.1.1.1 below. This MLP was designed to work at 10 GHz and thus the initial dimensions were rescaled by a factor of 1/3 for the design of a MLP for the scenario depicted in section 1.1 in HAPS applications. The original design makes use of 4 layers were the inner and the outer layers have different meander

dimensions, this choice is based in the fact that 4 layers is a good compromise between manufacturing ease and a smooth phase change which reduces reflections and increases the effective BW. Therefore, the initial MLP modeled in CST maintains the four-layer feature.

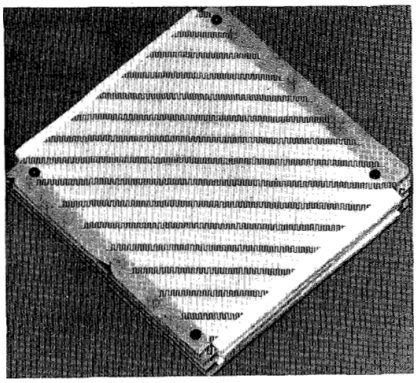

Figure 3.1.1.1. Leo Young *MLP design. [26]*

During the CST modeling it was found that in order to model and simulate an electrically big structure (the biggest boundary of the complete system structure is around $20\cdot\lambda$) containing periodic patterns with dimensions smaller than $\frac{\lambda}{50}$ implies serious difficulties. In order to correctly mesh periodic patterns with such small dimensions it is necessary to increase a lot the mesh resolution and, taking into account that the complete system is a big structure, this incurs in extremely heavy computations requiring huge amounts of memory and producing simulations times which are unacceptable for the optimization process. Figure 3.1.1.2 shows a detail of the mesh resolution in the MLP and, in contrast, Figure 3.1.1.3 exposes the boundaries of the complete system.

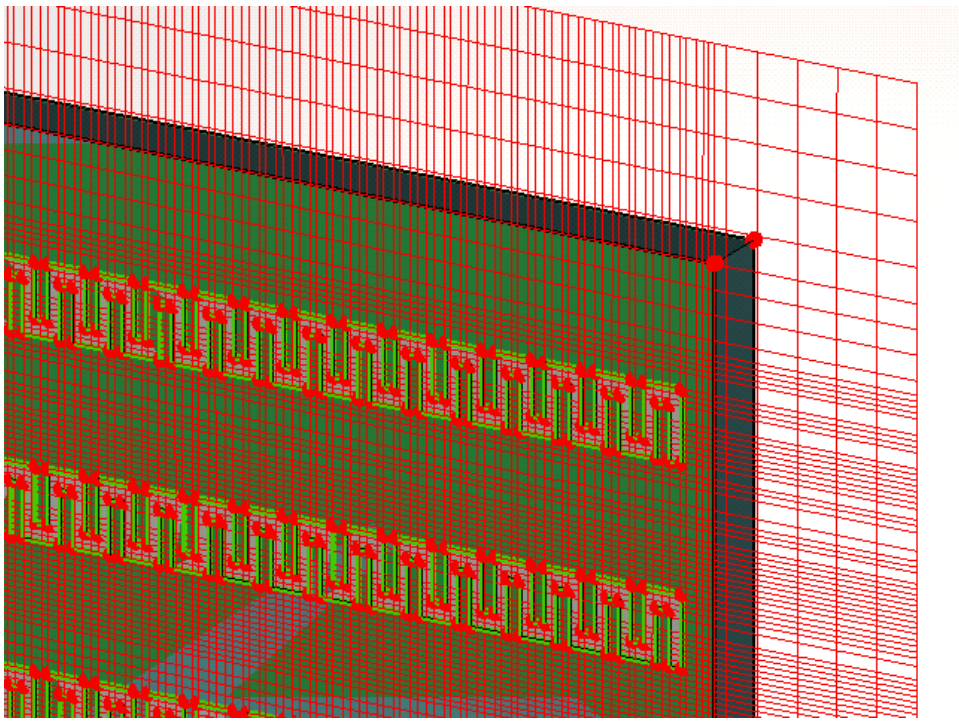

Figure 3.1.1.2. *MLP mesh resolution detail.*

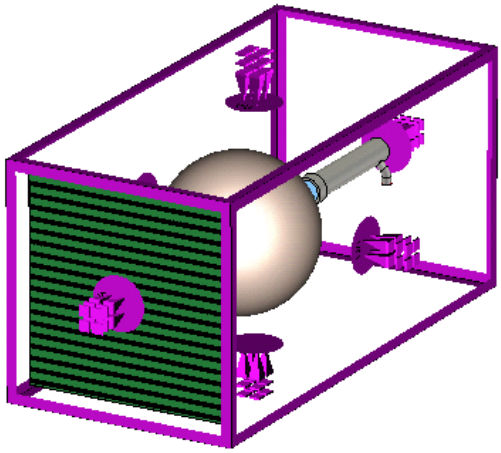

Figure 3.1.1.3. *Boundaries of the complete system.*

Therefore, following the advices of CST Support Team further modeling and simulation techniques were explored. The following sections 3.1.1.1, 3.1.1.2, 3.1.1.3 and 3.1.1.4 expose the different techniques that were analyzed making a comparison between them and choosing the best alternative among them.

3.1.1.1. Frequency Domain Solver using Periodic Boundaries

According to CST Support Team, the Frequency Domain Solver is the better choice if you are looking at electrically small structures, as the meander pattern is. Moreover, key applications for the Frequency Domain Solver are periodic structures being possible to define periodic boundaries.

Consequently, as it can be appreciated in Figure 3.1.1.1.1 below, a MLP structure has been modeled using periodic boundaries and defining a unit cell according to the different meander-lines periodicity for each layer; i.e. due to the fact that the meander-lines periodicity is different for the inner and the outer layers, the unit cell contains the minimum common multiple number of meanders between inner and outer layers.

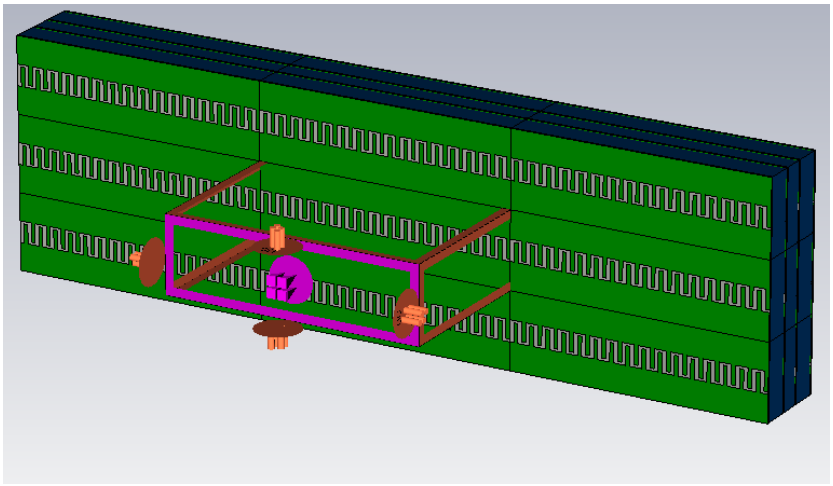

Figure 3.1.1.1.1. *CST Frequency Domain Solver using Periodic Boundaries.*

The problem that this technique implies is that in order to simulate the structure in a big frequency band using the Frequency Domain solver a huge amount of memory is required. Therefore, although different refinements in the solver configuration were tested, every solver run was interrupted abruptly due to the lack of memory in a PC with 8 GB of RAM. Therefore, this simulation technique was discarded.

3.1.1.2. Integral Equation Solver

Taking into account conclusions extracted in section 3.1.1.1 from Frequency Domain Solver, next suggestion given by CST Support Team was to use the Integral Equation Solver which is a specialized solver dedicated to electrically large structures, as is the case when considering the complete system. Integral Equation Solver uses a MoM discretization with a surface integral formulation of the electric and magnetic field.

The way to use the Integral Equation Solver in this scenario requires computing the farfield radiation pattern produced by the feed in combination of the lens. Once this result is recorded in a file, it may be used as the farfield excitation for the MLP. Following Figure 3.1.1.2.1 shows the system model that has been used to capture the farfield radiation pattern which will be used to excite the MLP. Figure 3.1.1.2.2 subsequently expose how the captured pattern is used as far field excitation for the four-layers MLP.

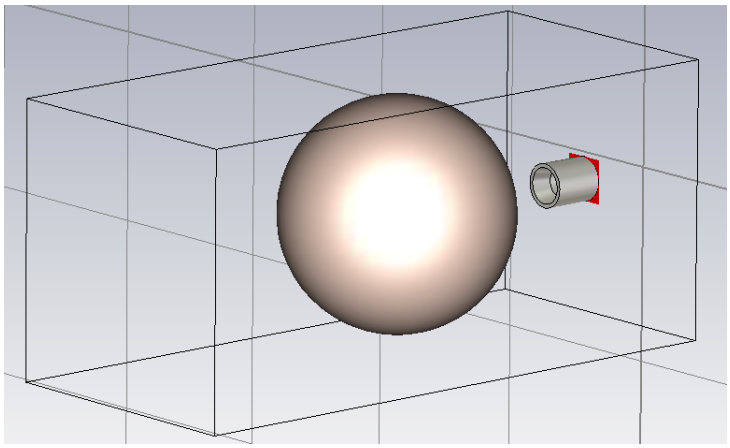

Figure 3.1.1.2.1. *CST Integral Equation Solver equivalent circuit to capture the farfield radiation pattern.*

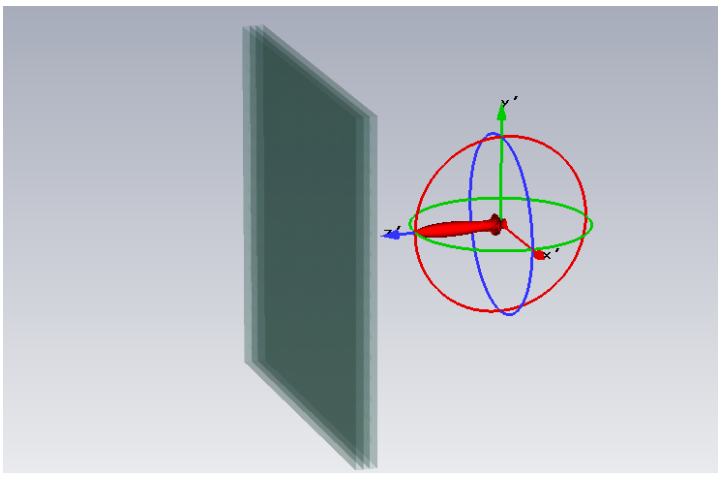

Figure 3.1.1.2.2. *CST Integral Equation Solver MLP farfield excitation.*

The problem that this technique implies is that, in order to simulate an electrically large structure which contains periodic patterns with dimensions smaller than $\frac{\lambda}{50}$, very heavy computations are required and thus the simulation time is very long. Therefore, although different refinements in the solver configuration were tested, the simulation time was longer than one week in a PC Intel Xenon at 2.8 GHz and 16 GB of RAM. Therefore, the simulation time was not compatible with any optimization process and thus this simulation technique was discarded.

3.1.1.3. Transient Solver using Plane Wave Excitation

Taking into account conclusions extracted in sections 3.1.1.1 and 3.1.1.2 from Frequency Domain and Integral Equation Solvers, next suggestion given by CST Support Team was to come back to the simulation technique that was used as first instance but including only the MLP in the system design and using a plane wave with linear polarization oriented to form a 45º angle with respect to the meaner-line axes to excite the structure. This way, the system design would be simplified and thus the simulation time should be considerably reduced; additionally the Transient Solver should be more effective because it does a broadband calculation of S-parameters from one single calculation run by applying DFT's to time signals. Figure 3.1.1.3.1 depicts the model used in these simulations where it can be seen the MLP structure excited by a plane wave linearly polarized and showing the 45º polarization angle.

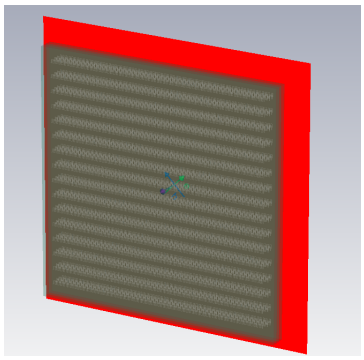

Figure 3.1.1.3.1. *CST Transient Solver using Plane Wave Excitation.*

The problem that this technique implies is that using an infinite plane wave the radiation suffers diffraction in the MLP edges. In the real scenario, where the beam is focused by the lens in certain region of the MLP surface, this diffraction is not the same. Therefore, although the simulation time was considerably reduced, this simulation technique was discarded.

This effect can be appreciated in following Figure 3.1.1.3.2 where a comparison is shown between the Inverse Axial Ratio produced in a plane wave excitation situation and the one produced when simulating the complete system, i.e. feed plus lens plus MLP (Inverse Axial Ratio is the most confortable way to study the quality of the circular polarization in this case.

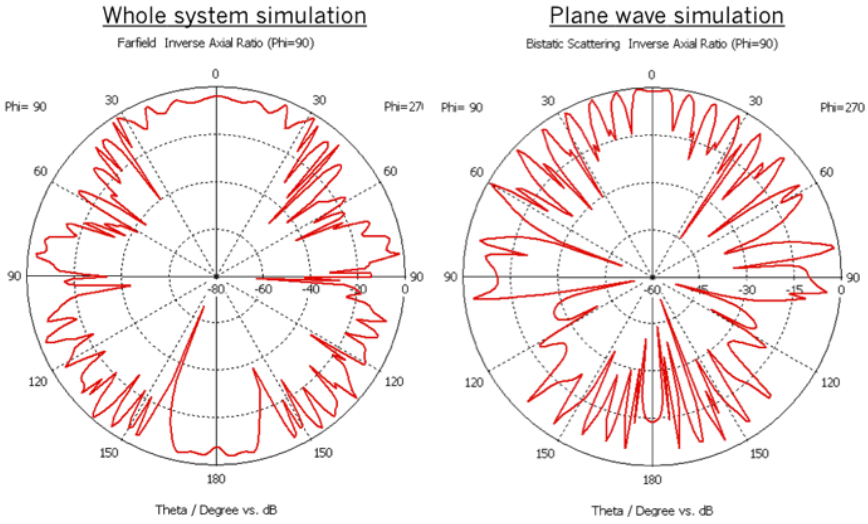

Figure 3.1.1.3.2. *Axial Ratio comparison for different CST Transient Solver simulations techniques.*

3.1.1.4. Transient Solver using the complete system

Taking into account conclusions extracted in sections 3.1.1.1, 3.1.1.2 and 3.1.1.3 from Frequency Domain, Integral Equation and Transient Solvers; it was decided to use the Transient Solver which gave the shortest simulation time among the solvers studied. However, as it has been explained in section 3.1.1.3, due to diffractions it is necessary to simulate the complete system. Figure 3.1.1.4.1 below shows the complete system structure used to analyze this simulation technique in this section.

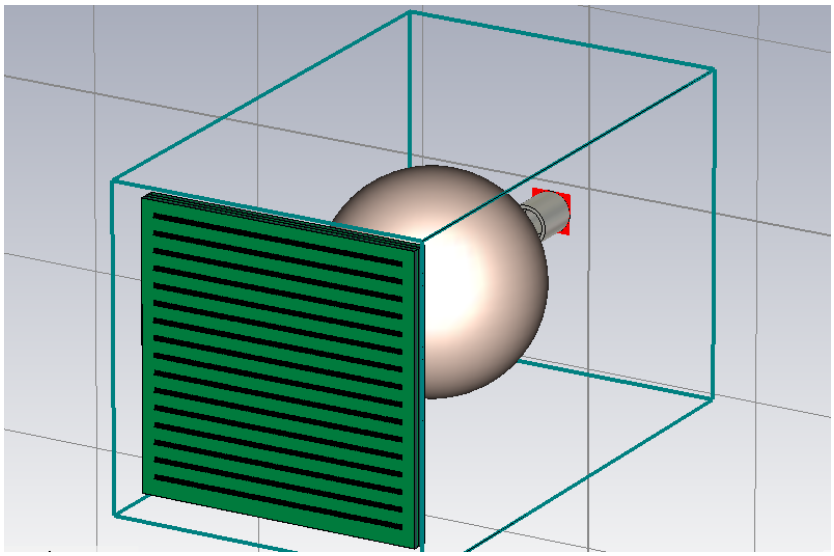

Figure 3.1.1.4.1. *CST Transient Solver complete system setup.*

As it has been already noticed, due to difficulty to choose an adequate mesh resolution for the complete system, this technique implies quite demanding requirements for the PC where the simulation is run. However, it has been simulated on the LEMA server PC (Intel Xenon at 2.8 GHz and 16 GB of RAM) producing around 12 hours simulation time. This long simulation time is not adequate to perform an optimization process but it is acceptable to check how changes in the meander dimensions affect the system behavior. Therefore, this is the simulation technique that was chosen to optimize the MLP in the first approach.

3.1.2. Limitation on the incidence angle.

By placing the polarizer after the lens it is obvious that the problem of the polarization degradation as the wave passes through the lens is solved. However, using a planar MLP polarizer, as it is depicted in Figure 1.2.4.1, a new source of polarization degradation comes up. The electrical characteristics of the meander-line structure remain almost constant for small deviations of wavefront propagation directions with respect to the orthogonal incidence case. On the other hand, when the incidence angle of the wavefront (which is defined as $\tilde{\theta}$ according to Figure 3.1.2.1) differs a lot from the orthogonal incidence case ($\tilde{\theta}=0$), the electrical characteristics of the meander-line structure are seen as different for this wave and thus the polarization conversion is not the same. This effect implies a degradation of the circular polarization as the incidence angle increase.

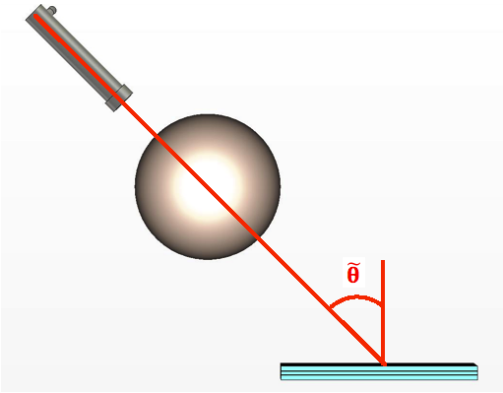

Figure 3.1.2.1. *Definition of the incidence angle.*

Traditional trend to overcome this problem was to develop conformal polarizers which lead to a situation where the incidence angle is seen as perpendicular for every propagation direction as Leo Young made in [26], check Figure 3.1.2.2 below. However, this alternative is not mechanically feasible in a scenario as the one depicted within the scope of this project where a conformal MLP should by machined in a spherical shape.

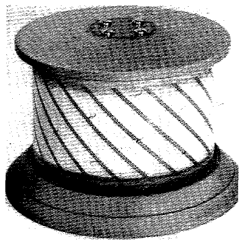

Figure 3.1.2.2. *Conformal MLP, [26].*

In order to characterize polarization degradation effect with the incidence angle, following Figure 3.1.2.3 shows how the AR increase with the incidence angle. A 3 dB axial ratio implies elliptical polarization where the ellipse's mayor axis is twice bigger than the minor axis and thus the polarization can no more be considered as cylindrical. Therefore, 3 dB is set in the plot as the boundary to consider the polarization as circular. Moreover, this Figure indicates by red lines the angles corresponding to the positions of the feeds belonging to the first and second ring of feeds around the central one.

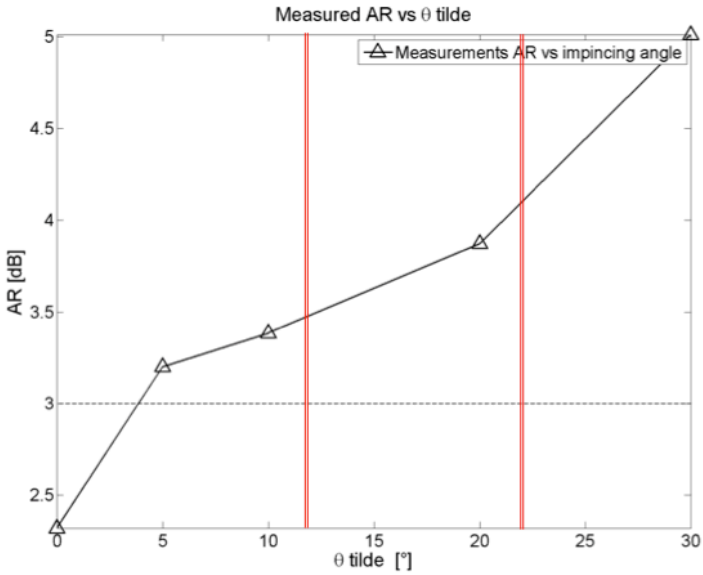

Figure 3.1.2.3. *AR degradation with the incidence angle.*

As it can be appreciated in Figure 3.1.2.3, a MLP optimized for orthogonal incidence cannot be used in the scenario specifications, i.e. cannot be used to provide a 7 cells cluster. Consequently, this effect of polarization degradation with the incidence angle limits the number of feeds that can be used in the case of implementing a planar MLP to achieve circular polarization. Therefore, the extension of this system to create bigger clusters with more cells is constrained, see Figure 3.1.2.4.

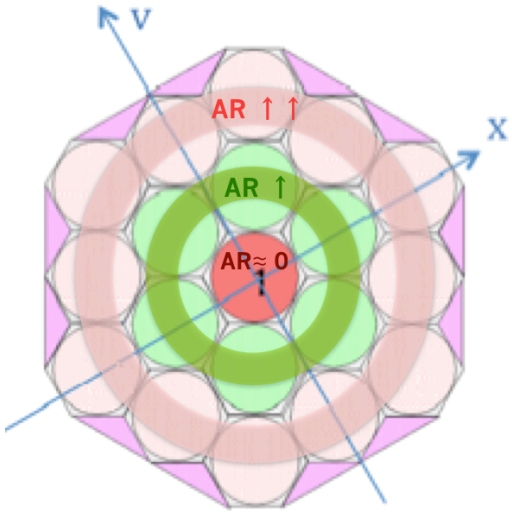

Figure 3.1.2.4. AR degradation in a *extended cluster with 19 cells*.

Figure 3.1.2.4 depicts a scenario with a cluster including 19 cells; this scenario could be useful to exemplify the effect of the axial ratio degradation in the outer cells. The situation could be the following: the central cell (red cell) presents very good axial ratio and thus all the services could be provided with no problems concerning the polarization, in the first ring of cells (green cells) the AR is higher and thus some services could presents some problems concerning the polarization and in the second ring of cells (pink cells) the AR degradation is so strong that services requiring circular polarization can not be provided.

3.2. CST optimization

As a first approach it was tried to optimize the MLP making use of full wave analysis by means of CST Microwave Studio. As it was stated in section 3.1.1, the optimization of this structures using full wave analysis is very difficult because the simulation time is too long to run the optimizer and thus the only way to deal with such structure for optimization is to simulate how the system behavior changes when some parameter of the structure is modified.

This section summarizes the work carried out on the first approach to optimize the MLP, i.e. using full wave analysis. Section 3.2.1 exposes the optimization procedure that it has been used. Once a MLP model was designed and optimized, the prototype was machined in LEMA and thus section 3.2.2 shows the building and assembling process. Finally, the prototype was mounted in the anechoic chamber and measurements were taken in order to characterize the MLP model; section 3.2.3 shows the measurement procedure, depicts the obtained results and extracts some conclusions.

3.2.1. Optimization procedure

In order to optimize the MLP for the scenario specifications, it has been decided to simulate the system behavior for different meander dimensions in order to check which values produce better results in this scenario. For this simulation, the spherical lens and the cylindrical waveguide feed were modeled using the adequate materials, i.e. brass for the feed and Teflon for the lens, and the dimensions obtained in the design shown in section 1.2. For the MLP, materials have been chosen according to workshop availability and also according to their characteristics, i.e. Rohacell has been chosen as the material used to create the correct spacing between meander-line layers because it presents a permittivity close to the air permittivity and Kapton has been chosen as the meander-line metallization substrate because it presents a small thickness (100µm) and small losses.

The excitation used for the simulation holds the whole frequency band, i.e. from 27.5 GHz up to 31.3 GHz, and farfield monitors on equally spaced discrete frequency points have been placed in order to analyze the radiation pattern of the system and its AR over the frequency span. The background material has been selected as air and the boundaries are set as open boundaries. The mesh precision has to be high enough to model correctly the meander-line pattern but trying not to mesh too much the lens because it is homogeneous and do not present fine details. Finally, all this system is simulated making use of the Transient Solver, according to the results exposed in section 3.1.1. Following Figure 3.2.1.1 shows the resulting model used to study the system behavior in the case of orthogonal incidence.

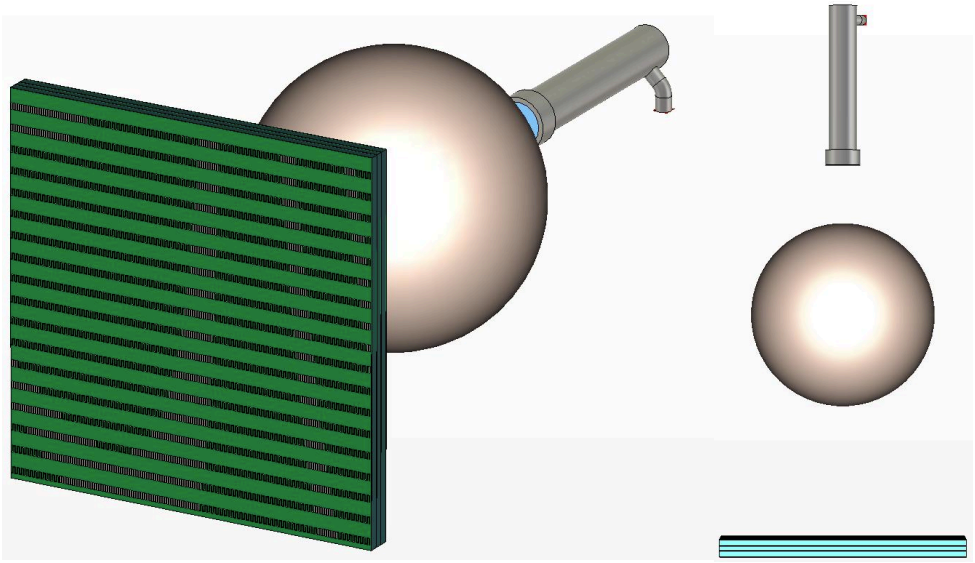

(a) (b)

Figure 3.2.1.1. *CST system model in orthogonal incidence. (a) perspective and (b) top view.*

MLPs have a wide range of parameters to define their geometry: meander-lines spacing, meander-lines periodicity, meander-lines height, meander-lines width, meander-lines dielectric permittivity, meander-lines dielectric thickness, spacers thickness and spacers permittivity. It is evident that it is not feasible tiring to optimize the MLP adjusting all these variables, nevertheless in section 1.2.3.4 it has been exposed the Terrent's results on changing different MLP parameters in [32]. This analysis explains that the parameters with a bigger influence on the AR are the spacing between the meander-lines on each layer, the meander-lines height and the meander-line width.

Therefore, it has been decided to reduce to two the number of parameters to be varied in the optimization process: the spacing between the meander-lines on each layer and the meander-lines height. Trying to maintain a reasonably low number of variables, the meander-line width has not been taken into account in the optimization because, according to the initial MLP modeling from the original Leo Young's model [26], the meander-line presents to different widths (the one corresponding to the vertical stretches and the one corresponding to the horizontal stretches). However, according to the original model ([26]), meander-line parameters are different between inner and outer layers and thus number of variables are no more two but four: spacing between the meander-lines on the outer layers, spacing between the meander-lines on the inner layers, meander-lines height on the outer layers and meander-lines height on the inner layers.

Although the process of manual optimization of the MLP using four variables requires a lot of effort and time, it has been performed numerous simulations trying to adjust these parameters for the scenario specifications. The optimization ideally aims to achieve low insertion loss and low AR over the whole working frequency band and to maintain it low also in the case of non-orthogonal incidence. However, is not feasible to work with so many optimization goals and thus, taking into account the intrinsic characteristics of the MLP (low insertion loss and broadband performance), it has been decided to choose the AR in the central frequency for the orthogonal incidence case as the criterion to compare between different parameters configurations. Nevertheless farfield monitors have been used over the whole frequency span to check the system BW and also the system has been modeled for different cases of oblique incidence (see Figure 3.2.1.2 below) to check the system behavior in these scenarios.

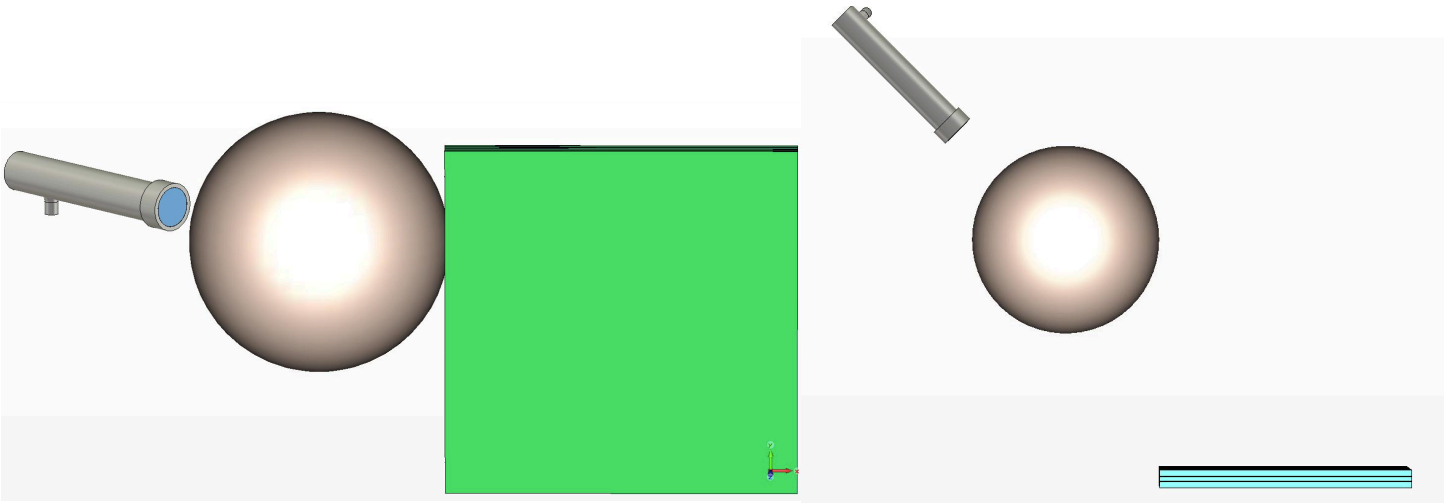

(a) (b)

Figure 3.2.1.1. *CST system model in oblique incidence. (a) perspective and (b) top view.*

Optimization results produced during these simulations will be studied in section 3.2.3 together with measurement results in order to be able to make a comparison between them and extract conclusions.

3.2.2. Prototyping

Once the MLP dimensions has been optimized according to section 3.2.1, it was machined a first prototype of this MLP model. This section goes through the prototyping process developed at EPFL including: the spacers cutting and milling process, the meander-line layers photoetching process and the assembly process.

The foam spacers, who accurately create the correct distance between meander-line layers, have been designed according to the rescaling of the original Leo Young's model ([26]) and thus they present a thickness which is not available among the materials present in the workshop (it is neither a standard width given by any manufacturer). Therefore, in order to produce the designed spacers it was needed to mill the foam spacer with a digital precision milling machine in order to create a flat structure with the desired thickness. The material used to build the spacer is Rohacell. Figure 3.2.2.1 below shows the milling process of the spacers.

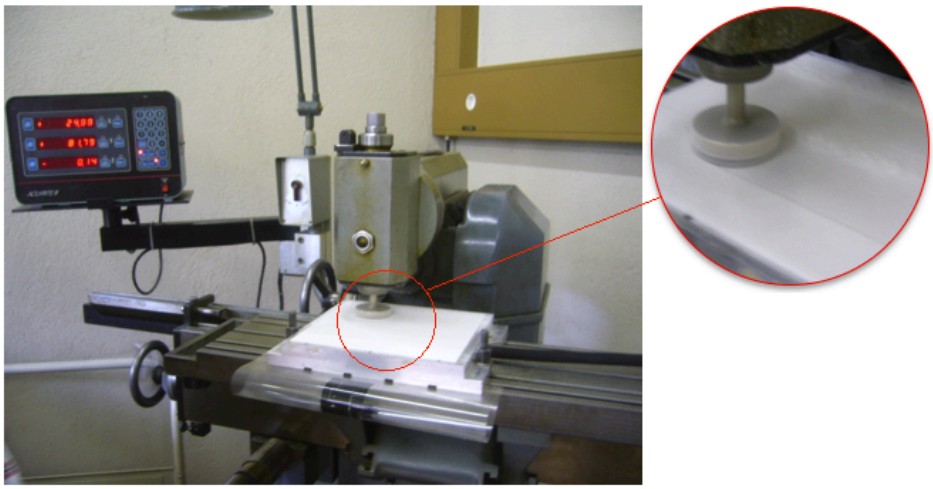

Figure 3.2.2.1. *Spacers milling process.*

Once the foam has been milled to achieve the desired thickness, it is necessary to cut the spacer pieces not only with the correct dimension but also being sure that their edges form a 90º angle. Therefore, as it can be seen in Figure 3.2.2.2 below, the spacer pieces were cut with a high precision cutting machine. Once they were cut, they were ready to be mounted between meander-line layers.

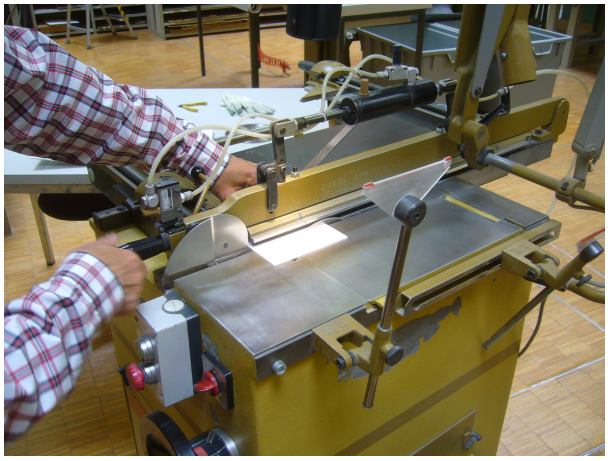

Figure 3.2.2.2. *Spacers cutting process.*

Next step to build the prototype was the manufacturing of the meander-line layers. A piece of 100 µm thickness Kapton dielectric with a cooper film over both sides was cut into different pieces according to the MLP dimensions (see Annex 2) to be used as meander-line layers, as it can be seen in Figure 3.2.2.3 below.

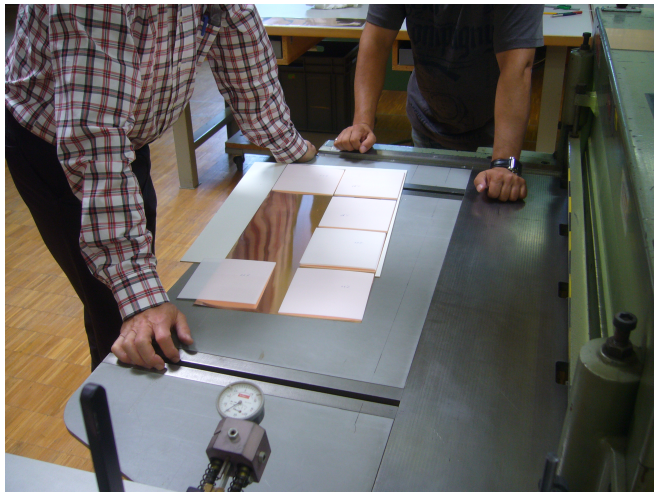

Figure 3.2.2.3. *Meander-line layers cutting process.*

In order to obtain the meander-lines from the cooper film over one side of the dielectric layers, different masks have been designed for the different layers, i.e. a mask for the inner layers and a different one for the outer layers. Design process of a mask consist in the following steps:

1. Using the CST model of the polarizer, extract the meander-lines of one layer. Then, add a frame as a visual aide to cut the layer with the correct dimension. The resulting CST design can be observed in Figure 3.2.2.4 below, where it can be appreciated the 45º orientation of the meander-lines which make easier the feeds mounting while maintaining the 45º angle with the electric field.
2. Export the CST design with a file format compatible with SolidWorks. Then, import this file into SolidWorks and use this design to create the mechanical draw which will be used as reference in following steps of the prototyping. The mechanical draws of the different layers prototyped are shown in Annex 2.
3. Export the SolidWorks project with a file format compatible with the high precision laser printer and print the mask that will be used in a photoetching process.

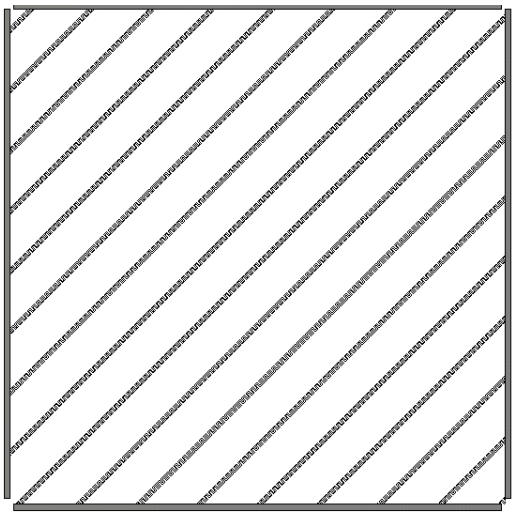

Figure 3.2.2.4. *CST design of the layer mask.*

Once the masks are prepared, they can be used in thee photoetching process to obtain the meander-lines in one side of the layers and remove all the cooper from the other side. The photoetching process involves the following steps:

1. Apply a photosensitive film to the entire layer uniformly.
2. Hold the mask over the layer and apply light, see Figure 3.2.2.5(a). The mask will prevent the meander-lines to receive light.
3. Develop the layers to remove the photosensitive film from the entire surface except on the meander-lines and on the edges.
4. Expose the layer to an acid bath to remove the cooper, see Figure 3.2.2.5(b). The photosensitive film on the meander-lines will prevent from removing the cooper in these areas.
5. Remove the photosensitive film from the meander-lines with alcohol.

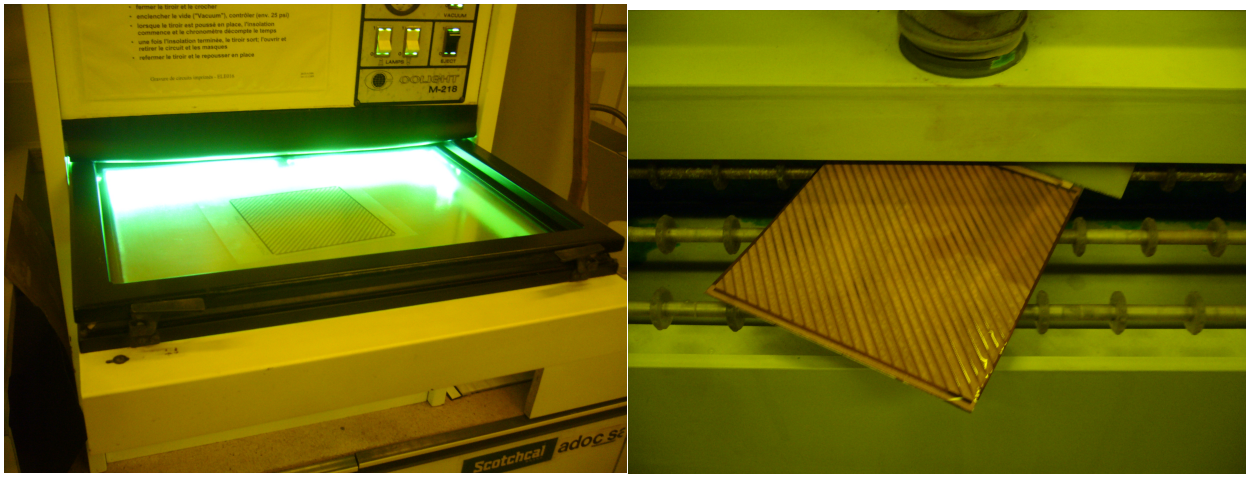

(a) (b)

Figure 3.2.2.5. *Photoetching process. (a) Light exposure. (b) Acid development.*

The last step to complete the meander-line layers is to cut the frame out of the layers paying attention to remove all the cooper in order to avoid shortcicuits between the meander-lines.

As soon as all the pieces of the MLP were finished, the final prototype was mounted by assembling and holding together all the layers while paying attention to the alignment. In order to glue together all the layers, a thick film of gluing material was inserted between each layer (this material has an extremely low permittivity and thickness and thus it should not interfere in the final system behavior). Figure 3.2.2.6 shows the assembling process.

Figure 3.2.2.6. *Assembling process.*

Finally, holding the structure between to metal plates the prototype was inserted into an oven and the gluing material was melted holding together al the layers. The final result is shown in Figure 3.2.2.6 where it can be clearly appreciated the meander-lines and the different layers which conform the MLP prototype.

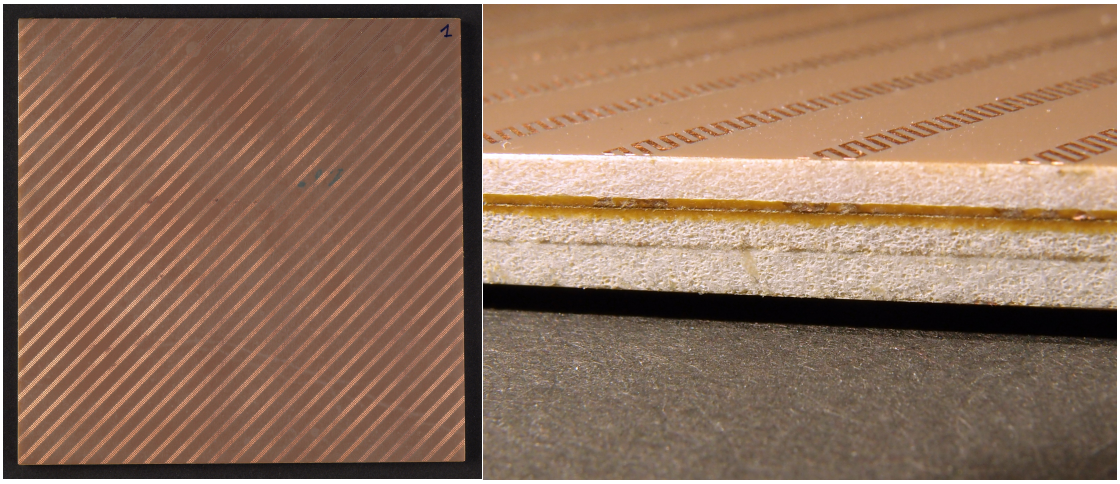

Figure 3.2.2.6. *Final prototype.*

3.2.3. Measurements

Once the MLP prototype is finish, everything is ready to perform the measurements which will characterize the MLP performance under the scenario's conditions. The complete antenna system was mounted in LEMA's anechoic chamber as it can be seen in Figure 3.2.3.1(a); the transmitting system was fed by a microwave generator and mounted on a rotatory structure, which performed an angular sweep between -30º to 30º. In order to measure the produced radiation pattern and AR it has been used the spinning dipole technique in the receptor. This technique provides maximum and minimum received power for each transmitter position and frequency, which corresponds to the mayor and minor axes of the elliptical polarization, and thus it is possible to compute the AR. This receptor will be connected to a spectrum analyzer, which in turn is connected to dedicated PC using specialized software developed in LEMA to process the results and store them in a file with an adequate format. Figure 3.2.3.1(b) shows the anechoic chamber setup.

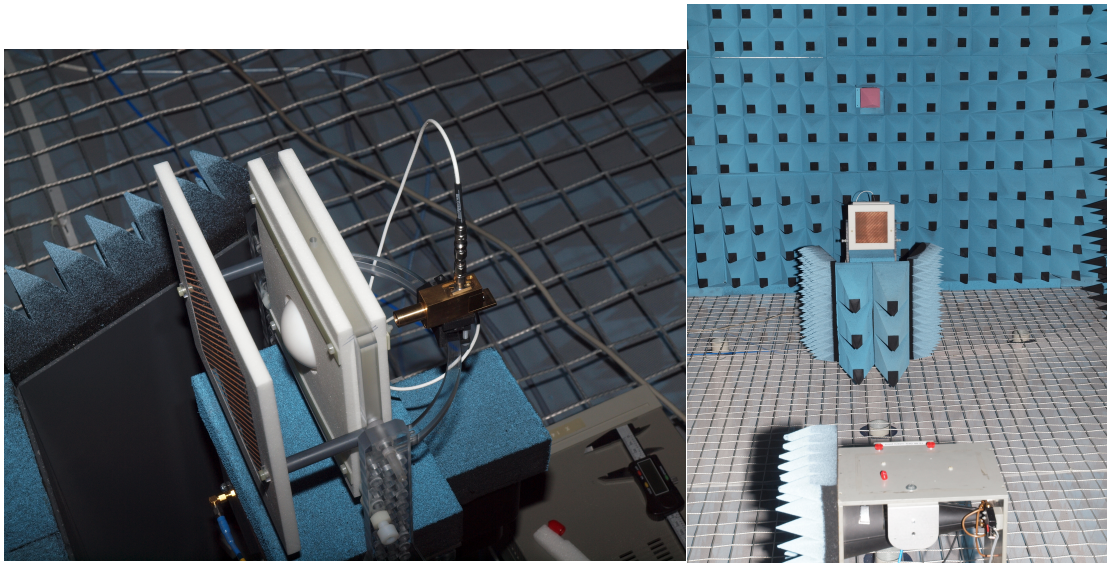

(a) (b)

Figure 3.2.3.1. *Anechoic chamber setup. (a) Transmitter system setup, (b) general setup*

In order to process results from simulations as well as results from measurements it has been implemented a Matlab script, which reads the text files containing the data and extract the desired information to plot in a graph the most relevant results. In the following Figure 3.2.3.2 it is shown one of the most relevant experiment that have been done for orthogonal incidence; the AR is monitored over the whole frequency band comparing the performance between two different models in simulations and the measured performance for the model that was prototyped.

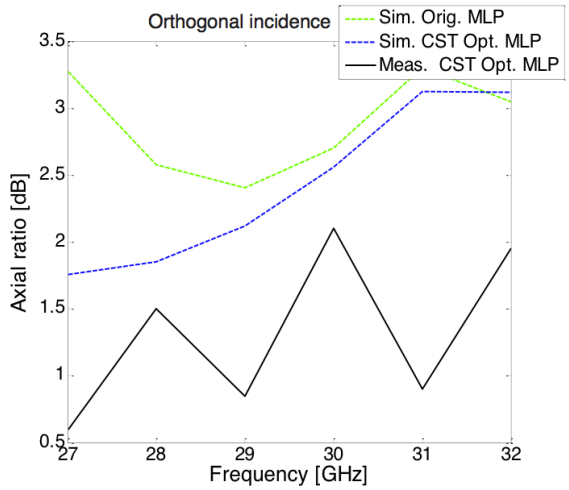

Figure 3.2.3.2. *Simulated and measured AR vs frequency*

As it can be appreciated in Figure 3.2.3.2, the improvement achieved in the MLP polarizer is very samall when comparing simulation results for the rescaled version of the Leo Young's original model [26] (green dotted line) with the simulation results for the optimized model (blue dotted line). The reason for this small improvement is that, as it has been explained in section 3.1.1, heavy computations and long simulation times lead to an extremely difficult optimization process. However, as it can be concluded from the observation of the measurements results for the optimized model (black continuous line), the simulation results can be used to have an estimation of the system behavior and thus being possible to notice improvements as it has been done; but simulations results are not accurate enough to predict the exact behavior of the system and actually the measured results demonstrate that the real performance is better than the one given by simulations. The reason to have a disagreement between simulation and measurement results is that the mesh resolution has been adjusted to provide a reasonable simulation time and thus not being possible to mesh the meander-line pattern with the adequate resolution.

Therefore, it can be concluded that the MLP prototype presents a good performance under the scenario conditions for orthogonal incidence providing an AR lower than 3 dB over the whole frequency band. However, as it can be deduced from the comparison of simulation results in Figure 3.2.3.2, the CST optimization process leads to small improvements in the system behavior and thus it cannot be considered as an efficient optimization technique.

On the other hand, as it has been explained in the scenario specifications, the use of several feeds to create multicell clusters implies oblique incidence for the case of the external feeds and thus it is also necessary to monitor the system behavior for different incidence angles. In order to perform these measurements the feed's position has been manually varied on the holding arc (see Figure 3.2.3.3) and the system behavior has been measured for different feed's position using the same technique as the one used in last measurements.

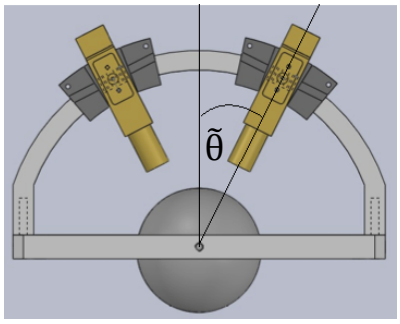

Figure 3.2.3.3. *Change of the feed's position.*

In order to process results from these measurements it has been implemented a different Matlab script, which reads the text files containing the data and extract the desired information to plot in a graph the most relevant results. In the following Figure 3.2.3.4 it is shown one of the most relevant experiment that have been done for the MLP prototype and for different incidence angles; the worst case AR (i.e. the worst AR measured over the frequency band), the best case AR and the average case AR (i.e. the average of the different ARs measured over the frequency band for each feed position) are monitored in Figures 3.2.3.4(a), (b) and (c) respectively.

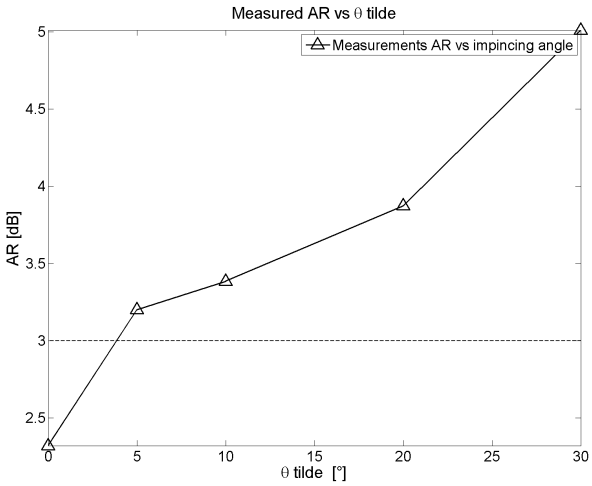

(a)

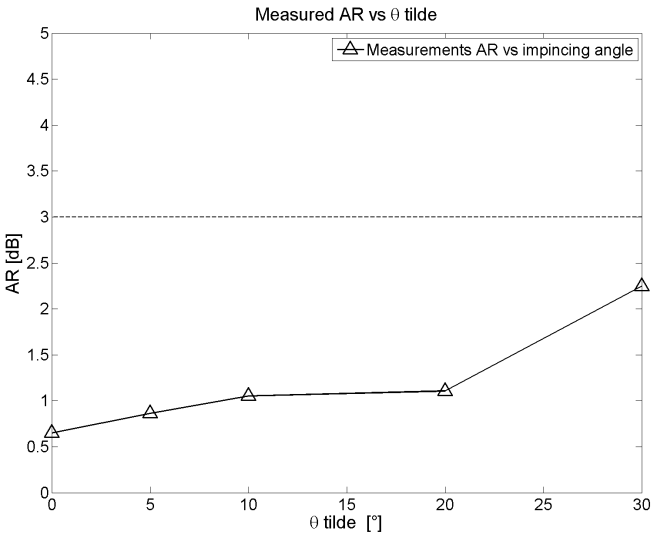

(b)

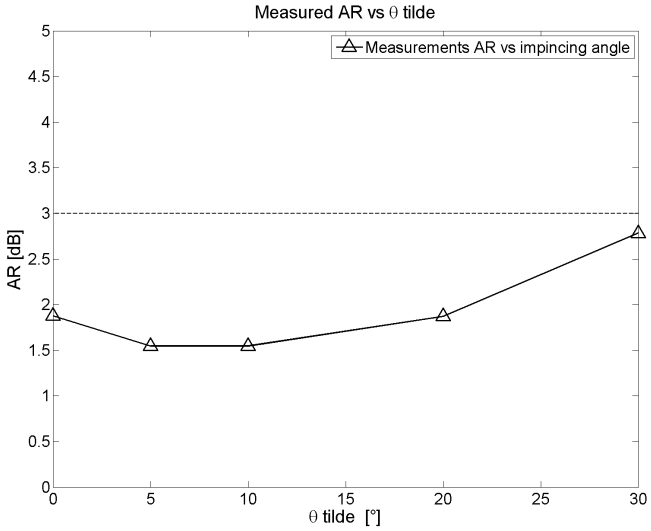

(c)

Figure 3.2.3.4. *Measured AR vs incidence angle for the worst case (a), best case (b), and average (c).*

A 3 dB axial ratio implies elliptical polarization where the ellipse's mayor axis is twice bigger than the minor axis and thus the polarization can no more be considered as cylindrical. Therefore, 3 dB is set in the plot as the boundary to consider the polarization as circular. Consequently, from the observation of Figures 3.2.3.4(b) and (c) it can be concluded that the designed MLP prototype is robust against changes in the incidence angle. However, taking into account Figure 3.2.3.4(a), it must be said that the system performance is not good enough for all the scenario conditions and it limits the incidence angle, thus not being possible to use this MLP design for the external feeds.

Conclusions:

- Small improvements with the CST optimization procedure => The CST optimization procedure is not a useful tool for the optimization of the MLP model.
- A MLP optimized for orthogonal incidence is not valid to be used for the external feeds => A MLP model optimized for the incidence angle of the external feeds must be designed. => In order to create a MLP that works for all the feeds it should be designed a meander-line pattern different for the different areas of incidence (see Figure 3.2.3.5) creating a smooth transition of the pattern in the areas' boundaries. Taking into account the frequency reuse scheme, the different areas of this MLP can not be in the ring disposition showed in Figure 3.2.3.5, they need to present a disposition similar to the cell distribution on the ground as shown in Figure 1.1.1.

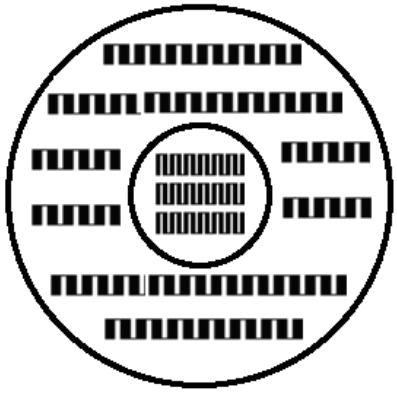

Figure 3.2.3.5. *Different sections MLP.*

3.3. Transmission line theory optimization

Taking into account the results exposed in section 3.2 for the CST optimization procedure, it was decided to design and develop a different optimization procedure. This second approach in the MLP optimization avoids the use of full wave analysis defining an equivalent circuit of the MLP structure which is easy to be optimized by numerical methods.

This section summarizes the work carried out on the second approach to optimize the MLP, i.e. using an equivalent circuit. Section 3.3.1 exposes the optimization procedure that it has been used. MLP dimensions have been optimized for the orthogonal incidence scenario in one model and they have been optimized for oblique incidence in a different model, sections 3.3.2 and 3.3.3 contains respectively the results given by the simulation of these two models.

3.3.1. **Procedure**

According to the theory studied in section 1.2.3.4, the incident electric filed is decomposed into a component parallel to the meander line axis and a component perpendicular to the meander-line axis. A single-layer meander line plane works differently for these two electric field components. For the parallel component of the electric field, the meander-line is equivalent to an inductive element, and for the perpendicular component of the electric field, the meander line is equivalent to a capacitive element. Due to the fact that the meander line responds differently to the above two mutually orthogonal field components, the associated transmitted field components will have two different phase shifts which together should imply a 90º phase difference between components. The objective of this procedure is to study the transmission characteristics of the polarizer and to design it controlling the phase difference between the two components.

Therefore, in order to model an equivalent circuit of the MLP two different circuits have to be designed, one with inductors for the parallel component and another one with capacitors for the perpendicular one. Each of these equivalent circuits will present as many sections as layers the MLP have; each section is a combination of the dielectric substrate with the meander-lines and the spacer, except for the last section that does not contain spacer. According to the transmission line theory the dielectric and the spacer can be modeled as transmission line sections and all the components can be interconnected in cascade. Figure 3.3.1.1 below depicts the conversion from the physical model to the equivalent circuit model.

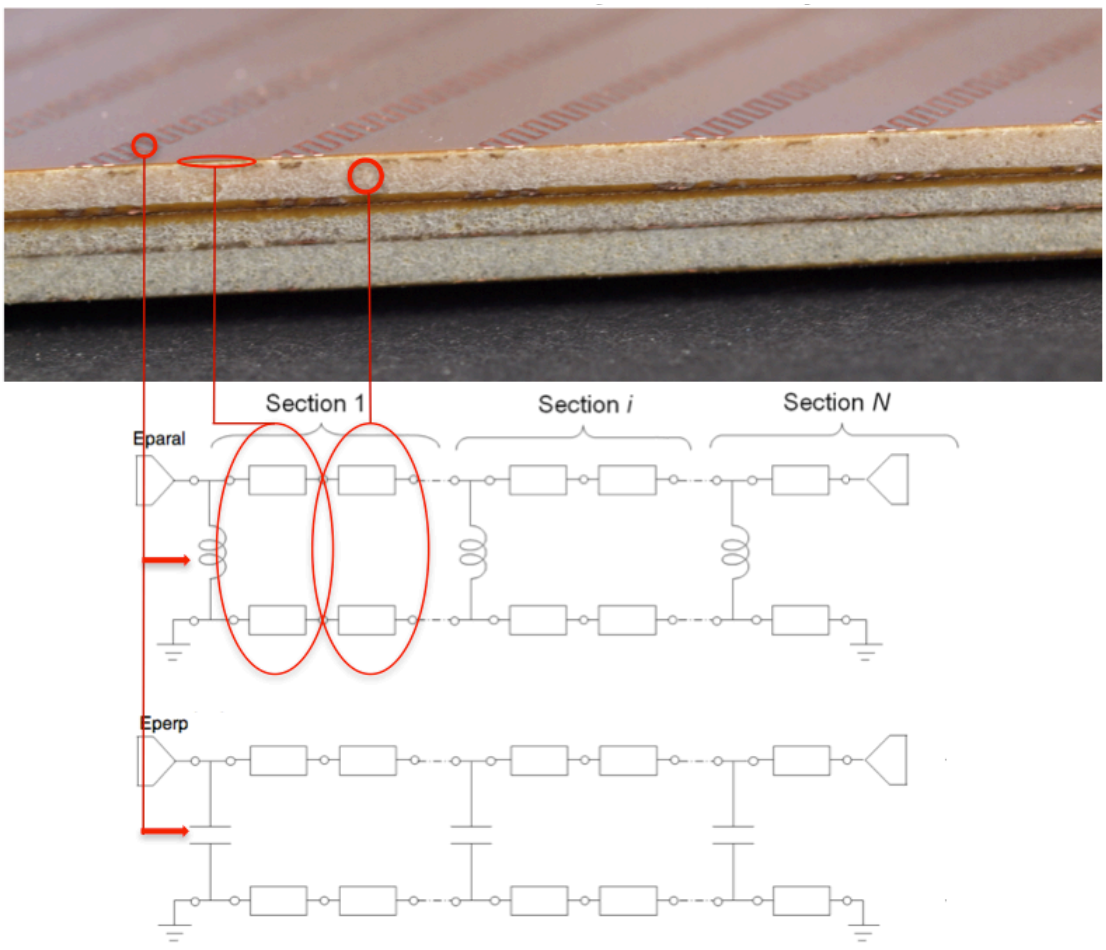

Figure 3.3.1.1 *Conversion from physical model to equivalent circuit model.*

In order to define the transmission line sections it is necessary to compute the impedance and the propagation constant for each section. Taking into account that the path followed by the wave depends on the incidence angle, these parameters are dependent of the incidence angle of each section, which according to the Snell's law will change in each discontinuity. The resulting parameters can be computed as follows for any incidence angle (θ) and for any frequency [31]:

$$\beta_{i,perp}{}^{(1)} = \beta_{i,paral}{}^{(1)} = k_i{}^{(1)} \cos\theta_i{}^{(1)} \quad (3.3.1.1)$$

$$\beta_{i,perp}{}^{(2)} = \beta_{i,paral}{}^{(2)} = k_i{}^{(2)} \cos\theta_i{}^{(2)} \quad (3.3.1.2)$$

$$Z_{i,perp}{}^{(1)} = \frac{\eta_0}{\sqrt{\varepsilon_{r_i}{}^{(1)}}} \frac{1-sin^2\theta_i{}^{(1)}}{\cos\theta_i{}^{(1)}} \quad (3.3.1.3)$$

$$Z_{i,perp}{}^{(2)} = \frac{\eta_0}{\sqrt{\varepsilon_{r_i}{}^{(2)}}} \frac{1-sin^2\theta_i{}^{(2)}}{\cos\theta_i{}^{(2)}} \quad (3.3.1.4)$$

$$Z_{i,paral}{}^{(1)} = \frac{\eta_0}{\sqrt{\varepsilon_{r_i}{}^{(1)}}} \frac{\cos\theta_i{}^{(1)}}{1-sin^2\theta_i{}^{(1)}} \quad (3.3.1.5)$$

$$Z_{i,paral}{}^{(2)} = \frac{\eta_0}{\sqrt{\varepsilon_{r_i}{}^{(2)}}} \frac{\cos\theta_i{}^{(2)}}{1-sin^2\theta_i{}^{(2)}} \quad (3.3.1.6)$$

where

η_0 is the vacuum impedance

ε_{r_i} is the dielectric constant of the i^{th} section.

The upper indexes (1) and (2) identify respectively the meander-line dielectric substrate and the spacer of each section.

$\sqrt{\varepsilon_{r_i}{}^{(2)}} \sin\theta_i{}^{(2)} = \sqrt{\varepsilon_{r_i}{}^{(1)}} \sin\theta_i{}^{(1)} = \sin\theta_{inc}$ according to the Snell's law. (3.3.1.7)

Taking into account the reciprocity of the device, the i^{th} section is the same as the $(N-i)^{th}$ one with i=0,1,…, (N/2) and this simplifies the analysis of the sections cascade, i.e. in the case of a four layers polarizer the two inner layers are identical and the two outer ones are identical but different than the inner ones.

These equivalent models have been implemented making use of Microwave Office (MWO) where each element is associated to its T-matrix and S-matrix and thus the complete equivalent circuit analysis can be easily computed by the software. Once the circuits are implemented on MWO it is possible to run its optimizer in order to obtain the ideal values of the lumped elements for a certain situation (i.e. for a certain incidence angle and frequency). According to the optimization procedure exposed in section 3.2, dielectric and spacer dimensions and electrical properties will remain fixed for the optimization in order to simplify this process. Therefore, the optimization process will have to act on four different variables: the capacitance of the inner layers, the inductance of the inner layers, the capacitance of the outer layers and the inductance of the outer.

On the other hand, the optimization goals have to be configured too. The final objective of the optimization process is to achieve a good circular polarization and low insertion loss for a certain incidence angle over the whole frequency band. But the real optimization goal needs to be defined in terms of the equivalent circuit properties. Therefore, the real optimization goals are:

- A phase difference of 90º between the resulting transmission coefficients of the two equivalent circuits for the whole frequency band (i.e. the phase difference between the outcoming parallel and perpendicular components of the electric field).
- Equal magnitude for the resulting transmission coefficients of the two equivalent circuits for the whole frequency band (i.e. equal magnitude for the outcoming parallel and perpendicular components of the electric field).
- A reflection coefficient equal to zero for the whole frequency band (i.e. no reflections). Weights have been used to relax this condition because the MLP presents low insertion loss and thus this condition should be automatically met.

MWO office optimization provides the ideal reactance values. However, this reactance's values needs to be converted into physical dimensions of the MLP in order to be able to prototype a model which presents such reactance's values. Unfortunately, MWO is not able to perform this conversion and thus it is necessary to use again full wave analysis.

In order to compute the impedance that a certain electric field component sees when it passes through a meander-line layer with a certain incidence angle, a meander-line unit cell has been modeled making use of Ansoft HFSS and its feature to use Floquet ports. As it can be see in Figure 3.3.1.2 the Floquet port uses an excitation with two components (a and b), which are respectively perpendicular and parallel to the meander-line axis, and it defines the propagation direction (blue vector). The meander-line unit cell is periodically repeated over the X and Y directions by defining periodic boundaries on the unit cell.

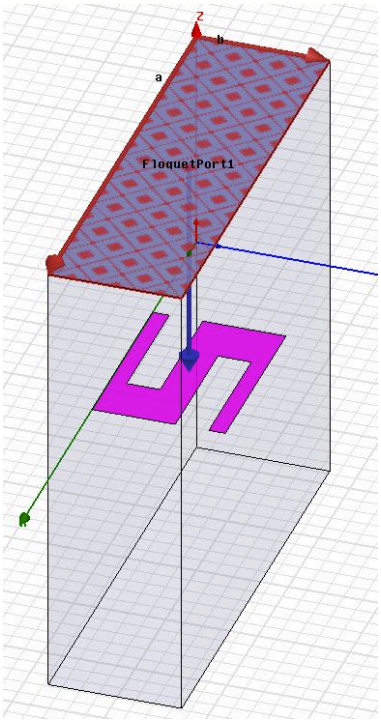

Figure 3.3.1.2. *HFSS unit cell model.*

Making use of this design, HFSS is able to compute the impedance that each excitation component sees when it passes through the periodic structure. These impedances values have to be equal to the reactance values computed during the MWO optimization. Therefore, once the meander-layer is designed on HFSS, it is possible to run its optimizer in order to obtain the dimensions which produce the desired impedances for a certain situation (i.e. for a certain incidence angle and frequency). According to the optimization procedure exposed in section 3.2, in order to simplify the process, the optimization will on the two more sensitive parameters: the meander-line spacing over the layer and the meander-line height. And the optimization goals are the seen impedances for each component of the excitation, i.e. the ideal reactance values.

The HFSS optimization will provide the ideal MLP dimensions for a certain frequency and incidence angle. Moreover, it is worth mentioning that, in contrast to the long simulation time using CST, both MWO and HFSS optimization processes can be computed in a few seconds.

3.3.2. Orthogonal incidence scenario

In this section analyzes the results given for a MLP optimized for orthogonal incidence using the transmission line theory optimization procedure exposed in last section. The MWO optimization process results in the values of inductances and capacitances of the equivalent circuits modeling the MLP which are summarized in Table 3.3.2.1. These values have been converted in their equivalent susceptances, which are the values that are used as goal in the HFSS optimization process, and Table 3.3.2.2 contains these values. Note that the inductances corresponds to the susceptances seen by the component of the electric field parallel to the meander-line axis, and the capacitances corresponds to the susceptances seen by the component of the electric field perpendicular to the meander-line axis.

	Outer layers	Inner Layers
L [H]	4,89E-09	3,78E-09
C [F]	3,52E-15	6,06E-15

Table 3.3.2.1. *Values of inductances and capacitances of the equivalent circuits. MWO optimization.*

	Outer layers	Inner Layers
B_{paral} **[siemens]**	-903,66	-698
B_{perp} **[siemens]**	1535,83	893

Table 3.3.2.2. *Susceptances values used as goal in HFSS optimization.*

Using the susceptances values from Table 3.3.2.2 as goal in the HFSS optimization, the MLP dimensions are varied in order to achieve these values. The result of this optimization process yields to the MLP dimensions shown in Table 3.3.2.3, where the meaning of each variable is defined by Figure 3.2.1.3.

	Outer [mm]	Inner [mm]
S	4.386	5.457
W	1.481	1.962
P	0.972	1.438
T1	0.194	0.349
T2	0.139	0.466

(a)

Td [mm]	0.1
Ts1 [mm]	1.866
Ts2 [mm]	1.555

(b)

Table 3.3.2.3. *MLP dimensions. (a) meander-line, (b) layers thickness*

Using HFSS it is possible to monitor the changes in the susceptances values that the variation of the meander dimensions produce during the optimization. Table 3.3.2.4 contains the final values that correspond to the susceptances values that the parallel and perpendicular components of the electric field see as they propagate through a MLP structure with the dimensions specified in Table 3.3.2.3. And their equivalent inductances and capacitances values for the equivalent circuits are shown in Table 3.3.2.5 below.

	Outer layers	**Inner Layers**
B_{paral} **[siemens]**	-904	-695
B_{perp} **[siemens]**	1539	896

Table 3.3.2.4. *Susceptances values given by the HFSS optimization*

	Outer layers	**Inner Layers**
L [H]	4,89E-09	3,76E-09
C [F]	3,52E-15	6,04E-15

Table 3.3.2.5. *Values of inductances and capacitances of the equivalent circuits.*

As it can be seen from the comparison of Tables 3.3.2.2 and 3.3.2.4, the HFSS optimization process is able to optimize the meander dimensions to produce susceptances values close to the ideal values given by the MWO optimization. Furthermore, from the comparison of Tables 3.3.2.1 and 3.3.2.5, it can be appreciated that the difference in terms of the inductance and capacitances values of the equivalent circuits is even smaller.

However, although the difference between the ideal values resulting from the MWO optimization and the real values resulting from the HFSS optimization is small (they are called real because they are the values that actually correspond to meanders' physical dimensions), it is necessary to check the effect that this small difference produce in the system behavior. Therefore, it has been decided to feedback MWO with the real susceptances values given by HFSS in order to analyze the equivalent circuits with these real values and thus check the differences between the ideal and the real results. Figure 3.3.2.1 below shows the results given for a MLP optimized for orthogonal incidence: (a) phase difference for the ideal reactance values, (b) magnitude difference for the ideal values, (c) phase difference for the real values, (d) magnitude difference for the real values.

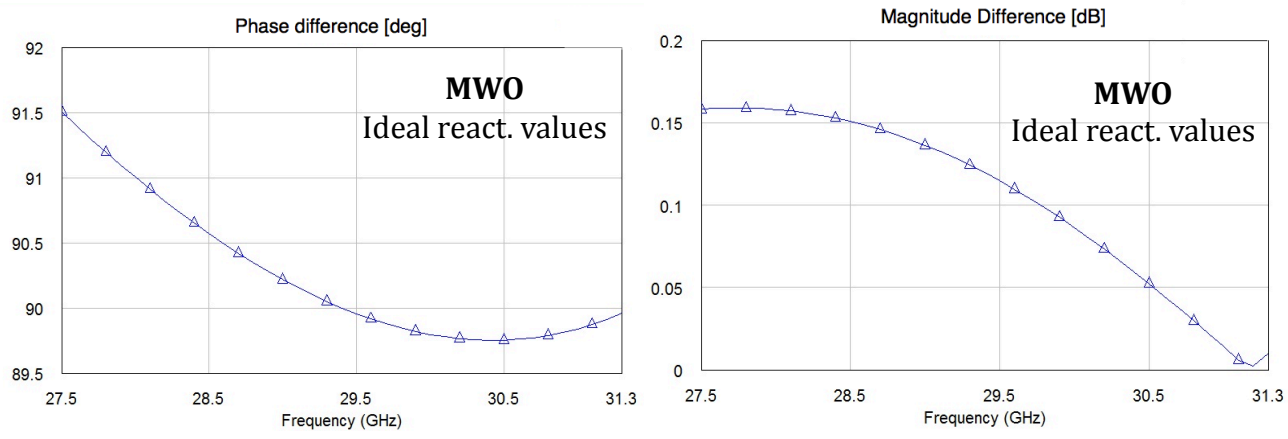

(a) (b)

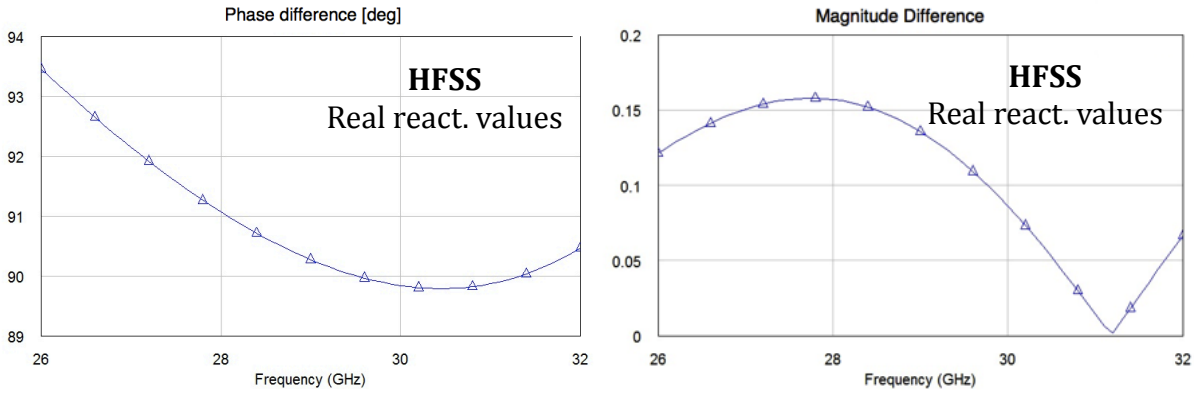

(c) (d)

Figure 3.3.2.1 *Results comparison between ideal and real values for orthogonal incidence.*

As it can be deduced from Figure 3.3.2.1 the transmission line theory optimization procedure produces a MLP model which is able to provide a good circular polarization under this scenario conditions because the phase difference between the electric field components is close to 90º and the phase difference is almost zero, both over the whole frequency band. Moreover, when results for ideal and real reactance values are compared, it can be seen how the difference between them is very small and thus it can be concluded that the MLP dimensions given by the HFSS optimization produce a good circular polarization in the case of orthogonal incidence.

Eventually, it can be checked the improvement of the new optimized MLP model over the models designed and prototyped during the CST optimization process exposed in section 3.2. In order to perform this comparison, it has been decided to model the new MLP on CST Microwave Studio (and thus this model could be used to design prototyping masks following the procedure exposed in section 3.2.2) and simulate the whole antenna system in the same way as it was done for the simulations studied in section 3.2.1. Following Figure 3.3.2.2 shows the performance comparison between the the rescaled version of the Leo Young's original model [26] (green dotted line), the model optimized using CST (blue dotted line) and the model optimized using the transmission line theory procedure (red dotted line). This Figure has been obtained processing CST simulations results with the same Matlab script as the one used in section 3.2.3.

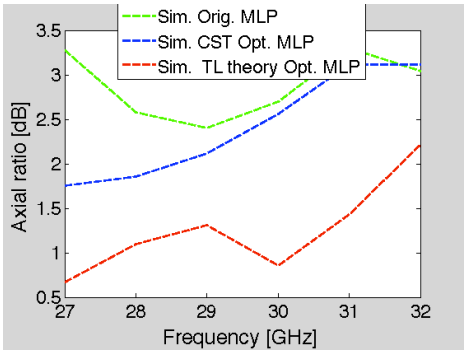

Figure 3.3.2.2. *CST simulations results comparison for the different optimization procedures.*

As it was explained in section 3.2.3, CST results are not able to describe the exact response of the system but can be used to have an idea of the improvements that an optimization reports. From Figure 3.2.2 it can be concluded that the transmission line theory optimization procedure not only deliver the results faster but also provides better results.

3.3.3. **Oblique incidence scenario**

In this section analyzes the results given for a MLP optimized for oblique incidence using the transmission line theory optimization procedure exposed in last section modified to include the effect of having a non-perpendicular incidence angle.

Taking into account the Snell's Law, it can be deduced that having a certain incidence angle different from zero in the surface of the MLP, the incidence angle will change from layer to layer as it has been considered in equations from 3.3.1.1 to 3.3.1.6 according to equation 3.3.1.7. Moreover, taking into account that the conditions are the same for the two inner layers (the wave comes from the spacer of last section and passes through the meander-line, the dielectric and the spacer of the current section) but different between the two outer ones (in the first outer layer the wave comes from air but in the second outer layer the wave comes from last section), it can be concluded that the incidence angle is the same for the two inner layers but different for the two outer layers. Therefore, this effect has been included in the optimization process and thus inductances, capacitances, susceptances and dimensions values used during the optimization process are different for the first and the last outer layers.

The MWO optimization process results in the values of inductances and capacitances of the equivalent circuits modeling the MLP which are summarized in Table 3.3.3.1. These values have been converted in their equivalent susceptances, which are the values that are used as goal in the HFSS optimization process, and Table 3.3.3.2 contains these values. Note that the inductances corresponds to the susceptances seen by the component of the electric field parallel to the meander-line axis, and the capacitances corresponds to the susceptances seen by the component of the electric field perpendicular to the meander-line axis.

	1st Outer layer	**Inner Layers**	**2nd Outer layer**
L [H]	7,83E-09	2,46E-09	6,96E-09
C [F]	5,04E-15	3,01E-15	5,03E-15

Table 3.3.3.1. *Values of inductances and capacitances of the equivalent circuits. MWO optimization.*

	1st Outer layer	**Inner Layers**	**2nd Outer layer**
$\boldsymbol{B_{paral}}$ **[siemens]**	-1445,85	-454,02	-1285,12
$\boldsymbol{B_{perp}}$ **[siemens]**	1074,92	1799,97	1076,05

Table 3.3.3.2. *Susceptances values used as goal in HFSS optimization.*

Using the susceptances values from Table 3.3.3.2 as goal in the HFSS optimization, the MLP dimensions are varied in order to achieve these values. The result of this optimization process yields to the MLP dimensions shown in Table 3.3.3.3, where the meaning of each variable is defined by Figure 3.2.1.3.

	Outer 1 [mm]	Inner [mm]	Outer 2 [mm]
S	6,97	5.329	6.078
W	1.715	1.351	1.715
P	0.972	1.438	0.972
T1	0.194	0.349	0.194
T2	0.139	0.466	0.139

(a)

Td [mm]	0.1
Ts1 [mm]	1.866
Ts2 [mm]	1.555

(b)

Table 3.3.3.3. *MLP dimensions. (a) meander-line, (b) layers thickness*

Using HFSS it is possible to monitor the changes in the susceptances values that the variation of the meander dimensions produce during the optimization. Table 3.3.3.4 contains the final values that correspond to the susceptances values that the parallel and perpendicular components of the electric field see as they propagate through a MLP structure with the dimensions specified in Table 3.3.3.3. And their equivalent inductances and capacitances values for the equivalent circuits are shown in Table 3.3.3.5 below.

	1st Outer layer	Inner Layers	2nd Outer layer
Bparal [siemens]	-1394,94	-464	-1349,93
Bperp [siemens]	1162,91	1698	1089,05

Table 3.3.3.4. *Susceptances values given by the HFSS optimization*

	1st Outer layer	Inner Layers	2nd Outer layer
L [H]	7,55E-09	2,51E-09	7,31E-09
C [F]	4,01E-15	3,82E-15	5,33E-15

Table 3.3.2.5. *Values of inductances and capacitances of the equivalent circuits.*

As it can be seen from the comparison of Tables 3.3.3.2 and 3.3.3.4, the HFSS optimization process is able to optimize the meander dimensions to produce susceptances values close to the ideal values given by the MWO optimization. Furthermore, from the comparison of Tables 3.3.3.1 and 3.3.3.5, it can be appreciated that the difference in terms of the inductance and capacitances values of the equivalent circuits is even smaller.

However, although the difference between the ideal values resulting from the MWO optimization and the real values resulting from the HFSS optimization is not very big, it is necessary to check the effect that this difference produce in the system behavior. Therefore, following the same procedure as the one shown in section 3.3.2, it has been decided to check the differences between the ideal and the real results making use of MWO analysis of the equivalent circuits. Figure 3.3.3.1 below shows the results given for a MLP optimized for oblique incidence: (a) phase difference for the ideal reactance values, (b) magnitude difference for the ideal values, (c) phase difference for the real values, (d) magnitude difference for the real values.

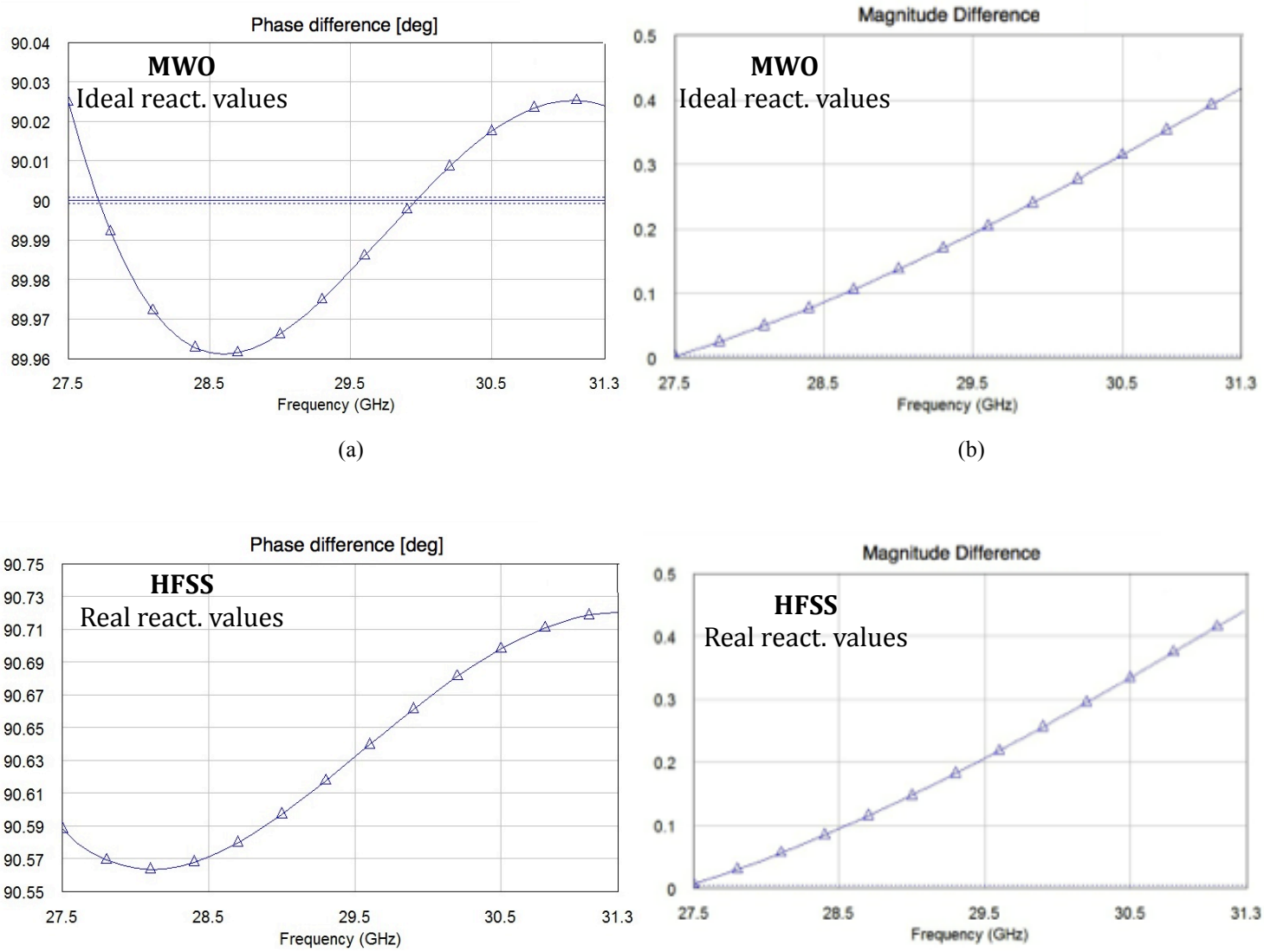

Figure 3.3.3.1 *Results comparison between ideal and real values for orthogonal incidence.*

As it can be deduced from Figure 3.3.3.1 the transmission line theory optimization procedure produces a MLP model which is able to provide a good circular polarization under this scenario conditions because the phase difference between the electric field components is close to 90º and the phase difference is almost zero, both over the whole frequency band. Moreover, when results for ideal and real reactance values are compared, it can be seen how the difference between them is very small and thus it can be concluded that the MLP dimensions given by the HFSS optimization produce a good circular polarization in the case of oblique incidence.

Therefore, making use of the MLP model optimized for orthogonal incidence and the MLP model optimized for oblique incidence it is possible to manufacture MLP that works for all the feeds by using a meander-line pattern different for the different areas of incidence and creating a smooth transition of the pattern in the areas' boundaries, as it has been depicted in Figure 3.2.3.5.

4. Feeds coupling

In section 1.2.4, where the influence of adjacent feeds was analyzed for the model that includes seven feeds plus lens, it was shown in Figure 1.2.4.5 how the coupling between adjacent feeds is lower than -32 dB within the working frequency band. Nevertheless, in a mobile communications scenario were a feed tries to receive a very weak signal coming from the ground while a small part of the energy ($s_{21} \leq -32dB$) coming from adjacent feeds is also received, the weak signal could remain embedded in the signal coming from adjacent feeds and thus not being possible to process the ground signal.

Therefore, although this topic was not initially considered in the project's scope, this section contains the analysis of the problem in the real scenario (where the system is composed out of feeds, lens and MLP), the analysis a proposed technique to overcome the problem and, based on the conclusions extracted for this technique, new techniques to reduce the coupling are proposed. Section 4.1 characterizes the feeds coupling problem, section 4.2 expose a possible solution and section 4.3 analyze the measurements obtained to check the validity of the proposed technique and propose different techniques.

4.1. Problem characterization

In order to characterize and understand the behavior of the feeds coupling, the transmitting system was mounted including the MLP, the lens and two feeds in the positions of two external feeds (according to the scenario specifications given in section 1.1). This system was connected to a network analyzer capable to perform measurements on the Ka-band, see Figure 4.1.1 below.

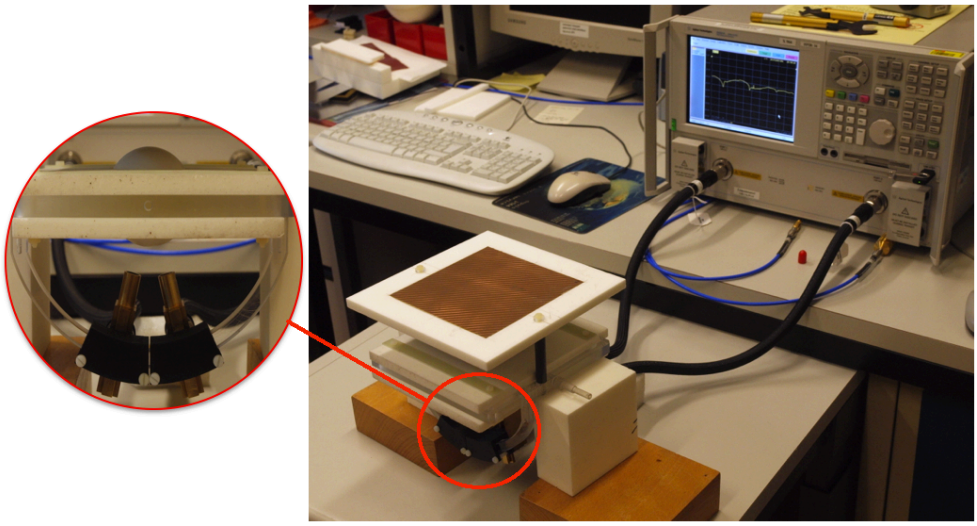

Figure 4.1.1. *System setup for the feeds coupling characterization.*

Using the network analyzer, one of the feeds is set as transmitter (port 3, according to Figure 1.2.4.4) and the other as receiver (port 2) in order to measure the amount of energy going from one port to the other over the working frequency band, i.e. S_{23}(f). The network analyzer stores the result in a file format that can be later read and processed. Therefore, a Matlab script has been developed to process the data from this file and plot the resulting measurement over the whole frequency band. This plot is included in Figure 4.3.1 and it will be analyzed in section 4.3 together with the measurements taken from the application of a technique to reduce the coupling.

4.2. Possible solutions

Taking into account results studied in section 2.2.1, where it was tried to compensate the ellipticity effect on the external cells by introducing an offset in the feeds positions with respect to the lens center, it can be concluded that using the correct offset it is also possible to achieve the cell distribution on the ground given by the scenario specifications positioning all the feeds parallel to each other.

The two possible feeds positions to achieve the same disposition of the cells on the ground can be seen in Figure 4.2.1 below, where it is reasonable to think that the parallel distribution of the feeds should lead to a lower coupling because the oblique distribution implies that the feeds apertures are faced with certain angle and thus it should be easier to the energy to flow from one port to the other.

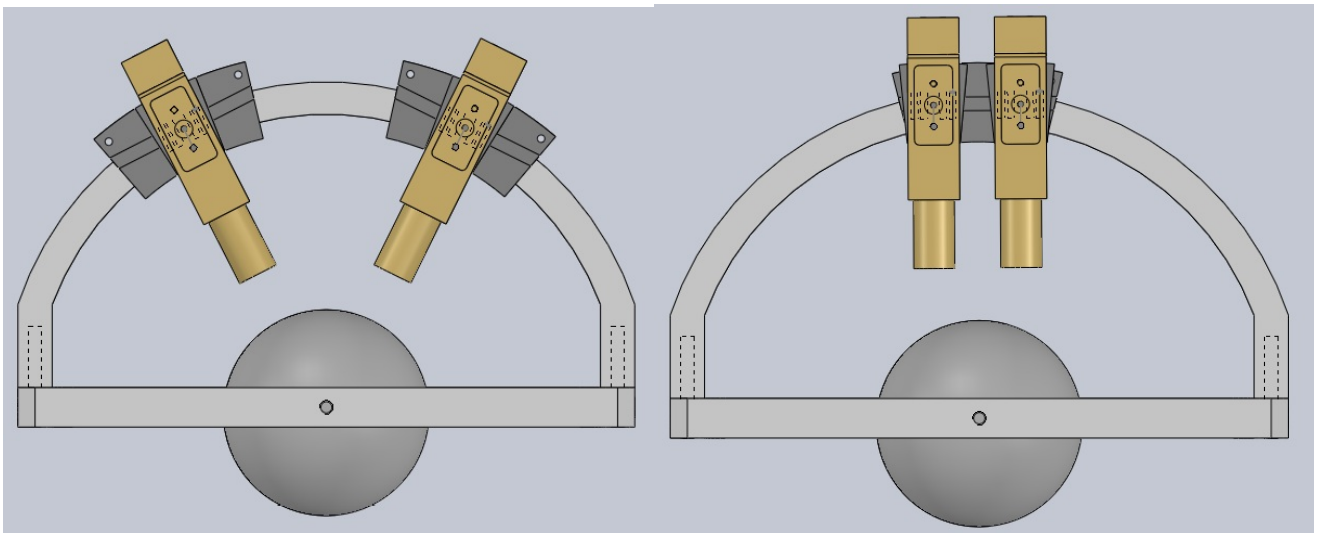

(a) (b)

Figure 4.2.1. *Possible feeds positions for the external cells. (a) oblique and (parallel) distribution*

These two different feeds dispositions were mounted and connected to the network analyzer as it has been explained in section 4.1. The results were stored in a file and later processed by the Matlab script code developed in section 4.1. Next section will expose these measurements comparing them and extracting conclusions about the feeds coupling from them.

4.3. Measurements & conclusions

Using the feeds dispositions exposed in section 4.2 (see Figure 4.2.1), it has been measured in the network analyzer the amount of energy going from one port to the other over the working frequency band, i.e. S_{23}(f). Processing the results with a Matlab scripts the results have been plotted together in Figure 4.3.1, where the blue line gives the measurements for the oblique disposition scenario and the red line gives the measurements for the parallel disposition scenario.

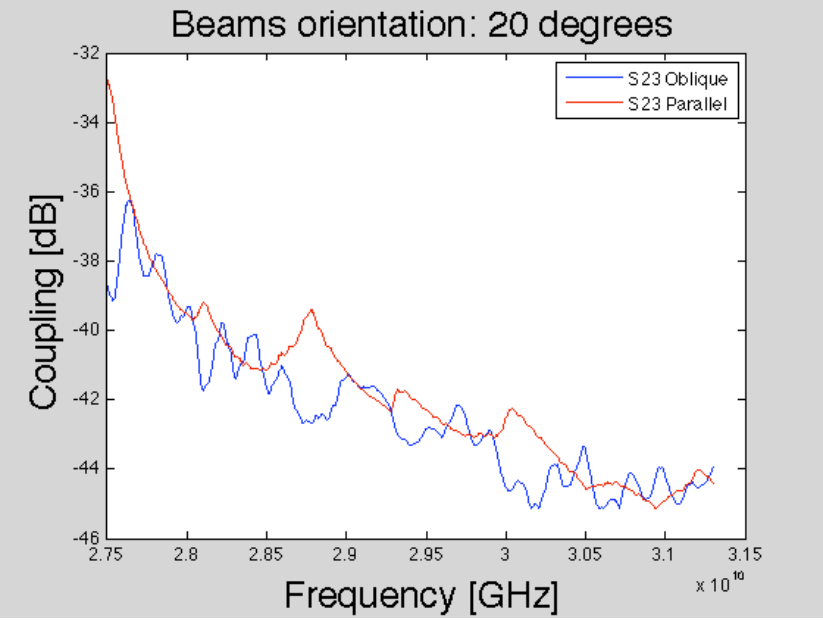

Figure 4.3.1. *Feeds couling.*

As it can be observed in Figure 4.3.1, feeds couplings could be considered equal for both feeds dispositions and again they are lower than -32 dB for the whole frequency band. Comparing these two results with the results given in the scenario where the transmitting system is composed by feeds, internal polarizers and lens (see Figure 1.2.4.5); and checking how S_{23}(f) is not bigger in presence of the MLP, it can be concluded that the use of MLP does not imply more reflections (remember that one of its characteristics is low insertion losses). Moreover, due to the fact that both curves are so similar, it can be concluded that coupling is not due to the feeds facing but to the reflections on the lens surface. In fact, it can be appreciated in Figure 4.3.1 how S_{23}(f) presents the behavior of a standing wave.

Tacking into account the conclusion that the coupling is due to reflections on the lens surface, two different techniques to reduce the coupling even more are proposed:

- **Luneburg lens**. As it has been introduced in section 1.2.2.2, the Luneberg lens is able to produce with a reasonable number of shells a smooth change in the permittivity that the wave sees when it passes through the lens and thus the reflections on its surface are reduced.

- **Frequency reuse scheme**. By the correct choice of the frequency used by each feed (see Figure 1.1.1), the feeds coupling can be reduced applying frequency filtering in the receiving system associated to each feed.

5. Summary & Future work

This project analyzes a multi-beam antenna system for HAPS applications. Different models have been studied to achieve the correct multi-beam radiation pattern:

- Printed array
- Helix array
- Circular waveguide feeds in combination with a spherical lens

The model chosen for the final antenna system is the waveguide feeds solution because it is able to handle big power and provides independency between feeds.

Moreover, in order to achieve circular polarization different polarizer models have been studied:

- Internal elliptical sections polarizer
- Internal septum polarizer
- External MLP

The polarizer chosen for the final antenna system is the external MLP solution because it provides a very good circular polarization preventing from the circular polarization degradation that the lens introduces.

The final antenna system has been analyzed and several potential problems have been identified and different solutions have been explored for each of them:

1. Ellipticity effect on external cells. Possible solutions:
   a. Acting on feeds position (feed's tilt and offset) => Not valid
   b. Acting on the radiators => Valid => Future work:
      i. Acting on lens shape. Create a lens shape which satisfies the requirements for the different feeds positions.

      ii. Acting on the feed. Different modifications in the feed's horn or waveguide should be analyzed.

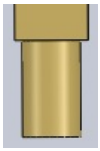

2. Axial ratio degradation on the external cells. Possible solutions:
   a. CST optimization => Not valid
   b. Transmission line theory optimization => Valid => Different MLP have been designed for different incidence angles. => Future work:
      i. Different sections polarizer, where is section is optimized for certain incidence angle and frequency.

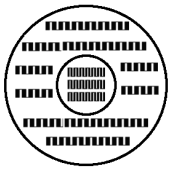

3. Feeds coupling.
   a. Conclusion: the coupling is due to reflections on the lens surface.
   b. Future work => possible solutions:
      i. Luneburg lens
      ii. Filtering

During the development of the project wide experience has been acquired in the use the following software tools:

- CST Microwave office. 3D full-wave electromagnetic field software tool used to simulate the antenna system.

- SolidWorks. 3D mechanical CAD tool used to design the plastic feed's holders and the mask for the meander-line layers.

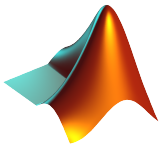

- Matlab. Mathematical software used to characterize the ellipticity effect problem and to process both measurements and simulations results.

- AWR Microwave Office. RF/microwave design software used to implement the equivalent circuits and optimize them for certain incidence angle and frequency according to the transmission line theory optimization procedure.

- Ansoft HFSS. 3D full-wave electromagnetic field software tool used for the optimization of MLP's dimensions according to the transmission line theory optimization procedure.

Finally, it could be interesting to highlight that during the development of the project wide experience has been acquired in the use the following hardware tools and prototyping techniques:

- 3D plastic laser printer.
- Photoetching process.
- Microwave generator.
- Spectrum analyzer.
- Network analyzer.
- Anechoic chamber.

6. Appendix

6.1. References

[1] J. Gavan, S. Tapuchi and D. Grace, "Concepts and Main Applications of High-Altitude-Platform Radio Relays," *Radio Science Bulletin,* NO. 330, September 2009.

[2] J. Thornton, D. Grace, M. H. Capstick and T. C. Tozer, "Optimising an Array of Antennas for Cellular Coverage from a High Altitude Platform," *IEEE Transactions on Wireless Communications,* 2, 3, 2003, pp. 484-492.

[3] "Technical and operational characteristics for the fixed service using high altitude platforms stations in the band 27.5-28.35 GHz and 31-31.3 GHz", Recommendation ITU-R F.1569, ITU.

[4] M. Letizia, B. Fuchs, A. Skrivervik, J. R. Mosig. *"Circularly polarized homogeneous lens antenna system providing multi-beam radiation pattern for HAPS"*. March 2010, Radio Science Bulletin.

[5] Marco Letizia, Jean-François Zürcher, Benjamin Fuchs, Juan Ramon Mosig, Anja Skrivervik. *"Circularly polarized multi-beam lens antenna system for High Altitude Platforms (HAPS)"*. EUCAP 2011.

[6] T. C. Tozer and D. Grace, "High-altitude platforms for wireless communications," *IEE Electronics and Communications Engineering Journal,* **13**, June 2001, pp. 127-137.

[7] J. Thornton, "Properties of Spherical Lens Antennas for High Altitude Platform Communications," *6th European Workshop on Mobile/Personal Satcoms & 2nd Advanced Satellite Mobile Systems (EMPS & ASMS),* 21-22 Sept. 2004. ESTEC, European Space Agency.

[8] J. Thornton, D. Grace, C. Spillard, T. Konefal and T. C. Tozer, "Broadband communications from a high altitude platform - The European HeliNet programme," *IEE Electronic Communication Engeneer Journal,* **13**, June 2001, pp. 138-144.

[9] M. A. Mitchell, J. R. Sanford, L. E. Corey, R. A. Moore and V. P. Pusateri, "A multiple-beam multiple-frequency spherical lens antenna system providing hemispherical coverage," *ICAP 89,* 1989, pp. 394-398.

[10] J. Thornton, "Antenna Technologies for Communications Services from Stratospheric Platforms," *4th International Airship Convention and Exhibition, Cambridge*, UK, July 2002.

[11] S. K. Rao, "Design and analysis of multiple-beam reflector antennas," *IEEE Transactions on Antennas and Propagation,* AP-41, 4, 1999, pp.53-54.

[12] FP6-IST-2003-506745 CAPANINA: *"Report on steerble antenna architectures and critical RF circuites performance"*, Deliverable Number D24.

[13] Bernhard H. Walke: *"Mobile Radio Networks"*, Wiley, 1999.

[14] Constantine A. Balanis: *"Antenna Theory, Analysis and Design"*, New York, Jhon Wiley and Sons, 2005.

[15] R. J. Mailloux: *"Phased Antenna Array Handbook"*, Boston: Hartech House,2nd.Ed, pp. 24.

[16] J.M.Tranquiila: *"A Study of the Quadri_lar Helix Antenna for Globale Positioning System (GPS) Applications"*, IEEE Trans. on Antennas and Propagation,vol. 38, No. 10, October 1990.

[17] B. Schoenlinner: *"Wide-Scan Spherical-Lens Antennas for Automotive Radars"* IEEE Transactions on Microwave Theory and Techniques, vol. 50,no. 9, pp. 2166-2175, 2002.

[18] E.F. Buckley: *"Microwave Optics"*, Academic Press, London, England.

[19] Richard C. Johnson: *"Antenna Engineering Handbook"*, Georgia Institute of Technology Atlanta, McGraw-Hill, 3rd edition, 1993.

[20] G. Bertin, L. Accatino and M. Mongiardo,: *"Full-Wave Design and Opti mization of Circular Waveguide Polarizers With Elliptical Irises"*, IEEE Trans.Microwave Theory Tech., vol. 50, No. 4, Apr 2002.
[21] J. Bornemann and V. A. Labay: *"Ridge waveguide polarizer with _nite and stepped-thickness septum,"* IEEE Trans. Microwave Theory Tech., vol. MTT-43, p. 1782-1787(1995).
[22] J. Esteban and J. M. Rebollar: *"Field theory CAD of septum OMT-polarizers,"* in IEEE AP-S Symp. Dig., p. 2146-2149(1992).
[23] S.W. Wang, C.-H. Chien, Chun-Long Wang, : *"A circular polarizer designed with a dielectric septum loading,"* IEEE Trans. Microwave Theory Tech., vol. 52, p. 1719-1723(2004).
[24] T. Zhang and Z. Yan, *"A Ka Dual-Band Circular Waveguide polarizer"*, National Laboratory of Antennas and Microwave Technology, Xidian University, Xi'an, 710071, P. R. China.
[25] D. S. Lerner: *"A wave polarization converter for circular polarization"*, Antennas and Propagation Society International Symposium, pp. 65-69, 1963.
[26] L. Young, L. A. Robinson, and C. A. Hacking, *"Meander-line polarizer"*, IEEE Trans. Antennas Propagat., vol. AP-21, pp. 376-378, May 1973.
[27] Burger, H. A. and A. Division: *"A dual polarized antenna system using a meanderline polarizer,"* IEEE Antennas Propag. Soc. Int. Symp. Dig., Vol. 16, 55–58, 1978.
[28] Wu, T. K.: *"Meander-line polarizer for arbitrary rotation of linear polarization"*, IEEE Microwave Guided Wave Lett., Vol. 4, No. 6, 199–201, 1994.
[29] J.-C. Zhang, Y.-Z. Yin, and J.-P. Ma: *"Multifunctional meander line polarizer"*, Progress In Electromagnetics Research Letters, Vol. 6, 55–60, 2009
[30] Russell A. Burleeon: *"A study of two dimensional tapered periodic edge treatments to reduce wideband edge diffraction"*, USAF, 1993.
[31] Ruey-Shi Chu and Kuan-Min Lee: *"Analytical Model of a Multilayered Meander-Line Polarizer Plate with Normal and Oblique Plane-Wave Incidence"*, IEEE Transactions on antennas and propagation, VOL. AP-35, NO. 6, June 1987
[32] C. Terret, J. R. Levrel, and K. Mahdjoubi: *"Susceptance Computation of a Meander-Line Polarizer Layer"*, IEEE Transactions on antennas and propagation, vol. ap-32, no. 9, September 1984
[33] R. F. Harrington: *"Field Computation by Moment Methods"*. New York: IEEE Press, second ed., 1993.
[34] Walton C. Gibson: *"The method of moments in electromagnetics"*, Boca Raton, Chapman & Hall, 2008.
[35] M. G. Floquet: *"Sur les équations différentielles linéaires a coefficient périodiques"*, Annales scientifiques de l'É.S.N. 2e série, tome 12, pp. 47-88, 1983.
[36] L.W. Henderson, *"Introduction to PMM"*, Tech. Rept. 715582-5, OSU ESL, Dept. of Electrical Eng., prepared for Wright-Patterson Air Force Base, OH, February 1986

1.1. Annex 1: EUCAP 2012 conference publication abstract

Circularly polarized multi-beam lens antenna system. Comparison between 2 polarizers.

Marco Letizia, Jean-François Zürcher, Benjamin Fuchs, Juan Ramon Mosig
Laboratory of Electromagnetics and Acoustics (LEMA) Ecole Polytechique Fédérale de Lausanne (EPFL)
Lausanne, Switzerland
marco.letizia@epfl.ch

Carlos Zorraquino Gastón
Universidad Carlos III de Madrid
Madrid, Spain

Abstract—**Two Ka-Band circularly polarized multi-beam antenna systems are compared. The antenna system is composed of a dielectric lens fed by circular waveguides terminated with small horns. The circular polarization is achieved either by integrating a polarizer in the waveguide feed or positioning a meander-line polarizer at the outer of the lens. An analytical model to design meander-line polarizers is proposed. The two antenna systems have been analyzed, realized, measured and compared. For both systems, an axial ratio lower than 3 dB is achieved within a bandwidth of 19%.**

Keywords: multi-beam antenna, circular polarization, polarizer, lens antenna.

I. Introduction

Many applications such as satellite communications and radar systems require the use of high gain circularly polarized multi-beam antennas. The multi-beam feature allows indeed to increase the capacity of the communication channel (via frequency reuse for instance) and to provide beam switching capabilities [1]. The use of circular polarization waveforms is a smart solution to both overcome the problems of alignment between transmitter and receiver and to mitigate the effects of undesired reflections. To radiate multiple beams with high gain in Ka-band, a dielectric lens fed by several feeds is used [2].

This paper focuses on the way to generate circularly polarized beams. For that purpose, two solutions are investigated and compared both numerically and experimentally.

II. Polarizer Design Procedures

Two solutions, represented in Fig.1, are described to generate circularly polarized beam.

A. Internal dielectric based Polarizer

The first solution (Fig. 1.a) implies the use of a dielectric septum polarizer mounted inside the feed. Details about the design of this polarizer are given in [2]. According to this strategy, each primary radiator is circularly polarized and the lens focuses the beam to achieve the needed radiation pattern.

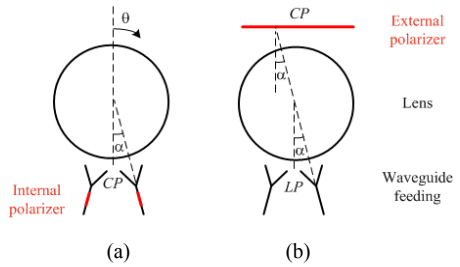

Figure 1. Dielectric lens illuminated by waveguide feeds: (a) the polarizer is inside the feed; the wave propagating in the lens is circularly polarized (b) the polarizer is mounted in the outer of the lens; the wave propagating in the lens is linearly polarized.

B. External Meander-line Polarizer

The second solution (Fig. 1.b) is composed of an external meander-line based polarizer that acts on the linearly polarized wave going out of the lens. The feed illuminates the lens with a linearly polarized wave and the external polarizer provides circular polarized beams.

The design of a meander polarizer in Ka-Band represents a challenge when its behavior needs to be predicted by full wave analysis software. Indeed, modeling the meander lines requires a high number of mesh cells and an eventual optimization of the structure becomes unfeasible. To overcome those problems an analytical model based on transmission line theory has been developed. The method is based on the combination of transmission lines theory and unit cells analysis of the single meander. Such analytical model will be fully discussed in the final paper.

III. Prototype Characterization.

A. Description of the prototypes and the measurement setups

The primary sources, the dielectric polarizer and the Teflon lens (shown in Fig. 2) have been realized by milling machine techniques with a nominal tolerance of 50 μm. The dielectric slab polarizer is inside the waveguide as represented in Fig. 2(a).

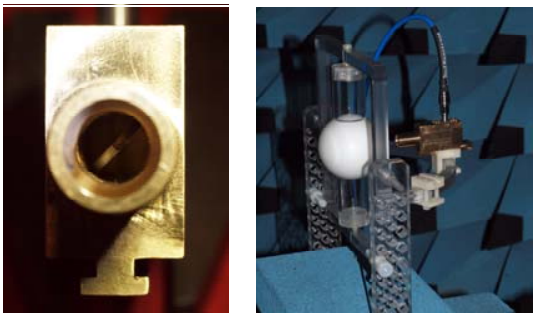

(a) (b)

Figure 2. Dielectric lens illuminated by a waveguide feed: (a) the polarizer is mounted inside the feed; (b) antenna in anechoic chamber.

The external polarizer has been realized by chemically etching the meander lines on Kepton substrate (ε_r= 3.2). Spacer made by Rohacell (ε_r= 1.07) is used to outdistance those substrates. Figure 3(b) shows the measurement setup where the external polarizer is mounted at the outer of the lens.

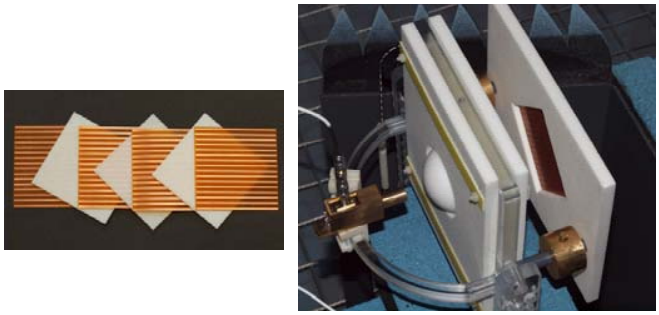

(a) (b)

Figure 3. (a) Prototype of meander line polarizer. (b) measurement setup with polarizer mounted outer of the lens.

The scattering parameters of the two prototypes have been evaluated by the vector analyzer (Agilent Technologies E8361A). Tests in anechoic chamber have been performed to characterize the radiation pattern and the Axial Ratio (AR).

B. Measurement results

The two antenna systems show a bandwidth of 19% (26.8-32.5 GHz). The half-power-beam-width of both antennas is 11.8° and the side lobe level is lower than -15°, as expected from simulations. The Axial Ratio (AR) has been measured using the spinning dipole method for different frequencies (between 27 and 32.5 GHz) and for different angles α (represented in Fig. 1) between 0° and 30°. The measured AR is plotted at 29 GHz for both antenna systems.

With the internal polarizer, the AR is lower than 3 dB in the broadside direction (α=0°) for all measured frequencies. Moreover, it remains acceptable within the range -10°<θ<10°. For symmetry reasons, the radiation performances of this antenna do not depend on α.

With the external polarizer, the AR is lower than 2 dB in the broadside direction (α=0°) and it remains acceptable within the range -12°<θ<12°. However, the AR degrades, when α increases and it is higher than 3 dB for $|\alpha|$>10°.

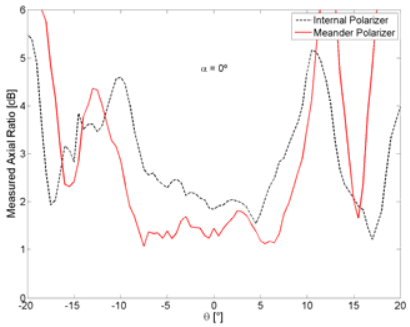

(a)

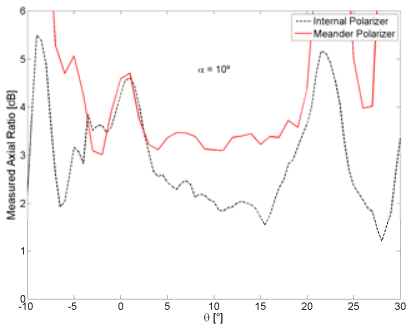

(b)

Figure 4. Axial ratio measured at 29 GHz. Comparison between internal septum and external meander polarizer for two different incident angle α. (a) α=0°. (b) α=10°.

IV. CONCLUSION

The way to generate multiple beams with a circular polarization in Ka-band has been investigated. The antenna system is composed of a homogeneous Teflon lens fed by waveguide horns. To synthesize the circular polarization, two strategies have been proposed and compared both numerically and experimentally. On the one hand, an internal polarizer is placed inside the feeds. Although the quality of the circular polarization is deteriorated by the lens, all beams have the same axial ratio. On the other hand, an external meander-line based polarizer is placed at the outer of the lens. The synthesized polarization is very good for the broadside beam and degrades when the beam angle increases.

REFERENCES

[1] A.L. Peebles, "A Dielectric Bifocal Lens for Multibeam Antenna Applications," *IEEE Antennas and Propagation*, vol. 36, 1988, pp. 599-606.

[2] M. Letizia, B. Fuchs, A. Skrivervik, J.R. Mosig, "Circularly Polarized Lens Antenna System Providing Multibeam Radiation Pattern for HAPS", Radio Science Bulletin, March 2010.

1.2. Annex 2: Feeds' positioners mechanical draws

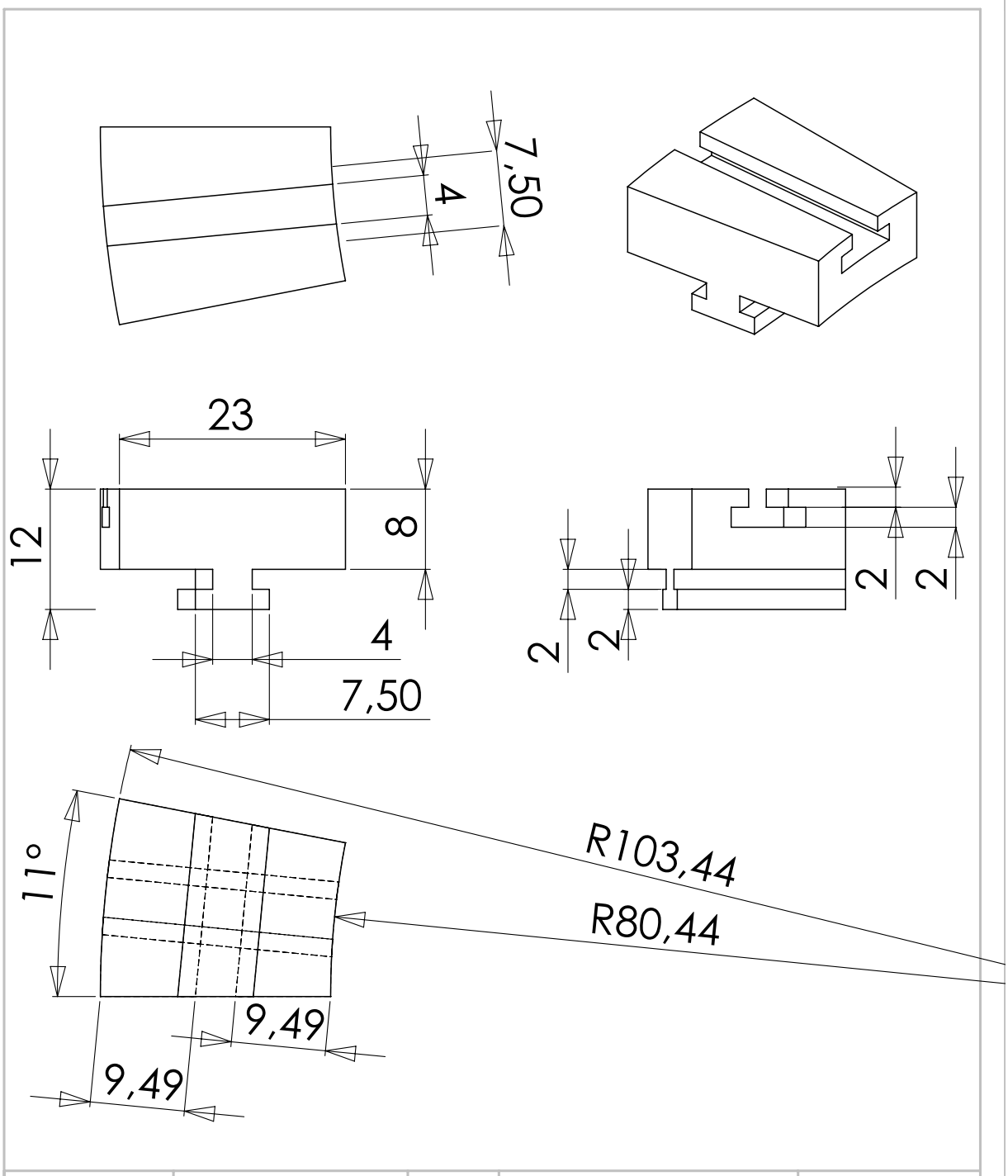

SI NO SE INDICA LO CONTRARIO: LAS COTAS SE EXPRESAN EN MM ACABADO SUPERFICIAL: TOLERANCIAS: LINEAL: ANGULAR:	ACABADO:	REBARBAR Y ROMPER ARISTAS VIVAS	NO CAMBIE LA ESCALA	REVISIÓN	
			Carlos Zorraquino, LEMA		
	NOMBRE	FIRMA	FECHA	TÍTULO:	
DIBUJ.				embase_1_a	
VERIF.					
APROB.					
FABR.					
CALID.			MATERIAL:	N.º DE DIBUJO	A4
			PESO:	ESCALA:2:1	HOJA 1 DE 1

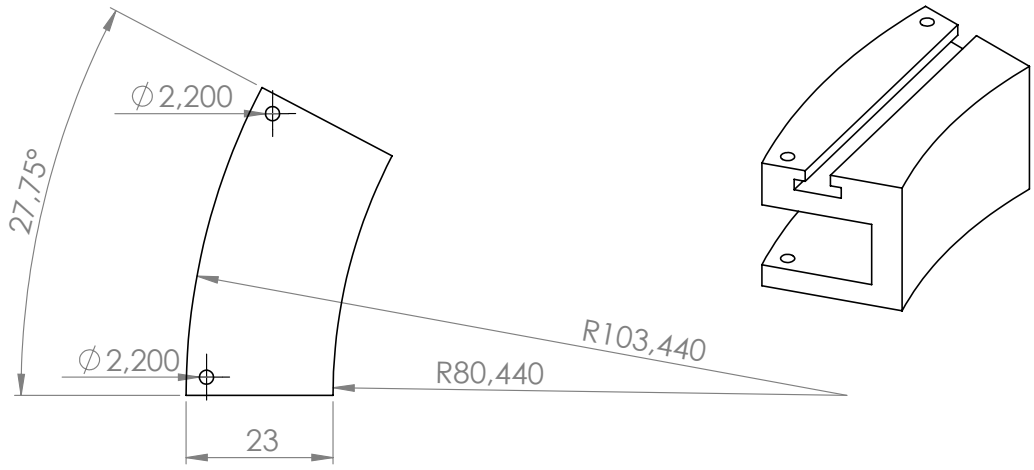

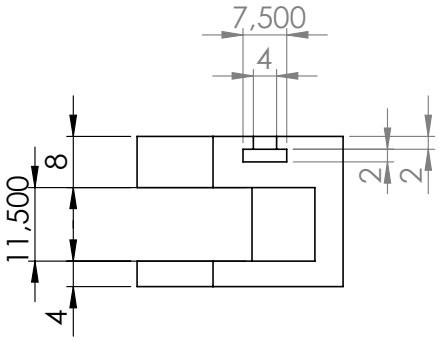

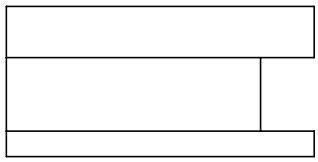

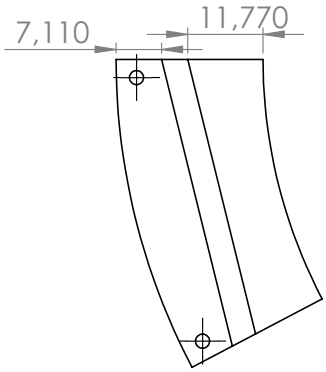

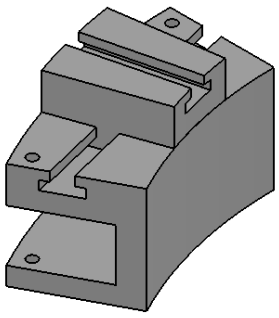

SI NO SE INDICA LO CONTRARIO: LAS COTAS SE EXPRESAN EN MM ACABADO SUPERFICIAL: TOLERANCIAS: LINEAL: ANGULAR:		ACABADO:		REBARBAR Y ROMPER ARISTAS VIVAS		NO CAMBIE LA ESCALA	REVISIÓN
	NOMBRE	FIRMA	FECHA			TÍTULO: Carlos Zorraquino, LEMA	
DIBUJ.							
VERIF.							
APROB.							
FABR.							
CALID.				MATERIAL:		N.º DE DIBUJO embase_1_b	A4
				PESO:		ESCALA:1:1	HOJA 1 DE 1

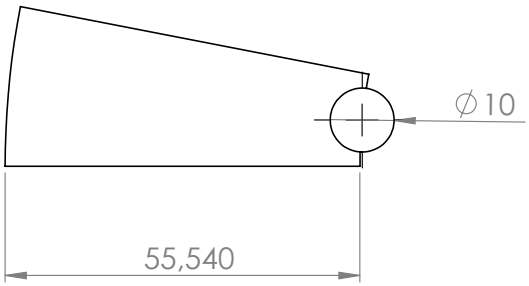

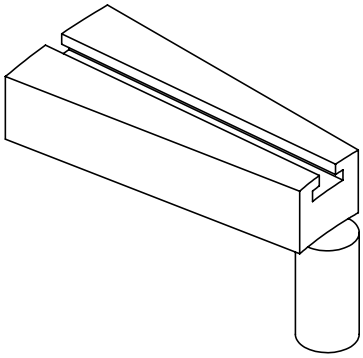

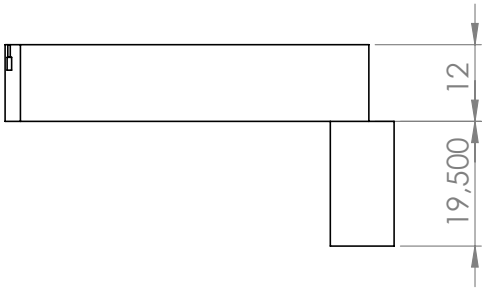

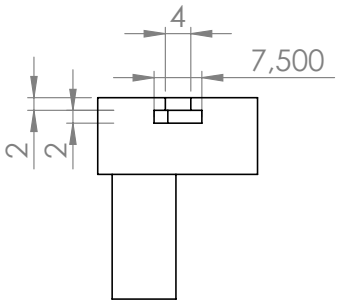

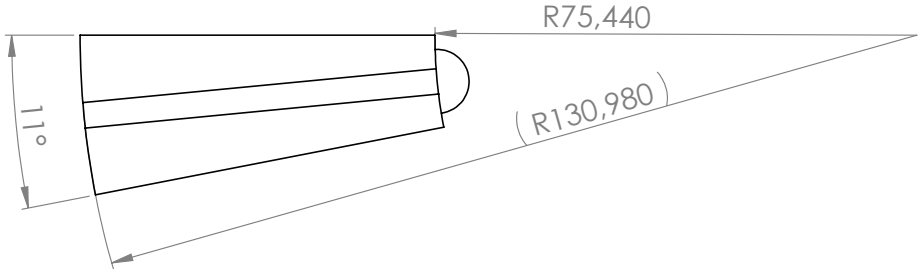

SI NO SE INDICA LO CONTRARIO: LAS COTAS SE EXPRESAN EN MM ACABADO SUPERFICIAL: TOLERANCIAS: LINEAL: ANGULAR:		ACABADO:			REBARBAR Y ROMPER ARISTAS VIVAS	NO CAMBIE LA ESCALA	REVISIÓN
	NOMBRE	FIRMA	FECHA			TÍTULO: Carlos Zorraquino, LEMA	
DIBUJ.							
VERIF.							
APROB.							
FABR.							
CALID.				MATERIAL:		N.º DE DIBUJO embase_2_a	A4
				PESO:		ESCALA:1:1	HOJA 1 DE 1

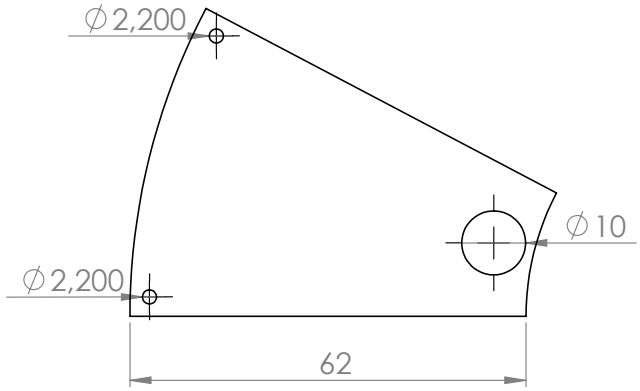

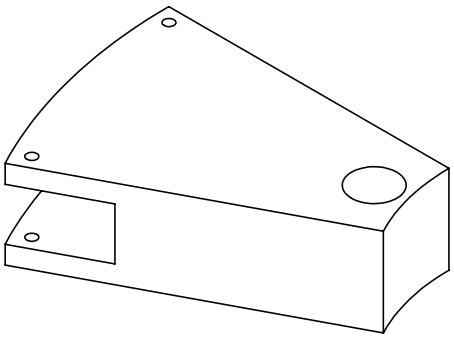

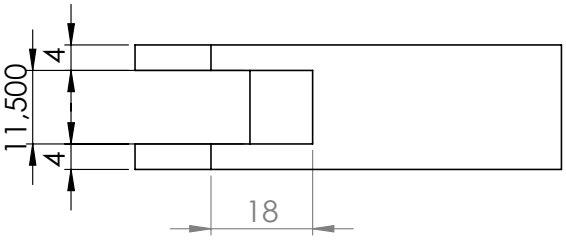

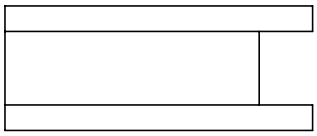

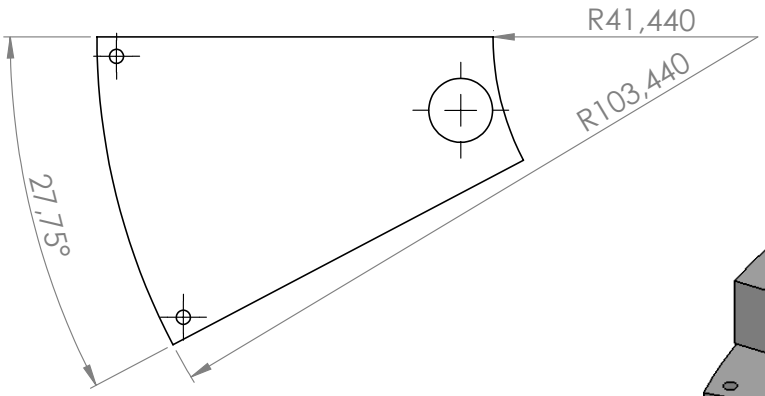

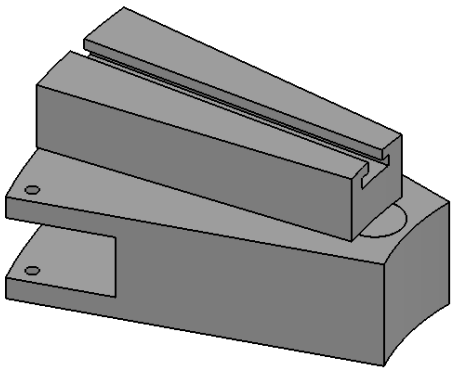

SI NO SE INDICA LO CONTRARIO: LAS COTAS SE EXPRESAN EN MM ACABADO SUPERFICIAL: TOLERANCIAS: LINEAL: ANGULAR:	ACABADO:	REBARBAR Y ROMPER ARISTAS VIVAS	NO CAMBIE LA ESCALA / REVISIÓN

	NOMBRE	FIRMA	FECHA
DIBUJ.			
VERIF.			
APROB.			
FABR.			
CALID.			

TÍTULO: Carlos Zorraquino, LEMA

MATERIAL:

N.º DE DIBUJO: embase_2_b

A4

PESO:

ESCALA:1:1

HOJA 1 DE 1

1.3. Annex 3: MLP mechanical draws

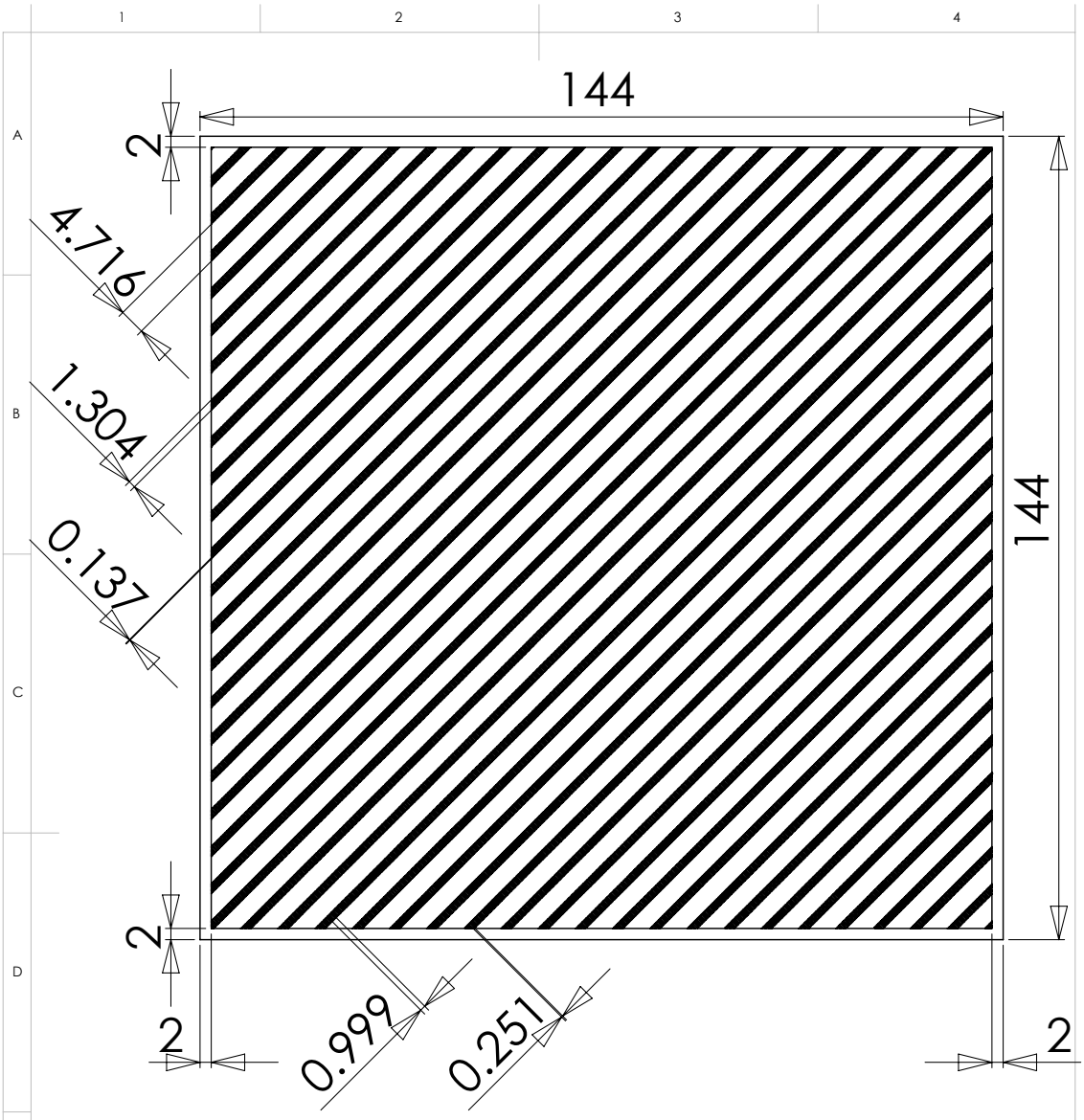

Note: - Mask in positive
- Gerber: 3 - 5 leading zeros
- Dimensions in millimeters

UNLESS OTHERWISE SPECIFIED: DIMENSIONS ARE IN MILLIMETERS SURFACE FINISH: TOLERANCES: LINEAR: ANGULAR:		FINISH:			DEBUR AND BREAK SHARP EDGES	DO NOT SCALE DRAWING	REVISION
	NAME	SIGNATURE	DATE				
DRAWN						TITLE:	
CHK'D							
APPV'D							
MFG							
Q.A				MATERIAL:		DWG NO. JF_outerLayer	A4
				WEIGHT:		SCALE:1:1	SHEET 1 OF 1

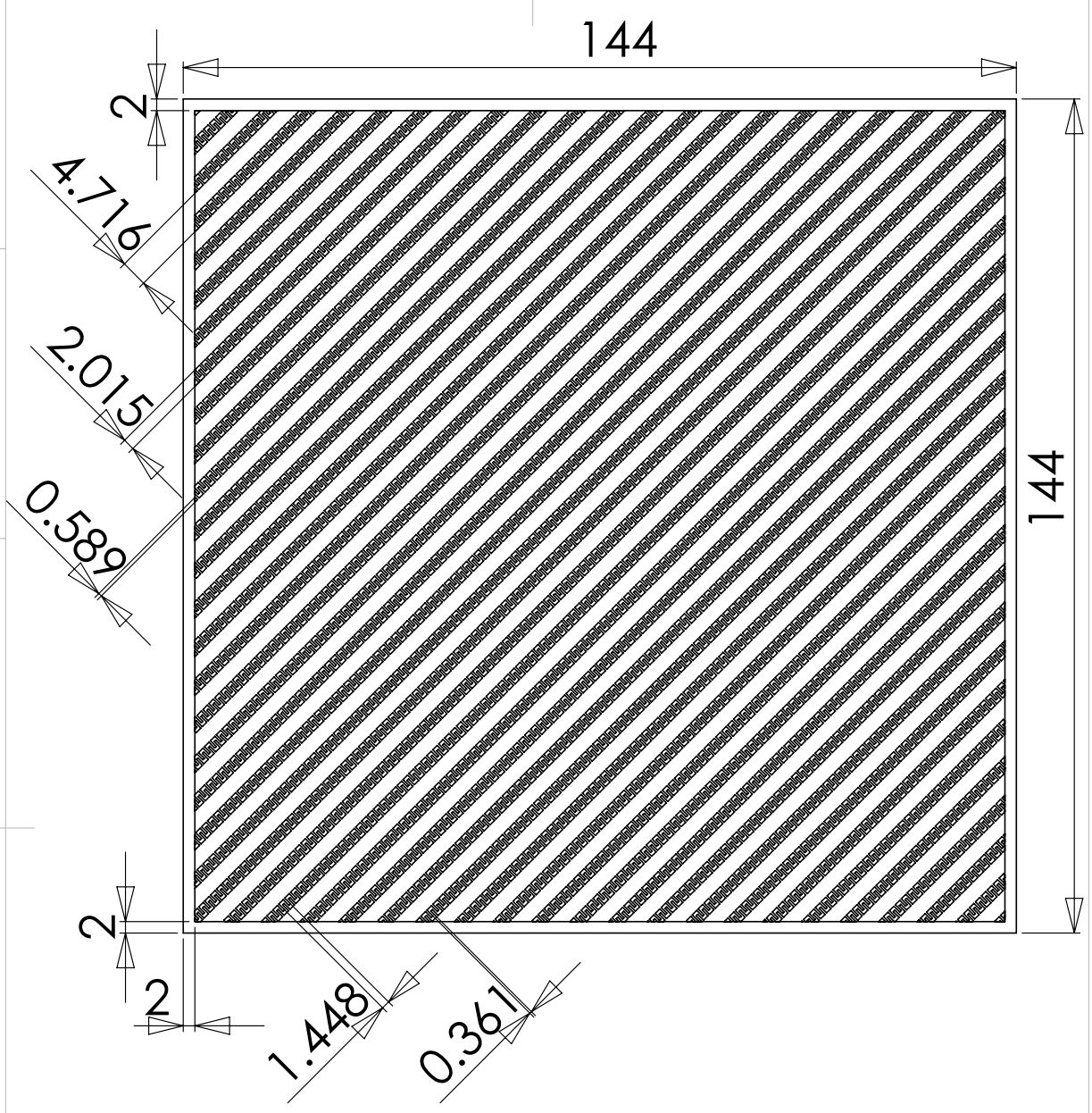

Note: - Mask in positive
- Gerber: 3 - 5 leading zeros
- Dimensions in millimeters

UNLESS OTHERWISE SPECIFIED: DIMENSIONS ARE IN MILLIMETERS SURFACE FINISH: TOLERANCES: LINEAR: ANGULAR:	FINISH:		DEBUR AND BREAK SHARP EDGES	DO NOT SCALE DRAWING	REVISION	
	NAME	SIGNATURE	DATE			TITLE:
DRAWN						
CHK'D						
APPV'D						
MFG						
Q.A				MATERIAL:	DWG NO. JF_innerLayer	A4
				WEIGHT:	SCALE:1:1	SHEET 1 OF 1

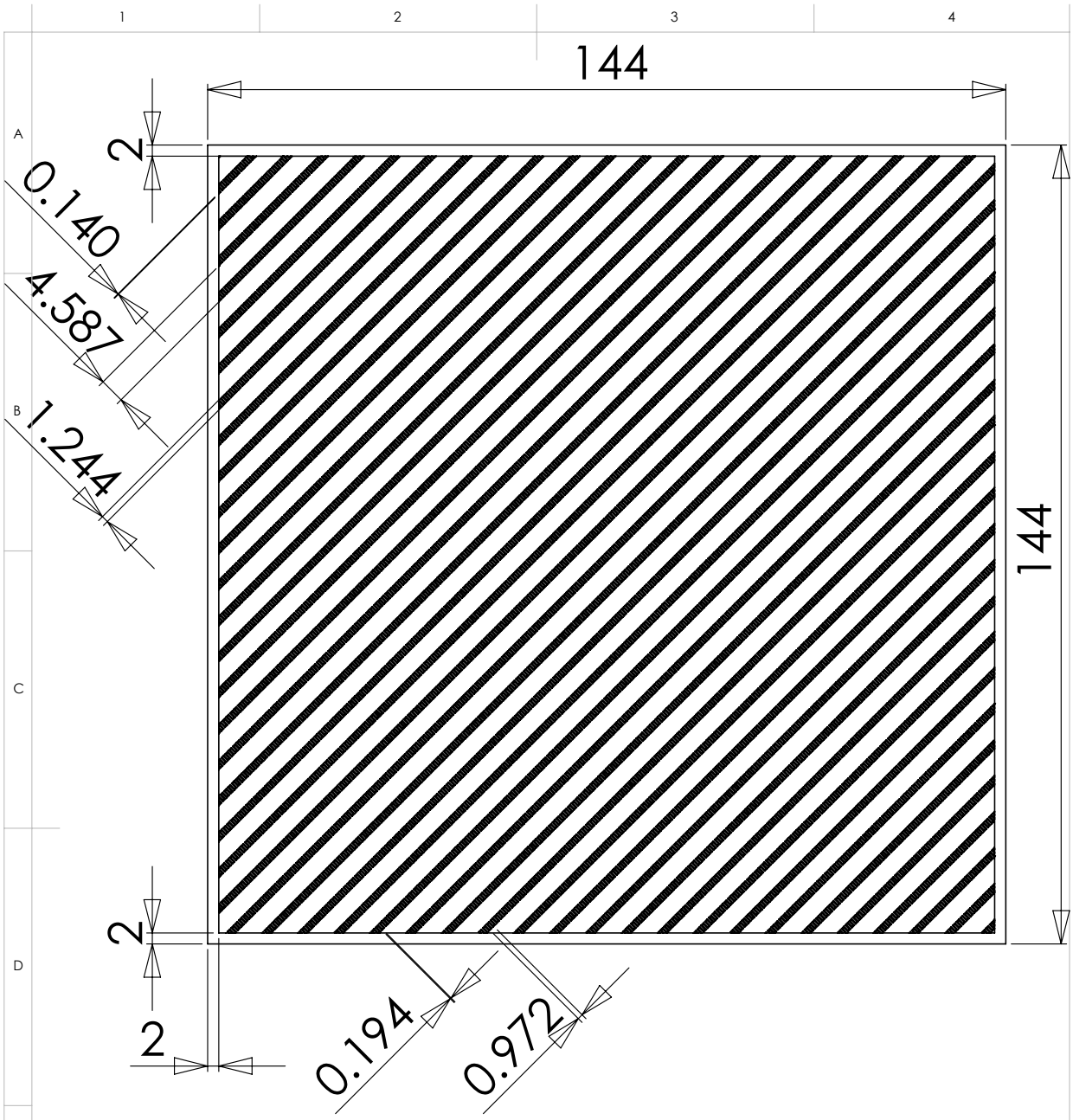

Note: - Mask in positive
- Gerber: 3 - 5 leading zeros
- Dimensions in millimeters

UNLESS OTHERWISE SPECIFIED: DIMENSIONS ARE IN MILLIMETERS SURFACE FINISH: TOLERANCES: LINEAR: ANGULAR:	FINISH:			DEBUR AND BREAK SHARP EDGES	DO NOT SCALE DRAWING	REVISION
	NAME	SIGNATURE	DATE		TITLE: Carlos Zorraquino, LEMA	
DRAWN						
CHK'D						
APPV'D						
MFG						
Q.A				MATERIAL:	DWG NO. outerLayer	A4
				WEIGHT:	SCALE:1:1	SHEET 1 OF 1

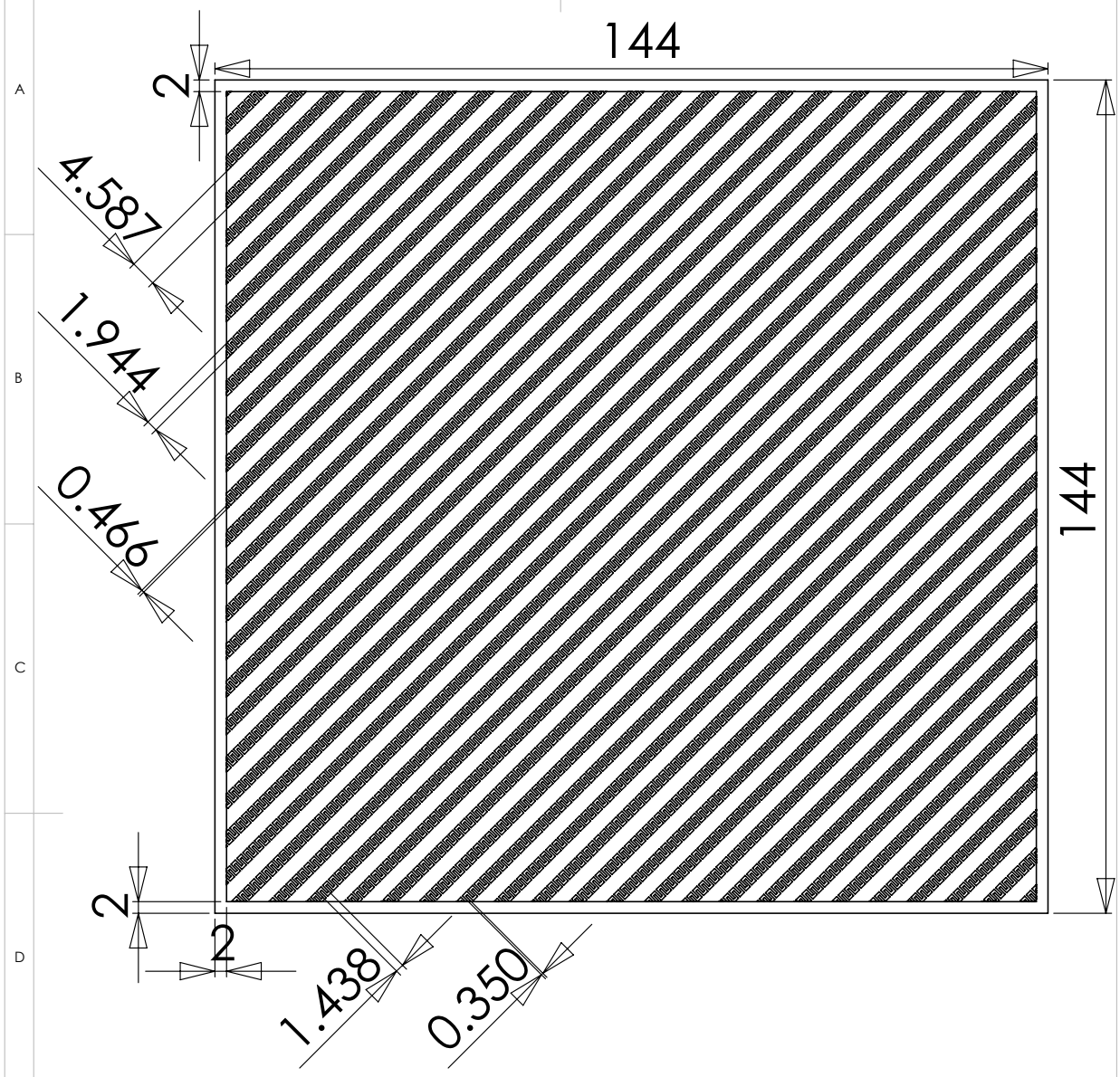

Note: - Mask in positive
- Gerber: 3 - 5 leading zeros
- Dimensions in millimeters

UNLESS OTHERWISE SPECIFIED: DIMENSIONS ARE IN MILLIMETERS SURFACE FINISH: TOLERANCES: LINEAR: ANGULAR:	FINISH:			DEBUR AND BREAK SHARP EDGES	DO NOT SCALE DRAWING	REVISION
	NAME	SIGNATURE	DATE		TITLE:	
DRAWN						
CHK'D						
APPV'D						
MFG						
Q.A				MATERIAL:	DWG NO. innerLayer	A4
				WEIGHT:	SCALE:1:1	SHEET 1 OF 1